# GEOMETRICAL THEORY, MODELING AND APPLICATIONS OF CHANNEL POLARIZATION

A Thesis
Presented to
The Academic Faculty

by

**Seek Chul Kwon**

In Partial Fulfillment
of the Requirements for the Degree
Doctor of Philosophy in the
School of Electrical and Computer Engineering

Georgia Institute of Technology
December 2013

# GEOMETRICAL THEORY, MODELING AND APPLICATIONS OF CHANNEL POLARIZATION

Approved by:

Dr. Gordon L. Stüber, Advisor
Committee Chair
Joseph M. Pettit Chair Professor
School of Electrical and Computer Engineering
*Georgia Institute of Technology*

Dr. John R. Barry
Professor
School of Electrical and Computer Engineering
*Georgia Institute of Technology*

Dr. Geoffrey Ye Li
Professor
School of Electrical and Computer Engineering
*Georgia Institute of Technology*

Dr. Faramarz Fekri
Professor
School of Electrical and Computer Engineering
*Georgia Institute of Technology*

Dr. Sung Ha Kang
Professor
School of Mathematics
*Georgia Institute of Technology*

Date Approved: 5 November 2013

*To*

*my parents, Bong Joong Kwon & Young Soon Choi;*

*my parents-in-law, Myung Keun Lee & Joon Beom Lee;*

*my late grand mother, Dong Choon Lee;*

*and my wife, Jung Yeon Lee*

# ACKNOWLEDGEMENTS

I have enjoyed my journey of doctoral research. The journey was not a means of achieving my goal, but every moment of the journey was the ultimate goal itself. Some have accompanied me from the beginning to the end of this journey, while I have met others at some points of the journey. I cannot agree more that each of them is a precious person who had me become far more mature at this moment than before the journey. I cannot complete this journey without acknowledging their favors.

It has been an honor to have Prof. Gordon L. Stüber as my thesis advisor. He has presented me a wonderful research topic with which I could set out on this journey to a wonderland feeling my heart fluttering. He has waited for me to achieve meaningful research results with much patience, insightful comments, and priceless advice. He deserves my earnest acknowledgment. I am sincerely grateful for the time and efforts that my dissertation committee members, Prof. John R. Barry, Prof. Geoffrey Ye Li, Prof. Faramarz Fekri, and Prof. Sung Ha Kang, spent on my thesis dissertation. They have done me many favors whenever I asked them, which I will never forget. I am also earnestly grateful for the help and advice from professor Choongyong Lee and professor Ilgu Yun at Yonsei University; and professor Giuseppe Caire and professor Robert Scholtz at University of Southern California.

I would like to acknowledge my group members: Sami Almalfouh, Hyungseok Yu, Sajid Saleem, Inho Lee, Yi-Syun Yang, Wenbin Chang, Wei Li, Jiawei Wang, Alireza Borhani for their friendship and help to me. Further, I acknowledge Georgia Tech. staffs, Patritia Dixon, Cordai Farrar, and Daniela Staiculescu, for their unforgettable help. I also appreciate the friendship and favors of all my friends in Georgia Tech., Emory University, Atlanta and the world, including Cem Ozturk, Ayse Ozturk,

Marco Contarini, Deborah Contarini, Fabiana Visentin, Yanwen Wang, Chongchao Zhao, Yusun Chang, Christy Mihyeon Jeon, Wonyeol Lee, Sungoh Choi, Minsik Ahn, Sangtaek Han, Hyungsoo Kim, Eun Seok Ryu, Soohyun Bae, Nari Kim, Sangwook Suh, Jinwoo Kang, Aravind Kailas, Jinwoo Jung, Yong Joon Chang, Hyoungsuk Jun, Haejoon Jung, Jonathan Chongkang Kim, Byungki Byun, Sunghwan Shin, IlSeo Kim, Hyunwoo Cho, Daewon Lee, Soohwan Kim, Jae Young Choi, Joon Hoi Hur, Kwanwoo Kim, Jaehyuk Choi, Dongwon Kwon, Hayang Kim, Sungho Beck, Hangue Park, Hyunwoo Park, Hwajung Hong, Steeve Taejin Kim, Minki Cho, Michael Lee, William Song, Taehoon Shin, Kyujung Han, Woojin Choi, Yongjin Cho, Younghoon Jung, Sang Eon Bak, Sanghyun Chang, Jeongyeup Paek, Taesup Moon, Seunghoon Nam, Chulhan Lee, Hosung Jeff Kang, Sangmin Oh, Youngjae Kim, Jaewook Lee, Youkeun Oh, Myungjoon Kim, Kyunhyung Kim, Ilho Kim, and Taekhyun Kwon. I cannot agree more that I have been a happy person, recalling the memory of friendship between me and them.

I dedicate my Ph.D. thesis to my late grand mother, Dong Choon Lee, who had frequently said that she really hoped to see it. She was the person to present me the first desk of my own, which was small but wonderful. I appreciate the endless support of my parents, Bong Joong Kwon and Young Soon Choi; and parents-in-law, Myung Keun Lee and Joon Beom Lee. Without their love and support, I cannot help giving up my dream. I also thank my sisters, brother, brothers-in-law, sister-in-law: Tae Yeon Kwon/Soo Young Choi, Tae Im Kwon, Seok Hoon Kwon/Dasom Lee, Jin Seok Lee, and Jin Wook Lee.

Last but not least, I would like to express much gratitude and love to another myself, Jung Yeon Lee. She has been always my best strategist, and without her love and advice, I would not have been able to complete this work. She is my home.

# TABLE OF CONTENTS

# LIST OF TABLES

# LIST OF FIGURES

# SUMMARY

Polarization diversity resulting from the wireless channel depolarization has attracted considerable attention since it has large potential of improving the performance of present wireless communication systems. However, the characteristics of wireless channel polarization/depolarization are not fully known, in particular, for none line-of-sight (NLoS) polarized wireless channels, which is a normal scenario of wireless communication systems such as cellular land mobile systems, vehicular communication systems, and wireless body area network (BAN). For this reason, wireless channel polarization has not been utilized enough to satisfy the expected performance improvement beyond the present wireless communication systems; further, the performance of polarized wireless channel seriously depends on the channel conditions considered in conventional wireless communication systems.

This research contributes largely to the comprehensive understanding and modeling of polarized wireless channels; and novel utilization of unique characteristics revealed from them. The thesis consists of three basic streams: 1) a geometrical theory and models for fixed-to-mobile (F2M) and mobile-to-mobile (M2M) polarized wireless channels; 2) wireless BAN polarized channel modeling; and 3) a polarization division multiple access (PDMA) scheme exploiting polarization diversity and multiplexing. Polarization in the wireless channel takes center stage in the thesis.

In this research, we propose a geometrical theory that reveals the origin and mechanism of channel depolarization by focusing on the tilt of "conservation of polarization (CoP)" planes. Using the theory, we develop geometry-based stochastic models for

F2M and M2M polarized wireless fading channels. Those models show good agreement with previously reported empirical data in terms of cross-polarization discrimination (XPD), which is the principal measure of channel depolarization. Further, the models explain the reasons of unique symptoms in polarized wireless channels. We also propose a new polarized channel model for the wide-band wireless BAN, which can separately consider three propagation modes. Scattered waves from the surrounding surfaces and the body can be modeled by the cylindrical-surface-scattered (CSS) and body-scattered (BS) propagation modes, respectively, and those from the ground are to be modeled by a ground-scattered (GS) propagation mode.

Finally, we design and propose a cellular down-link PDMA scheme with polarization-filtering (PF) detection and cooperative transmitter-receiver-polarization (Tx-Rx-polarization) adjustment for wide-band NLoS wireless polarized fading channels. The fundamental novelty of the proposed scheme is that it can adjust transmit polarization angles to change the channel impulse response itself and yield a more desirable complex cross-polarization discrimination (XPD) observed at receivers. This is a significant difference between the proposed scheme and the conventional multiple-input multiple-output (MIMO) systems. The capacity analysis of the proposed PDMA scheme is provided, and the feasibility and satisfactory performance of the proposed scheme are demonstrated even when serious time-variant channel depolarization occurs. The proposed cellular down-link PDMA scheme uses practical synchronous orthogonal frequency division multiple access (OFDMA) with an appropriate channel parameter estimator. The PDMA scheme has large potential to be utilized as a new multiple access/mlutiplexing technique along with the conventional time, frequency, and code division multiple access (TDMA, FDMA, and CDMA); and spatial multiplexing for next-generation wireless communication systems.

# CHAPTER I

# INTRODUCTION

## *1.1 Motivation*

Long-term evolution (LTE) standard has been successfully stabilized, and launched in several areas of the United States, Scandinavia, Japan, and South Korea. However, the required data rate is expected to increase significantly as the explosively increasing number of smart-phone users implies. For that reason, this is already the time for researchers to concentrate on a new multiple-access scheme in wireless communications to satisfy the channel capacity that those smart users will want in the not-too-distant future. The diversity and multiplexing in a new domain - the polarization domain - rather than the conventional space, time and frequency domains can be a strong candidate for the solution to that problem in future wireless communication systems via efficiently suppressing cochannel interference and improving channel capacity.

Nevertheless, whether the previously reported research considers polarization multiplexing or diversity gain, the basic approach has usually been to substitute dual-polarized antennas for the spatially separated uni-polarized antennas. That is, some conventional MIMO techniques utilizing spatial diversity are applied to the dual-polarized MIMO system using polarization diversity along with spatial diversity, where the dual-polarized antennas are, usually, spatially separated.

Several remarkable MIMO techniques such as space-time block coding (STBC) and Tx/Rx beamforming have been proposed, based on the MIMO channel characteristics investigated from the well-developed MIMO channel models. On the other hand, the basic approach in polarization multiplexing is usually to substitute dual-polarized antennas for spatially separated single-polarized antennas. In some sense, it is also a sort of MIMO system. However, the problem is that most existing polarization-utilizing techniques do not fully exploit the unique characteristics of polarized channels, but they are based on or aided by conventional MIMO techniques.

In turn, these conventional MIMO techniques are best optimized not to the polarized channel having polarization diversity, but to the conventional MIMO channel having spatial diversity. For this reason, the relative performance of spatial versus polarization diversity is substantially dependent on the channel condition. Sometimes the use of both polarization and spatial diversity will yield a performance that is worse than if polarization diversity is not used at all.

Considering all these situations, it is necessary to develop the comprehensive polarized wireless channel model where a concrete XPD reference model is embedded such that we can exploit the unique characteristics of polarized wireless channel revealed from the channel model. Furthermore, the reason why channel depolarization happens and the mechanism how it affects wireless channel must be clearly explained based on the XPD reference model if we want to figure out the channel condition in which the polarization-utilizing technology shows good performance. It is obvious that polarization-utilizing technology can show the best performance only when it is besed on a deep understanding of the unique characteristics of the polarized wireless channels as will be shown in this thesis.

## *1.2 Research Contributions*

To the best of my knowledge, the proposed theory and models in this thesis are the first which reveals the origin and mechanism of wireless channel depolarization in a geometry-based methodology, and provides a method of deriving XPD in a quantitative manner for a given geometrical environment. Furthermore, the proposed PDMA scheme is the first which shows feasibility of utilizing polarization domain for a multiple access/multiplexing scheme without the aid of spatial diversity or other conventional MIMO techniques in the OFDMA-based wireless cellular systems. This section summarizes the contributions of this thesis.

- A geometrical theory, which can reveal the origin of wireless channel depolarization is established. The theory can also describe the general mechanism of channel depolarization, which can be applied to any other wireless communication systems even having NLoS reflected/scattered wave propagation components. We show that the tilt of "*conservation-of-polarization (CoP)*" plane in three-dimensional (3-D) space creates wireless channel depolarization, and verify it by comparing XPD curves obtained in a manner of quantitative computation and from previously reported measurements.

- A theoretical stochastic model of the narrow-band polarized wireless fading channel in the F2M scenario, is developed based on the aforementioned geometrical theory. The F2M polarized channel model is verified, and shows good agreement with empirical data reported by other authors.

- A M2M polarized channel model is proposed by extending F2M polarized channel model. This model successfully describes the change of wireless channel polarization in the double-bounce radio propagation, which means the waves reflected once at the transmitter (Tx) side and then reflected again at the receiver (Rx) side in vehicular communications. The model also provides the quantitative way of obtaining XPD, and shows different XPD curves from those of the F2M channel scenario.

- A unique 3-D geometry-based statistical model for the polarized wireless BAN channel with three different propagation modes, cylindrical-surface-scattered (CSS), body-scattered (BS) and ground-scattered (GS) propagation modes, is developed. Further, a theoretical modeling of the creeping wave using diffraction theories is performed, and the empirical validation of the proposed model is also provided with a good agreement between the theoretical and empirical results of channel characteristics. Several meaningful analytical characteristics of polarized BAN channels are also presented based on the proposed BAN channel model.

- A novel cellular down-link *Polarization Division Multiple Access (PDMA)* scheme with *polarization-filtering detection* and *collaborative Tx-Rx-polarization adjustment* is proposed for wide-band NLoS wireless polarized fading channels. The fundamental novelty of the proposed scheme is that it can adjust transmit polarization angles to change the channel impulse response itself and yield a more desirable complex XPD observed at receivers. This is a significant difference between the proposed scheme and the conventional MIMO systems. The capacity analysis of the proposed PDMA scheme is provided, and the feasibility and satisfactory performance of the proposed scheme are demonstrated even when serious time-variant channel depolarization and polarization mismatch between receivers occur. The proposed cellular down-link PDMA scheme uses synchronous OFDMA with an appropriate channel parameter estimator. The scheme can be used to extend the capacity of any cellular system that uses uni-polarized antennas, and can be extended and applied to MIMO arrays as well.

## *1.3 Thesis Outline*

The remainder of this thesis is organized as follows. Chapter 2 provides a background review including wireless channel polarization/depolarization, XPD - the main measure of channel depolarization, previously reported empirical results of channel polarization, and the history of the uni-polarized wireless channel modeling, particularly focusing on the MIMO channel. The research in wireless BAN are also reviewed with the important issues in that research area, and then, the concepts of polarization multiplexing and diversity are described along with the problems and issues to be considered for more reliable and improved system performance. Chapter 3 proposes a geometrical theory for depolarization in narrow-band F2M and M2M wireless channels. This novel theory is used to reveal the origin of channel depolarization and to provide a mechanism for computing XPD in a quantitative fashion. A new 3-D geometry-based reference model is proposed for XPD in narrow-band F2M and M2M wireless channels based on the geometrical theory of channel depolarization. Then, the geometrical theory of channel depolarization is applied to the new geometrical BAN channel model in Chapter 4. Further, a cellular down-link PDMA scheme with polarization-filtering detection and collaborative Tx-Rx-polarization estimation/adjustment is proposed for wide-band non-line-of-sight (NLoS) wireless polarized fading channels in Chapter 5. Finally, Chapter 6 concludes the thesis with the description of the research contributions and future research.

# CHAPTER II

# BACKGROUND

## *2.1 Polarization/Depolarization in the Wireless Channel*

Multipolarized antennas have attracted considerable attention as a means of increasing channel capacity and reducing the required antenna spacing through the principle of polarization diversity [1–11]. Such antennas exploit depolarization and have the potential to double or triple the channel capacity that is achievable with single-polarized antennas [5,6,8,12–14]. In practice, cellular land mobile radio systems have employed slant polarized-array antennas at base stations for good benefit.

Depolarization can occur as a result of two factors. One factor arises from the transmitter (Tx) and receiver (Rx) antennas themselves. Any practical antenna-gain pattern can be described in terms of two orthogonal antenna-polarization functions. For a vertically polarized antenna these polarization functions are $f^a_{VV}$ and $f^a_{HV}$, while for a horizontally polarized antenna they are $f^a_{HH}$ and $f^a_{VH}$, where $H$ and $V$ refer to horizontal and vertical polarization, respectively. Assuming ideal antennas having linear polarization, a vertically or horizontally polarized antenna only has non-zero $f^a_{VV}$ or $f^a_{HH}$, respectively. However, for practical antennas, the cross-polarization functions, $f^a_{HV}$ and $f^a_{VH}$, will be non-zero as well because of antenna depolarization.

The other factor causing depolarization, which is the principal subject of this thesis, is the radio propagation environment as depicted in Figure 1. In the environment of rich scattering, each scatterer located in a different position from each other creates different depolarization of the propagated wave. Similar to antenna depolarization, the radio channel can be characterized in terms of four orthogonal channel-polarization functions identified as $f_{VV}$, $f_{VH}$, $f_{HV}$ and $f_{HH}$ in this thesis, where, once again, $H$ and $V$ refer to horizontal and vertical polarization, respectively. The antenna and radio propagation factors can be decoupled, and ideal linearly polarized antennas are assumed to isolate the effect of depolarization in the radio propagation channel. The main measure for the degree of depolarization is cross-polarization discrimination (XPD). It is defined as

$$\mathrm{XPD} = \frac{\text{copolarized average received signal power}}{\text{cross-polarized average received signal power}} , \tag{1}$$

where "copolarized" and "cross-polarized" mean having the same as and orthogonal to the polarization utilized at the Tx, respectively.

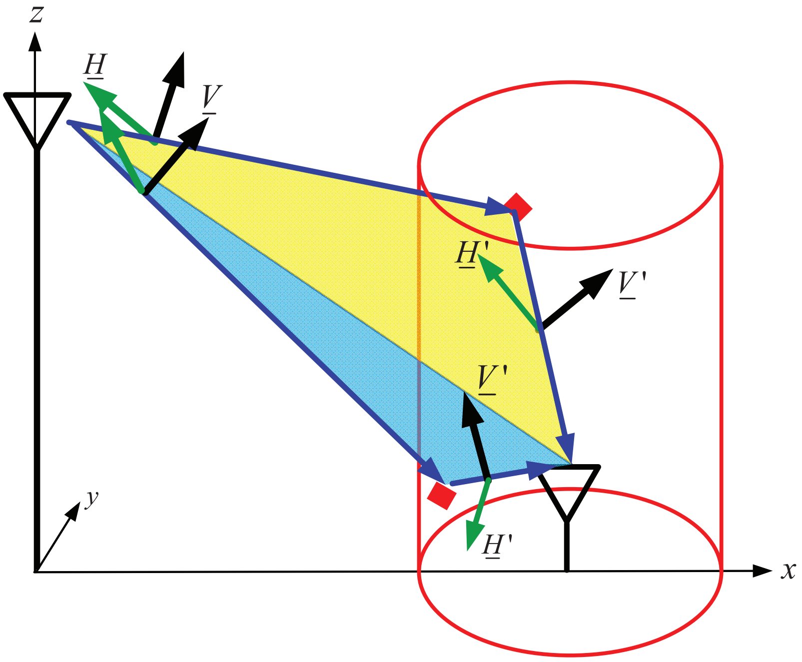

**Figure 1:** Wireless channel depolarization depending on the distinct scatterers.

Several multipolarized-channel models have successfully embedded XPD metrics into them [5, 8, 15–17]. The characteristics of XPD for different antenna orientations have been studied, starting with a truncated Laplacian power azimuth spectrum, which is based on empirical measurements and is widely used to model scattering in indoor channels [17]. The empirical study in [17] takes into account depolarization caused by the antenna configuration. On the other hand, a few papers report on the empirical characteristics of XPD for outdoor channels [1, 7, 12]. The dependence of XPD on the distance between the Tx and Rx is studied in [1, 12], where the measurement campaign shows that XPD tends to approach 0 dB as the Tx–Rx distance increases. However, the variance of XPD at a fixed distance is too substantial to apply curve-fitting approximation to measurement data.

In contrast, the measurement data obtained from several different scenarios in [7] show that XPD does not directly depend on the Tx–Rx distance but varies for the different geometry of the Tx, Rx and scatterers. For example, the comprehensive XPD-sounding campaign is performed at different locations distributed on a certain street, and the relation of XPD to the angle between the street line and the Tx–Rx boresight line is presented. A 3-D polarized multi-input multi-output (MIMO) channel model and mutual information are provided in [8]. This model includes a polarization-channel matrix in the mathematical expression of the model, but the polarization-channel matrix is also based on XPD measurement. The aforementioned empirical-XPD models have considerable differences from each other depending on its measurement environment, and further, those prior works provide no mathematical model for the origin of wireless-channel depolarization.

A number of theoretical/mathematical reference models have been developed for F2M and M2M channels, e.g., [18–27]. A two-dimensional (2-D) single-ring model is utilized to analyze the space-time correlation function (ST-CF) for the F2M-MIMO channel in [18]. A 3-D F2M-channel model is proposed to take into account not only the horizontal component but also the vertical component of the signal's angle-of-arrival (AoA) at the Rx [21]. A statistical model is proposed for the wireless M2M channel between two vehicles in motion without the LoS radio propagation component in [22]. The probability-density function (pdf) of the received signal's envelop/phase, ST-CF and the Doppler spectrum are also presented utilizing the statistical model in [22]. The 2-D single-ring model for the F2M channel is extended to the 2-D double-ring model to study the characteristics of the M2M-MIMO channel such as ST-CF with the assumption that not only the Rx, but also the Tx has a rich scattering environment in the vicinity of it owing to the low antenna elevation [19, 20].

The 2-D double-ring model is extended to the 3-D double-cylinder model for the narrow-band M2M-MIMO channel in [25], and the latter, in turn, is extended to the concentric-cylinder model for the wide-band M2M-MIMO channel in [26]. Those 3-D models are in good agreement with the measurement data in terms of the first- and second-order channel statistics such as the space-time-frequency correlation function (STF-CF), space-Doppler power-spectral density (sD-psd), power space-delay spectral density (psds) and envelope level-crossing rate (LCR), not only for rural areas but also for urban areas. Although the analytical MIMO-channel model such as [24], which has no sense for the physical geometry of the channel, is frequently utilized because of its convenience to use, the 3-D geometry-based model such as [25, 27] exhibits more accuracy and feasibility for realizing wireless channels than the analytical channel model.

In spite of the remarkable contributions of the channel models introduced above, they do not incorporate channel polarization. For that reason, a theoretical model for channel depolarization in F2M and M2M channels need to be developed. The wireless channel is characterized by isotropic or non-isotropic azimuthal scattering and with either NLoS or LoS conditions between the Tx and Rx. In addition, each scenario exhibits different XPD characteristics; therefore, the XPD model must be derived from a geometry-based channel model to reflect a given geometrical scenario on XPD characteristics. To the best of knowledge, the proposed research is the first to develop a geometrical theory for channel depolarization along with a method for determining XPD in a quantitative fashion without the aid of measurement data. Using the proposed geometrical theory of channel depolarization, a new mathematical XPD reference model is proposed for narrow-band F2M and M2M channels, which yields good agreement with the aforementioned empirical results from other authors [1,7,12]. Furthermore, the proposed model can explain the detailed XPD characteristics and their differences observed in [1,7,12].

## 2.2 Wireless BAN Channel

The wireless sensor network and the ad-hoc network have been remarkably active research areas for the last decade. The research results are employed for several applications such as monitoring environments, surveillance for military purposes and data collection/reporting in industries. One promising application among them is wireless BAN, which is the sensor and ad-hoc network around the human body. Wireless BAN has the potential to be widely utilized from the medical monitoring and rehabilitation to wearable computing and sensing in the military.

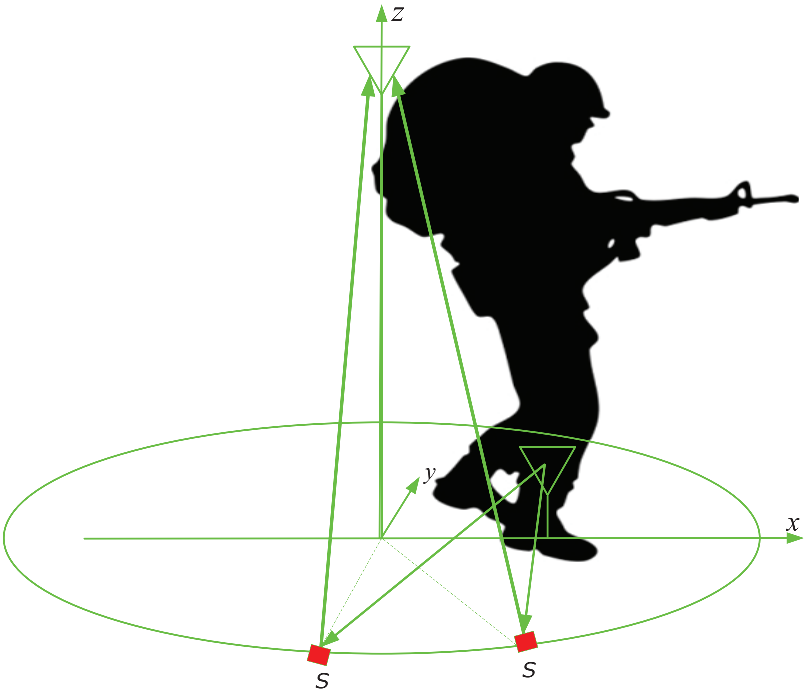

**Figure 2:** Example of a concrete wireless body area network channel model.

Figure 2 describes a dominant channel environment of wireless BAN communications. The importance of concrete BAN wireless channel models have been emphasized recently, since those models can provide crucial hints of utilizing BAN channel characteristics for more complicated BAN communication systems than those in the current stage. The waves scattered from the ground in Figure 2 are regarded as a most important propagation component in wireless BAN channels. However, other propagation components along with creeping wave can also affect wireless BAN channel characteristics as we will see later.

Although wireless BAN has been considered as emerging technology to improve human life in many aspects, the following issues regarding the wireless-BAN channel are still considered as critical limitations [28,29]: 1) interference on a wireless communication channel caused by multiple sensors/devices; 2) the lack of system integration of individual sensors; and 3) the necessity of long-term power consumption. The first issue is created directly by substituting wireless channels for unwieldy wires between sensors, and the other two issues also require an understanding of the channel characteristics in wireless BAN. Furthermore, future BAN will also require a sophisticated wireless-communication system with a multiple-access scheme as already shown in military research.

Multipolarized antennas in BAN channels can exploit polarization degrees of freedom and have the potential to significantly increase the channel capacity that is achievable with single-polarized antennas through polarization diversity and multiplexing [1, 5, 6, 8, 12, 13]. Recalling the advantage of multipolarized antennas, the BAN having multipolarized-antenna elements is promising technology that may solve the aforementioned critical issues. The improvement of achievable channel capacity will decrease the waiting time of the device that has to transmit or receive pertinent data, and the device can be in the sleep mode longer than in the case of a long waiting time; therefore, it contributes to long-term power consumption [28]. Moreover, when an urgent event happens, all sensors that are monitoring related events will begin to try transmitting the collected data to their central device. For this reason, mitigating interference on the wireless-BAN channel that is shared by the devices/sensors is a rising issue [29]. Further, the sophisticated wireless-communication system with multi-antennas for each sensor/device may be integrated on a human body; therefore, how to reduce antenna spacing at each node can be a pressing question for convenience. The multipolarized antenna is one of the strong candidates for the aforementioned issues, and applying it to the BAN requires an understanding of polarized channels in the wireless BAN.

Several empirical studies on BAN channels have often been cited in the literature, including [30–37]. The path-loss and power-delay profile (PDP) associated with the different locations of the transmitter (Tx) and receiver (Rx) are provided in [34, 37]. In [35, 36], the multi-path components are distinguished and clustered according to their average PDP, and the impact of arm motions on the wireless BAN channel are also reported in [35]. A path loss model and other properties of the diffracted creeping wave is studied in [30–33]. Likewise, research on antennas for wireless BANs has been active as well [38–42]. Only a few studies consider polarized wireless BAN channels [43], although several polarized channel models exist for land mobile radio (LMR) and vehicle-to-vehicle (V2V) channels [5, 8, 9, 15–17].

In contrast to the empirical BAN channel models, no theoretical BAN channel model has been previously reported. Moreover, only a few studies have considered multipolarized BAN channel models [43], although several multipolarized channel models exist for F2M and M2M channels [5, 8, 9, 15–17]. In particular, the F2M/M2M channel-depolarization model in [9] reveals the origin and meaningful characteristics of channel depolarization based solely on the scattering geometry. A similar approach can be applied to wireless BAN channels, but the geometrical models used to represent the scattered-wave propagation components for the polarized wireless-BAN channels must be quite different from those for F2M/M2M channels [10].

The polarized BAN channel can be characterized by either isotropic or non-isotropic azimuthal scattering and with either NLoS or LoS conditions between the Tx and Rx that are both located on the body as implied in [5,8–10,15–17]. In particular, from the previously reported empirical research, the BAN channel is considered to have the following four propagation modes: scattered waves from the surrounding surfaces above the ground, from the ground, from the body, and the LoS wave. Scattered waves from the surrounding surfaces and the body can be modeled by the cylindrical-surface-scattered (CSS) and body-scattered (BS) propagation models, respectively, and those from the ground are to be modeled by a ground-scattered (GS) propagation model. Among those four components, the LoS component is often blocked by the human body, particularly when the Rx and Tx are located on opposite sides of the human body. The scattered waves from the ground, which corresponds to the GS propagation described in Figure 2, have been reported as a stable and dominant radio propagation component in wireless BAN channels.

## *2.3 Polarization Diversity and Multiplexing*

The phenomenon of channel depolarization in wireless communication systems has been regarded as the key to utilizing polarization diversity and multiplexing [1,5,7–9]. Depolarization deteriorates the performance of polarization multiplexing schemes, but at the same time it can provide polarization diversity. Multipolarized antennas utilize the polarization diversity caused by the channel depolarization to increase channel capacity and to reduce the required antenna spacing [2,44,45].

Channel depolarization causes polarization correlation between the received signals that are orthogonally polarized at a Tx. However, polarization multiplexing combined with or utilizing the methodologies of conventional MIMO techniques, such as space-time block coding (STBC), water-filling, and beamforming shows satisfactory improvement in the channel capacity overcoming channel depolarization [44–46].

In this thesis, we only consider polarization diversity and multiplexing scheme without the aid of spatial diversity of other conventional MIMO techniques. In Figure 3, the Tx having a dual-polarized antenna transmits two signals with different polarization, and the Rx has the mixed signals at both the vertically and horizontally polarized antennas. The fundamental question is whether we can design a polarization filtering scheme such that the signal blended with two desired signals is decomposed into two original signals again. The answer is "Yes" as we will see later in Chapter 5. On the other hand, if the Tx sends two different signals to different mobile stations (MSs), this case corresponds to the down-link of the multiple access, and we call this scenario down-link PDMA.

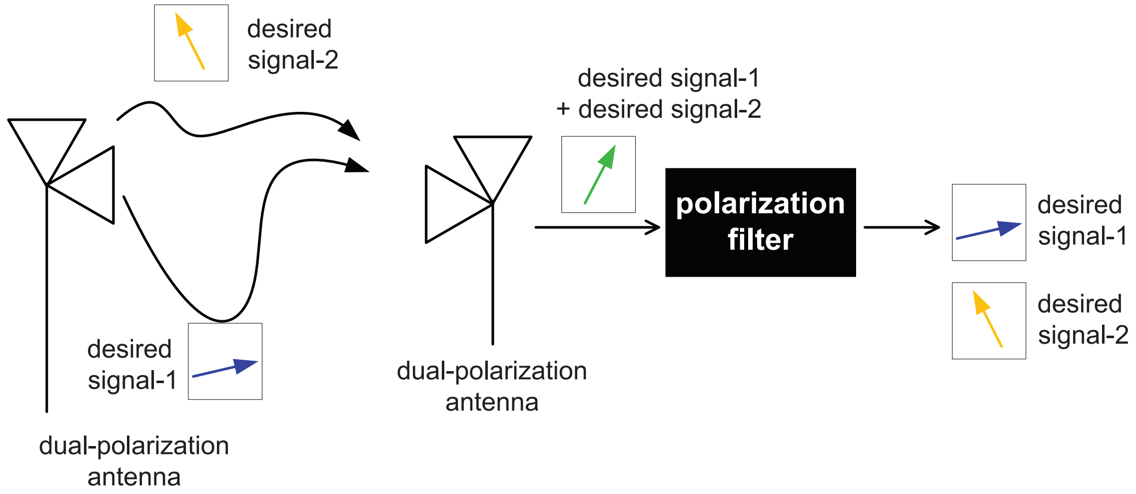

**Figure 3:** Concept of polarization multiplexing.

Whether the previously reported research considers polarization multiplexing or diversity, the basic approach has always been to substitute dual-polarized antennas for spatially separated single-polarized antennas. That is, some conventional MIMO techniques utilizing spatial diversity are applied to the dual-polarized MIMO system using polarization diversity (and spatial diversity) whether the dual-polarized antennas are still spatially separated, colocated or in-between.

While conventional MIMO techniques have been proposed to principally utilize the spatial diversity of MIMO channels, most existing polarization-utilizing techniques do not fully exploit the unique characteristics of polarized channels, but rather are based on or aided by conventional MIMO techniques. In turn, these conventional MIMO techniques are best optimized not to the polarized channel having polarization diversity, but to the conventional MIMO channel having spatial diversity. This is the main reason that the relative performance of spatial versus polarization diversity is very much dependent on the specific channel condition [44,45]. Sometimes the use of both polarization and spatial diversity will yield a performance that is worse than if polarization diversity were not used at all.

The technology that exploits polarization multiplexing or diversity must be based on an understanding of the unique characteristics of the polarized channel such as the theoretical and empirical research results [1,5,7–9,12]. A geometrical theory of wireless-channel depolarization was introduced for channel depolarization in [9], which is in good agreement with the detailed empirical results reported by other authors [1,7]. The aforementioned research is regarded as helpful in developing polarization-related technology and in verifying its feasibility.

The PDMA scheme designed in this thesis purely exploits polarization diversity without the aid of conventional MIMO techniques that utilize spatial diversity or space-time multiplexing such as STBC. The suggested PDMA scheme is applied to wide-band multipolarized multi-path fading channels found in cellular down-links. Furthermore, the NLoS-F2M channel is taken into account to show that the PDMA scheme is feasible even when serious channel depolarization exists. The assumption of a NLoS-F2M channel, particularly, in dense metropolitan areas is more common than a specular-fading channel. Moreover, in the latter, the proposed PDMA scheme shall show better performance than in the former because of the strong LoS copolarized-wave component.

The cellular down-link PDMA scheme needs to be applied to an orthogonal frequency division multiple access (OFDMA) system according to the LTE standard; therefore, the detection scheme exploiting polarization will have to be applied on a per-subcarrier basis. The current cellular system utilizes the feedback channel between the Tx and Rx. Hence, a scheme of feedback Tx-polarization adjustment is feasible for controlling the XPD of each signal at the Rx.

For channel and polarization-state estimation in the PDMA system, a previously proposed scheme of channel-state estimation can be utilized. For example, equally-spaced pilot symbols are suggested to minimize the error probability in [47], and it can be modified to provide polarization-state information (PSI) in the PDMA system, as will be described in Chapter 5. In this chapter, channel-state parameters are estimated on a per-block basis, which is particularly appropriate for packet data transmission, where the Rx may receive distinct blocks with unknown delays as in [47] and [48]. However, it is worth mentioning that the pilot-symbol-aided inter-block channel/polarization state estimation may be possible as well [49].

# CHAPTER III

# GEOMETRICAL THEORY OF CHANNEL DEPOLARIZATION IN F2M/M2M WIRELESS CHANNELS

A geometrical theory is proposed for depolarization in narrow-band F2M and M2M wireless channels. This novel theory is used to reveal the origin of channel depolarization and to provide a mechanism for computing cross-polarization discrimination (XPD). The main contributions in this section are as follows: 1) A geometrical theory to explain the origin of channel depolarization; 2) A methodology to quantitatively compute XPD: the superposition of the co and cross-polarization components on conservation-of-polarization planes; and 3) A 3-D geometry-based theoretical XPD model for narrow-band F2M and M2M channels. This section is organized as follows. Section 3.1 presents the novel geometrical theory for channel depolarization along with a methodology to quantitatively compute XPD from a 3-D geometry-based reference model for F2M channels. This approach is extended to M2M channels in Section 3.2. In Section 3.3, predictions from our model are compared with previously reported measurement data [1, 7, 12] and shown to have close agreement.

## *3.1 Channel Depolarization and XPD Reference Model for F2M Channels*

This section describes the 3-D geometry-based model for channel depolarization in narrow-band NLoS or LoS-F2M channels, and describes the methodology used to obtain the XPD. Meanwhile, the underlying theory is expanded to explain the impact of the channel-modeling parameters on the XPD.

### 3.1.1 3-D Single-cylindrical XPD Reference Model

As shown in Figure 4, the model assumes that scatterers are distributed on a cylindrical surface in the vicinity of the mobile station.[1] These scatterers result in single-bounced receiver-side (SBR) propagation from a base station Tx to a mobile-station Rx. The high-elevation base station antenna is assumed to be free of local scattering, which is typical of cellular land mobile radio systems. A LoS component may or may not exist between the Tx and the Rx.

The 3-D cylindrical model in Figure 4 has been suggested before for cellular land mobile radio channels [21, 50], but has not been used previously to study XPD. The cylindrical scattering-surface is characterized by its radius, $R_r$, and the ray incident on the Rx antenna from each scatterer on the cylinder has an associated azimuth angle-of-arrival (AAoA), $\alpha_R$, and elevation angle-of-arrival (EAoA), $\beta_R$. The purpose of this section is to derive XPD of each individual received plane wave as a function of $\alpha_R$, $\beta_R$, $R_r$, and the distance between the Tx and the Rx, $D$. Afterwards, we will obtain the mean XPD that accounts for the plane waves received via all the scatterers.

### 3.1.2 Origin of Channel Depolarization

The phenomenon of channel depolarization between a Tx and an Rx can be explained by the NLoS plane waves that arrive at the Rx via scattering objects. A vertically (horizontally) polarized plane wave emitted from the base station Tx can result in a horizontally (vertically) polarized plane-wave component being received at the mobile-station Rx as shown in a scenario of Figure 4. The vector $\underline{V}$ in Figure 4 is the vertical polarization vectors of a plane wave from the Tx, and $\underline{V}$' is the corresponding polarization vector of the plane wave after reflection from a receiver-side scatterer. By convention the vertical- and horizontal polarization vectors are parallel to $\underline{\mathrm{e}}_\theta$ and

---

[1] Here the term "scatterer" refers to a plane boundary that is typically much larger than a wavelength.

$\underline{e}_{\phi}$, respectively, when describing the plane wave's direction of propagation at the Tx or Rx in a spherical coordinate system [7]. It is clear that $\underline{V}$' is not entirely vertically and horizontally polarized at the Rx, but has a cross-polarization component as well. This phenomenon is called channel depolarization and will be shown to be affected mainly by $\alpha_R$ and $\beta_R$ in our model as opposed to $R_r$ and $D$.

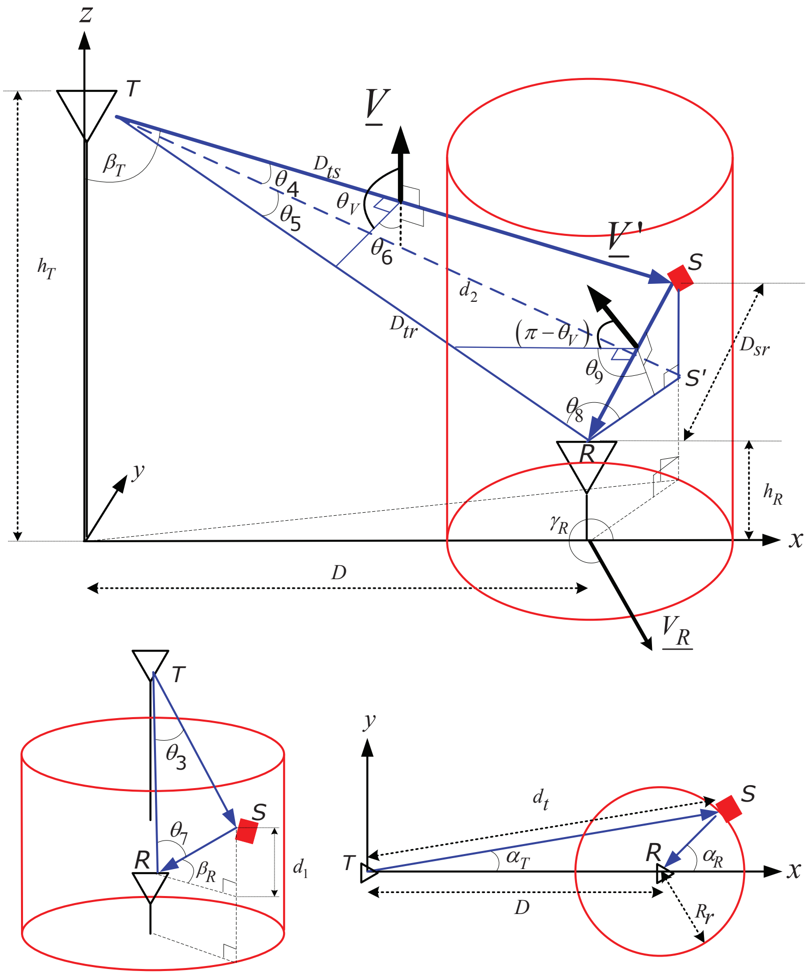

**Figure 4:** 3-D cylindrical scattering model for XPD on narrow-band F2M channels.

Channel depolarization is affected by the scattering geometry as shown in Figure 4. For the plane wave that is emitted from the Tx and received at the Rx via a scatterer, the plane that is defined by the Tx, Rx and the scatterer must be taken into account. Such a plane, which is corresponding to the sheet of the paper, is depicted at the left side of Figure 5. The circled dot and arrow represent the vectors of the perpendicular and parallel polarization components associated with the plane, whose directions are from the backside to the front side of the figure and the arrow's direction, respectively [51]. If each scatterer is modeled as a planar boundary, then the directions of the vectors of the perpendicular and parallel polarization components as viewed from the Tx and Rx will be the same within the plane. Since any polarization vector can be expressed as a linear combination of the vectors of perpendicular and parallel polarization components, as shown in the right side of Figure 5, the polarization angle viewed at the Tx will be same as that observed at the Rx in the ideal scenario [51]. For this reason, we call each Tx-scatterer-Rx plane in Figures 4 and 5 a *conservation-of-polarization plane* (CoP-plane).

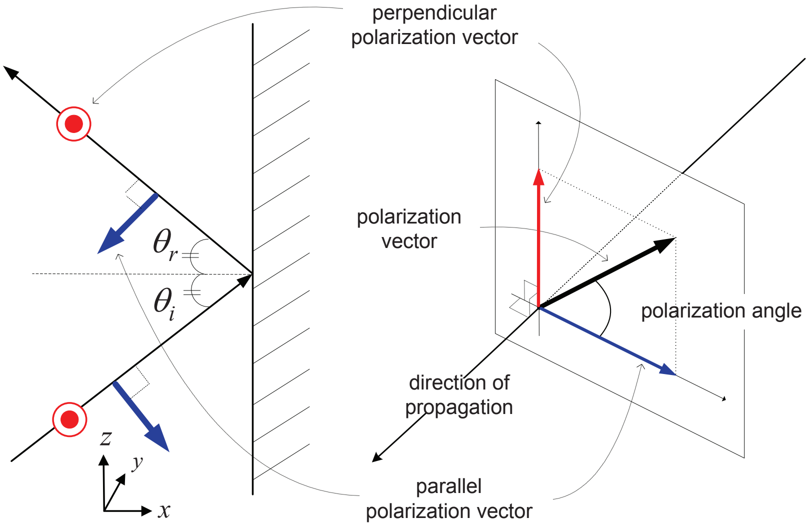

**Figure 5:** Conservation of polarization (CoP) plane and polarization angle.

The polarization angle associated with a CoP-plane, denoted by $\theta_V$ in Figure 4, is defined as the angle between $\underline{V}$ and the line that includes the projection of $\underline{V}$ onto the CoP plane. The angle between $\underline{V}'$ and the line that includes the projection of $\underline{V}'$ onto the same CoP plane in Figure 4 is equal to $\pi - \theta_V$ according to the conservation of polarization principle in the ideal case [51]. Thus, by using the polarization angle with respect to the CoP-plane, the polarization vector, $\underline{V}$' on its CoP-plane can be decomposed into vertical and horizontal polarization components with respect to the plane wave's direction of propagation at the Rx. Consider a vertically polarized plane wave from the Tx, and let $A_{VV}$ ($A_{HV}$) be the amplitude of the received plane wave at a vertically (horizontally) polarized Rx antenna via a single scatterer. The geometry in Figure 4 implies that $A_{VV}$ and $A_{HV}$ can be expressed as a function of $D$, $D_{ts}$, $D_{sr}$, $R_r$, $\alpha_R$, and $\beta_R$ as follows:

$$\begin{bmatrix} A_{VV} \\ A_{HV} \end{bmatrix} = A_V \begin{bmatrix} f_{VV}(D, D_{ts}, D_{sr}, R_r, \alpha_R, \beta_R) \\ f_{HV}(D, D_{ts}, D_{sr}, R_r, \alpha_R, \beta_R) \end{bmatrix}, \tag{2}$$

where $A_V$ is the amplitude of $\underline{V}$' at the Rx. For SBR plane waves, the azimuth and elevation angles-of-departure (AAoDs and EAoDs) from the Tx are dependent on, and are fixed by the AAoAs and EAoAs at the Rx; therefore, the channel-polarization functions $f_{VV}$ and $f_{HV}$ in (74) do not depend on $\alpha_T$ and $\beta_T$. In a similar fashion, for the case of a horizontally polarized plane wave from the Tx:

$$\begin{bmatrix} A_{VH} \\ A_{HH} \end{bmatrix} = A_H \begin{bmatrix} f_{VH}(D, D_{ts}, D_{sr}, R_r, \alpha_R, \beta_R) \\ f_{HH}(D, D_{ts}, D_{sr}, R_r, \alpha_R, \beta_R) \end{bmatrix}, \tag{3}$$

where $A_H$ is the amplitude of $\underline{H}$' at the Rx. From the geometry in Figure 4, the distances are,

$$d_t = \sqrt{(D + R_r \cos\alpha_R)^2 + (R_r \sin\alpha_R)^2}, \tag{4}$$

$$D_{ts} = \sqrt{{d_t}^2 + (\Delta_h - R_r \tan\beta_R)^2}, \tag{5}$$

$$D_{sr} = R_r / \cos\beta_R, \;\; d_1 = R_r \tan\beta_R, \tag{6}$$

$$D_{tr} = \sqrt{D^2 + {\Delta_h}^2}, \;\; d_2 = \sqrt{{d_t}^2 + {\Delta_h}^2}, \tag{7}$$

where $\Delta_h = (h_T - h_R)$. Based on (4) – (7) and the law of cosines, the angles in

Figure 4 can be written as

$$\cos\theta_3 = \frac{{D_{ts}}^2 + {D_{tr}}^2 - {D_{sr}}^2}{2D_{ts}D_{tr}} = \frac{a_2 - a_3 + a_4}{\sqrt{\left({a_1}^2 + 2a_2 - 2a_3 + a_4\right) a_4}} \ , \tag{8}$$

$$\cos\theta_4 = \frac{{D_{ts}}^2 + {d_2}^2 - {d_1}^2}{2D_{ts}d_2} = \frac{2a_2 - a_3 + a_4 + {a_5}^2}{\sqrt{\left({a_1}^2 + 2a_2 - 2a_3 + a_4\right)\left(2a_2 + a_4 + {a_5}^2\right)}} \ , \tag{9}$$

$$\cos\theta_5 = \frac{{d_2}^2 + {D_{tr}}^2 - {R_r}^2}{2d_2D_{tr}} = \frac{a_2 + a_4}{\sqrt{\left(2a_2 + a_4 + {a_5}^2\right) a_4}} \ , \tag{10}$$

$$\cos\theta_6 = \frac{\cos\theta_5 - \cos\theta_3\cos\theta_4}{\sqrt{\left(1 - \cos^2\theta_3\right)\left(1 - \cos^2\theta_4\right)}}, \qquad \theta_V = \pi - \theta_6, \tag{11}$$

$$\cos\theta_7 = \frac{{D_{sr}}^2 + {D_{tr}}^2 - {D_{ts}}^2}{2D_{sr}D_{tr}} = \frac{\left(-a_2 + a_3\right)\cos\beta_R}{\sqrt{a_4}\ a_5} \ , \tag{12}$$

$$\cos\theta_8 = \frac{{D_{tr}}^2 + {R_r}^2 - {d_2}^2}{2D_{tr}R_r} = \frac{-\cos\alpha_R}{\sqrt{a_4}}, \tag{13}$$

$$\cos\theta_9 = \frac{\cos\theta_8 - \cos\theta_7\cos\beta_R}{\sqrt{\left(1 - \cos^2\theta_7\right)\left(1 - \cos^2\beta_R\right)}}, \tag{14}$$

where,

$$a_1 = \frac{R_r/D}{\cos\beta_R} \ , \ a_2 = \frac{R_r}{D}\cos\alpha_R, \ a_3 = \frac{R_r\Delta_h}{D^2}\tan\beta_R \ , \ a_4 = 1 + \left(\frac{\Delta_h}{D}\right)^2 , \ a_5 = \frac{R_r}{D} \ . \tag{15}$$

The angles $\cos\theta_6$ and $\cos\theta_9$ in (82) and (85), respectively, can be used to derive the channel polarization functions, $f_{VV}$, $f_{HV}$, $f_{HH}$ and $f_{VH}$ in (74) and (3) as will be described in the sequel.

From the geometry in Figure 4, the amplitudes of the vertical and horizontal polarization components that are received from a vertically polarized transmitted plane wave are, respectively,

$$\begin{aligned} A_{VV} &= A_V \left|\cos\left(\theta_9 + \left(\pi - \theta_V\right) - \pi\right)\right| \qquad (16) \\ &= A_V \left|\cos\theta_6\cos\theta_9 - \sqrt{1 - \cos^2\theta_6}\sqrt{1 - \cos^2\theta_9}\right| \ , \\ A_{HV} &= A_V \left|\sin\left(\theta_9 + \left(\pi - \theta_V\right) - \pi\right)\right| \qquad (17) \\ &= A_V \left|\cos\theta_6\sqrt{1 - \cos^2\theta_9} + \cos\theta_9\sqrt{1 - \cos^2\theta_6}\right| \ , \end{aligned}$$

where $\cos\theta_6$ and $\cos\theta_9$ in (86) and (87) are functions of $D$, $R_r$, $\alpha_R$ and $\beta_R$ as is evident from (79) – (85). Comparing (86) and (87) with (74), the channel-polarization functions, $f_{VV}$ and $f_{HV}$, can be written as:

$$\begin{aligned} f_{VV}(D, D_{ts}, D_{sr}, R_r, \alpha_R, \beta_R) &\equiv f_{VV}(D, R_r, \alpha_R, \beta_R) \\ &= \left|\cos\theta_6 \cos\theta_9 - \sqrt{1-\cos^2\theta_6}\sqrt{1-\cos^2\theta_9}\right| \ , \quad (18) \\ f_{HV}(D, D_{ts}, D_{sr}, R_r, \alpha_R, \beta_R) &\equiv f_{HV}(D, R_r, \alpha_R, \beta_R) \\ &= \left|\cos\theta_6 \sqrt{1-\cos^2\theta_9} + \cos\theta_9\sqrt{1-\cos^2\theta_6}\right| \ . \quad (19) \end{aligned}$$

In a similar fashion, the channel polarization functions, $f_{HH}$ and $f_{VH}$, can be written as:

$$\begin{aligned} f_{VH}(D, D_{ts}, D_{sr}, R_r, \alpha_R, \beta_R) &\equiv f_{VH}(D, R_r, \alpha_R, \beta_R) \\ &= \left|\cos\theta_6 \sqrt{1-\cos^2\theta_9} + \cos\theta_9\sqrt{1-\cos^2\theta_6}\right|, \quad (20) \\ f_{HH}(D, D_{ts}, D_{sr}, R_r, \alpha_R, \beta_R) &\equiv f_{HH}(D, R_r, \alpha_R, \beta_R) \\ &= \left|\cos\theta_6 \cos\theta_9 - \sqrt{1-\cos^2\theta_6}\sqrt{1-\cos^2\theta_9}\right|. \quad (21) \end{aligned}$$

Note that a symmetry exists in the co and cross-polarization functions such that

$$f_{VV} = f_{HH}, \ \ f_{HV} = f_{VH} \ . \quad (22)$$

### 3.1.3 XPD in F2M Multi-path Fading Channels

The polarized channels in Figure 4 can be modeled by combining the channel-polarization functions with the conventional copolarized channel-impulse-response functions that have been derived previously in the literature for the exact same 3-D single-cylinder scattering geometry shown in Figure 4 [26]. The case of vertically polarized Tx and Rx antennas (VV-channel) are first considered. The complex channel impulse response for the VV-channel can be expressed as

$$g_{VV}(t) = g_{VV}^{SBR}(t) + g_{VV}^{LoS}(t), \quad (23)$$

where the diffusive-SBR and LoS components are, respectively, expressed as

$$\begin{aligned} g_{VV}^{SBR}(t) &= \sum_{n=1}^{N} A_{V,n} f_{VV,n} \ e^{j\phi_n(t)}, \\ g_{VV}^{LoS}(t) &= A_V^{LoS} \ e^{j\phi^{LoS}(t)}, \quad (24) \end{aligned}$$

and

$$A_{V,n} = A_V(\alpha_{R,n}, \beta_{R,n}), \quad f_{VV,n} = f_{VV}(D, R_r, \alpha_{R,n}, \beta_{R,n}) \ , \tag{25}$$

$$\phi_n(t) = 2\pi(f_c + f_{D,n}) \Big( t - (D_{ts,n} + D_{sr,n})/c_0 \Big) + \phi_n \ , \tag{26}$$

$$\phi^{LoS}(t) = 2\pi(f_c + f_D^{LoS})\,(t - D_{tr}/c_0)\,, \tag{27}$$

$$f_c = c_0/\lambda, \quad f_{D,n} = (v_R/\lambda)\cos\beta_{R,n}\cos\left(\gamma_R - \alpha_{R,n}\right), \tag{28}$$

$$f_D^{LoS} = \frac{D}{\sqrt{D^2 + {\Delta_h}^2}}\,(v_R/\lambda)\cos\left(\gamma_R - \pi\right). \tag{29}$$

Here, $c_0$, $\lambda$, $v_R$, and $\gamma_R$ are the velocity of light, the carrier wavelength, the velocity of the Rx and the angle of the Rx's moving direction with respect to the positive $x$-axis, respectively. Further, $f_c$ and $f_{D,n}$ are the carrier and Doppler frequencies associated with the $n$-th arriving plane wave, respectively. Note that the Rx is considered to be in the center of the scattering cylinder regardless of the physical location and velocity of the Rx, which is a typical assumption in geometrical channel modeling. Of course, the exact location of the scatterers on the cylinder will change with the physical location of the Rx because of site-specific propagation conditions. In this case, the channel is modeled as being *locally* wide-sense stationary, i.e., the locations of the scatterers with respect to the Rx will stay the same if the Rx moves over the small distance.

It is assumed that the phases $\{\phi_n\}$ in (26) are independent and identically distributed (i.i.d.) uniform random variables on the interval $[-\pi, \pi)$, and the $\{\phi_n\}$ are independent of the AAoAs $\{\alpha_{R,n}\}$, EAoAs $\{\beta_{R,n}\}$ and the radii of the scattering cylinder. For large $N$, the central-limit theorem can be invoked, and $g_{VV}(t)$ can be treated as a complex Gaussian-random process. By using the complex channel impulse response and the aforementioned properties, it is straightforward to obtain the received power through the VV-channel at the Rx as follows:

$$\begin{aligned}
P_{VV} &= P_{VV}^{SBR} + P_{VV}^{LoS} = (1+K)\, P_{VV}^{SBR} \ , && (30)\\
P_{VV}^{SBR} &= \frac{1}{2}\, \mathrm{E}\left[ |g_{VV}^{SBR}(t)|^2 \right] \\
&= \frac{1}{2}\, \mathrm{E}\left[ \left( \sum_{n=1}^{N} A_{V,n} f_{VV,n}\ e^{j\phi_n(t)} \right) \left( \sum_{m=1}^{N} A_{V,n} f_{VV,n}\ e^{-j\phi_m(t)} \right) \right] \\
&= \frac{1}{2}\, \mathrm{E}\left[ \sum_{n=1}^{N} A_{V,n}^2 f_{VV,n}^2 \right] , && (31)\\
P_{VV}^{LoS} &= \frac{1}{2}\ \left| A_V^{LoS} \right|^2 = K P_{VV}^{SBR} \ , && (32)
\end{aligned}$$

where $K$ denotes the Ricean K-factor, and the third equality in (31) is due to the fact that the phases $\{\phi_n\}$ in (26) are i.i.d. uniform-random variables on the interval $[-\pi, \pi)$. Further, as $N \to \infty$, the discrete AAoAs, $\alpha_{R,n}$, and discrete EAoAs, $\beta_{R,n}$, can be replaced with continuous random variables, $\alpha_R$ and $\beta_R$ having the joint pdf, $f(\alpha_R, \beta_R)$. Here, it is assumed that the AAoA and EAoA are independent of each other; therefore, the joint pdf $f(\alpha_R, \beta_R)$ can be decomposed as $f(\alpha_R)f(\beta_R)$. It follows that

$$P_{VV}^{SBR} = \frac{A_V^2}{2} \int_{-\pi}^{\pi} \int_{-\beta_{R,Max}}^{\beta_{R,Max}} f_{VV}^2(D, R_r, \alpha_R, \beta_R)\ p_r\left(\beta_R\right) p_r\left(\alpha_R\right)\ d\beta_R d\alpha_R \ , \quad (33)$$

where $\beta_{R,Max}$ is the absolute value of the maximum EAoA.

Several different distributions have been suggested in the literature to characterize the AAoA distribution, e.g., uniform, Gaussian and Laplacian distributions. The von Mises distribution is used in this proposal, and it is defined as [52]

$$p_r\left(\alpha_R\right) = \frac{\exp[k_R \cos(\alpha_R - \mu_R)]}{2\pi I_0(k_R)} \ , \ k_R \geq 0 \ , \quad (34)$$

where $\alpha_R \in [-\pi, \pi)$, $I_0(\ \cdot\ )$ is the zero-order-modified Bessel function of the first kind, $\mu_R \in [-\pi, \pi)$ is the mean AAoA of the scatterers in the $x$-$y$ plane with respect to the positive $x$-axis, and $k_R$ controls the spread of the scatterers around the mean AAoA, $\mu_R$. When $k_R = 0$ the von Mises distribution reduces to the uniform distribution, $p_r(\alpha_R) = 1/(2\pi)$, which corresponds to isotropic azimuthal scattering, while as $k_R$ increases the AAoA distribution becomes increasingly non-isotropic and concentrated around the mean AAoA, $\mu_R$ [52]. Prior works have also used several different distributions to characterize the EAoA distribution. Here, the cosine pdf is used as [50]

$$p_r(\beta_R) = \frac{\pi}{4\beta_{R,Max}} \cos\left(\frac{\pi}{2}\frac{\beta_R}{\beta_{R,Max}}\right) \ , \quad |\beta_R| \leq \beta_{R,Max} \leq \pi/2 \ , \tag{35}$$

where $\beta_{R,Max}$ typically lies in the range, $20^\circ < \beta_{R,Max} < 45^\circ$ for F2M land mobile radio channels [7,50,53]. Of course, other suitable distributions for $p_r(\alpha_R)$ and $p_r(\beta_R)$ can be used as well at this stage.

In a similar manner with (33), the power of SBR components at the Rx with a horizontally polarized Rx antenna and a vertically polarized Tx antenna (HV-channel), a vertically polarized Rx antenna and a horizontally polarized Tx antenna (VH-channel), and horizontally polarized Rx and Tx antennas (HH-channel), which are denoted by $P_{HV}$, $P_{VH}$, and $P_{HH}$, respectively, can be expressed as

$$P_{HV}^{SBR} = \frac{A_V^2}{2}\int_{-\pi}^{\pi}\int_{-\beta_{R,Max}}^{\beta_{R,Max}} f_{HV}^2(D, R_r, \alpha_R, \beta_R)\ p_r(\beta_R)\, p_r(\alpha_R)\ d\beta_R d\alpha_R \ , \tag{36}$$

$$P_{VH}^{SBR} = \frac{A_H^2}{2}\int_{-\pi}^{\pi}\int_{-\beta_{R,Max}}^{\beta_{R,Max}} f_{VH}^2(D, R_r, \alpha_R, \beta_R)\ p_r(\beta_R)\, p_r(\alpha_R)\ d\beta_R d\alpha_R \ , \tag{37}$$

$$P_{HH}^{SBR} = \frac{A_H^2}{2}\int_{-\pi}^{\pi}\int_{-\beta_{R,Max}}^{\beta_{R,Max}} f_{HH}^2(D, R_r, \alpha_R, \beta_R)\ p_r(\beta_R)\, p_r(\alpha_R)\ d\beta_R d\alpha_R \ . \tag{38}$$

Notice that by taking into account the statistical distribution of scatterers, the total power of the vertical and horizontal polarization components can be derived via the superposition of the CoP-plane components by averaging over the pdfs of the AAoA and EAoA, $p(\alpha_R)$ and $p(\beta_R)$, respectively. Finally, the average-XPD values are obtained from (33) and (36) – (38) as

$$\overline{XPD}_{VV/HV}^{F2M} = \frac{P_{VV}}{P_{HV}} \ , \ \overline{XPD}_{HH/VH}^{F2M} = \frac{P_{HH}}{P_{VH}} \ . \tag{39}$$

## *3.2 Channel Depolarization and XPD Reference Model for M2M Channels*

This section extends the methodology of the previous section to obtain a 3-D geometry-based double-cylinder XPD reference model for narrow-band LoS or NLoS-M2M channels.

### 3.2.1 3-D Double-cylindrical XPD Reference Model

As shown in Figures 6 and 7, the proposed M2M scattering model assumes that scatterers are distributed on cylindrical surfaces in the vicinity of both the Tx and Rx. This geometry results in four different propagation modes; line-of-sight (LoS), single-bounced transmitter-side (SBT), single-bounced receiver-side (SBR) and double-bounced (DB) modes. The LoS and SBR modes are same as those in Figure 4, except that the elevation of the Tx antenna is low like that of the Rx antenna. The SBT and DB modes in M2M channels are portrayed in Figures 6 and 7, respectively. The scattering cylinders are characterized by their radii, $R_t$ and $R_r$, and the AAoA, $\alpha_R$, and EAoA, $\beta_R$, are defined in the same fashion as in Section 3.1. Further, the plane wave emitted from the Tx and reflected from each scatterer on the cylindrical surface in the vicinity of the Tx has an AAoD, $\alpha_T$, and EAoD, $\beta_T$. Hence, the XPD of each arriving plane wave at the Rx antenna can be derived as a function of $\alpha_R$, $\beta_R$, $R_r$, $\alpha_T$, $\beta_T$, $R_t$ and the distance between the Tx and Rx antennas, $D$. Afterwards, the mean XPD can be computed based on the scattering distributions for $\alpha_R$, $\beta_R$, $\alpha_T$ and $\beta_T$.

### 3.2.2 Polarization Functions for the SBT Propagation Mode

The mechanism of the SBT propagation mode is portrayed in Figure 6. The vector $\underline{V}_{SBT}$ in Figure 6 stands for the vertical polarization vector of a wave from the Tx, and $\underline{V}'_{SBT}$ is the corresponding polarization vector of the wave after reflection from a transmitter-side scatterer in the vicinity of the Tx. It is clear that $\underline{V}'_{SBT}$ has cross-polarization components. Similar to the SBR propagation mode described in

Section 3.1, the cross-polarization components arising from the SBT propagation mode tend to be dominated by $\alpha_T$ and $\beta_T$ as opposed to $R_t$ and $D$. The same phenomenon happens when a horizontally polarized antenna is used at the Tx, but it is omitted due to the complexity of the figure.

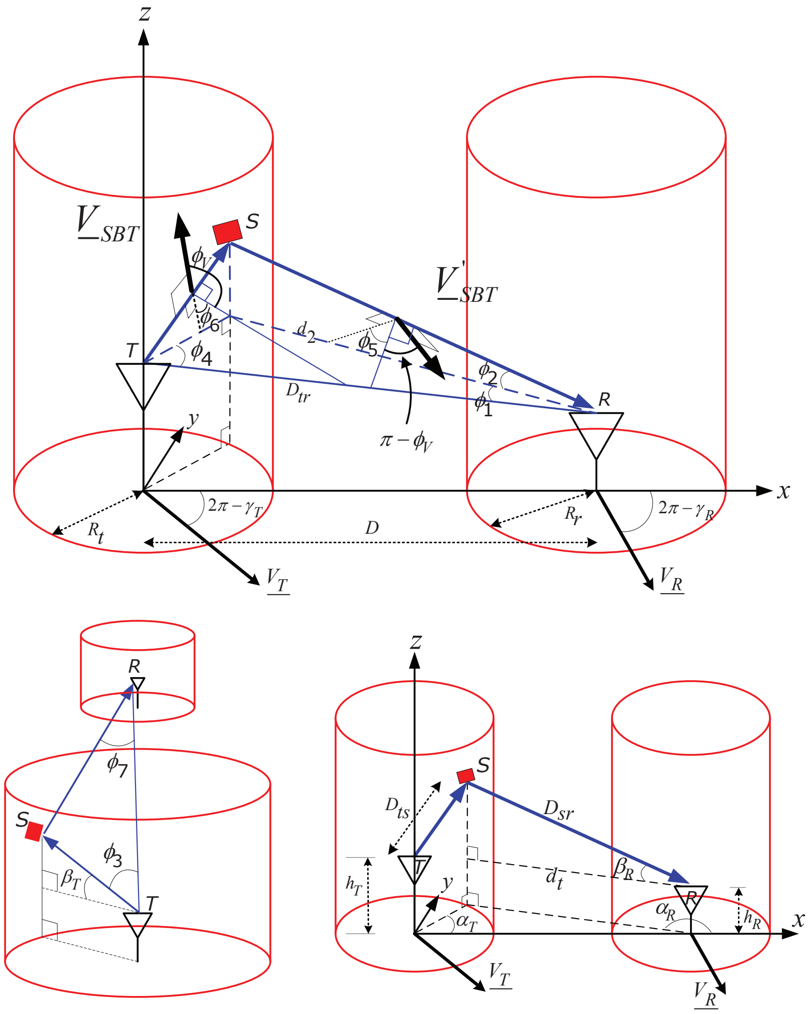

**Figure 6:** Single-bounced transmit-side (SBT) propagation mode for XPD on narrowband M2M channels.

A single vertically polarized SBT plane wave from the Tx is first considered. The CoP-plane for the SBT propagation mode consists of the Tx, Rx and the scatterer on the cylindrical surface around the Tx. The polarization angle of $\underline{V}_{SBT}$, $\phi_V$, in Figure 6 is defined as the angle between $\underline{V}_{SBT}$ and the line that includes the projection of $\underline{V}_{SBT}$

onto the corresponding CoP-plane. Then the angle between $\underline{V}'_{SBT}$ and a line that includes its projection onto the CoP-plane is equal to $\pi - \phi_V$, as stated in Sect. 3.1 [51]. The polarization vector, $\underline{V}'_{SBT}$ for a given CoP-plane can be decomposed into vertical and horizontal polarization components at the Rx antenna. Define $A_{VV}^{SBT}$ and $A_{HV}^{SBT}$ as the amplitude of the received SBT plane wave at a vertically and horizontally polarized Rx antenna, respectively. The geometry in Figure 6 implies that $A_{VV}^{SBT}$ and $A_{HV}^{SBT}$ can be expressed as a function of $D$, $D_{ts}$, $D_{sr}$, $R_t$, $\alpha_T$ and $\beta_T$ as:

$$\begin{bmatrix} A_{VV}^{SBT} \\ A_{HV}^{SBT} \end{bmatrix} = A_V \begin{bmatrix} f_{VV}^{SBT}(D, D_{ts}, D_{sr}, R_t, \alpha_T, \beta_T) \\ f_{HV}^{SBT}(D, D_{ts}, D_{sr}, R_t, \alpha_T, \beta_T) \end{bmatrix}, \tag{40}$$

where $A_V$ is the amplitude of $\underline{V}'_{SBT}$ at the Rx antenna. For SBT plane waves, the AoAs are dependent on and are fixed by the AoDs and, thus, (40) does not include $\alpha_R$ and $\beta_R$. In a similar fashion, the following two equations can be derived in the case of a horizontally polarized plane wave from the Tx antenna:

$$\begin{bmatrix} A_{VH}^{SBT} \\ A_{HH}^{SBT} \end{bmatrix} = A_H \begin{bmatrix} f_{VH}^{SBT}(D, D_{ts}, D_{sr}, R_t, \alpha_T, \beta_T) \\ f_{HH}^{SBT}(D, D_{ts}, D_{sr}, R_t, \alpha_T, \beta_T) \end{bmatrix}, \tag{41}$$

where $A_H$ is the amplitude of the horizontally polarized plane wave at the Rx antenna.

From the geometry in Figure 6, the amplitudes of the vertical and horizontal polarization components at the Rx antenna in (40) are, respectively,

$$\begin{aligned} A_{VV}^{SBT} &= A_V \left|\cos\left(\phi_5 + (\pi - \phi_V) - \pi\right)\right| \qquad (42) \\ &= A_V \left|\cos\phi_6 \cos\phi_5 - \sqrt{1-\cos^2\phi_6}\sqrt{1-\cos^2\phi_5}\right|, \\ A_{HV}^{SBT} &= A_V \left|\sin\left(\phi_5 + (\pi - \phi_V) - \pi\right)\right| \qquad (43) \\ &= A_V \left|\cos\phi_6 \sqrt{1-\cos^2\phi_5} + \cos\phi_5\sqrt{1-\cos^2\phi_6}\right|. \end{aligned}$$

From (216) – (226) in Appendix A, $\cos\phi_5$ and $\cos\phi_6$ in (42) – (43) can be expressed as a function of $D$, $R_t$, $\alpha_T$ and $\beta_T$. Comparing (42) – (43) with (40), the channel polarization functions $f_{VV}^{SBT}$ and $f_{HV}^{SBT}$ can be written as:

$$\begin{aligned}
&f_{VV}^{SBT}(D, D_{ts}, D_{sr}, R_t, \alpha_T, \beta_T) \\
&\equiv f_{VV}^{SBT}(D, R_t, \alpha_T, \beta_T) \\
&= \left|\cos\phi_6 \cos\phi_5 - \sqrt{1-\cos^2\phi_6}\sqrt{1-\cos^2\phi_5}\right|, \qquad (44) \\
&f_{HV}^{SBT}(D, D_{ts}, D_{sr}, R_t, \alpha_T, \beta_T) \\
&\equiv f_{HV}^{SBT}(D, R_t, \alpha_T, \beta_T) \\
&= \left|\cos\phi_6 \sqrt{1-\cos^2\phi_5} + \cos\phi_5 \sqrt{1-\cos^2\phi_6}\right|. \qquad (45)
\end{aligned}$$

Similar to the SBR propagation mode, a symmetry exists in the channel polarization functions such that

$$f_{VH}^{SBT} = f_{HV}^{SBT}, \;\; f_{HH}^{SBT} = f_{VV}^{SBT} \;\; . \qquad (46)$$

### 3.2.3 Polarization Functions for the DB Propagation Mode

The channel-polarization functions of the DB propagation mode can be obtained by treating the DB propagation mode as a combination of the SBT and SBR propagation modes, as illustrated in Figure 7. First, the CoP-plane of the SBT-like propagation mode with the Rx antenna replaced by the receiver-side scatterer, $S_r$, is considered, and the change in the polarization vector after the plane wave is reflected from the transmitter-side scatterer, $S_t$, is computed. Second, the CoP-plane of the SBR-like propagation mode with the Tx replaced by the transmitter-side scatterer, $S_t$, is considered, and the change in the polarization vector after the plane wave is reflected from the receiver-side scatterer, $S_r$ is computed. Furthermore, the angle between the two CoP-planes defined by the common line $S_t$–$S_r$ is $|\theta_6' - \phi_5'|$; therefore, the total change in the polarization vector for each DB component can be computed.

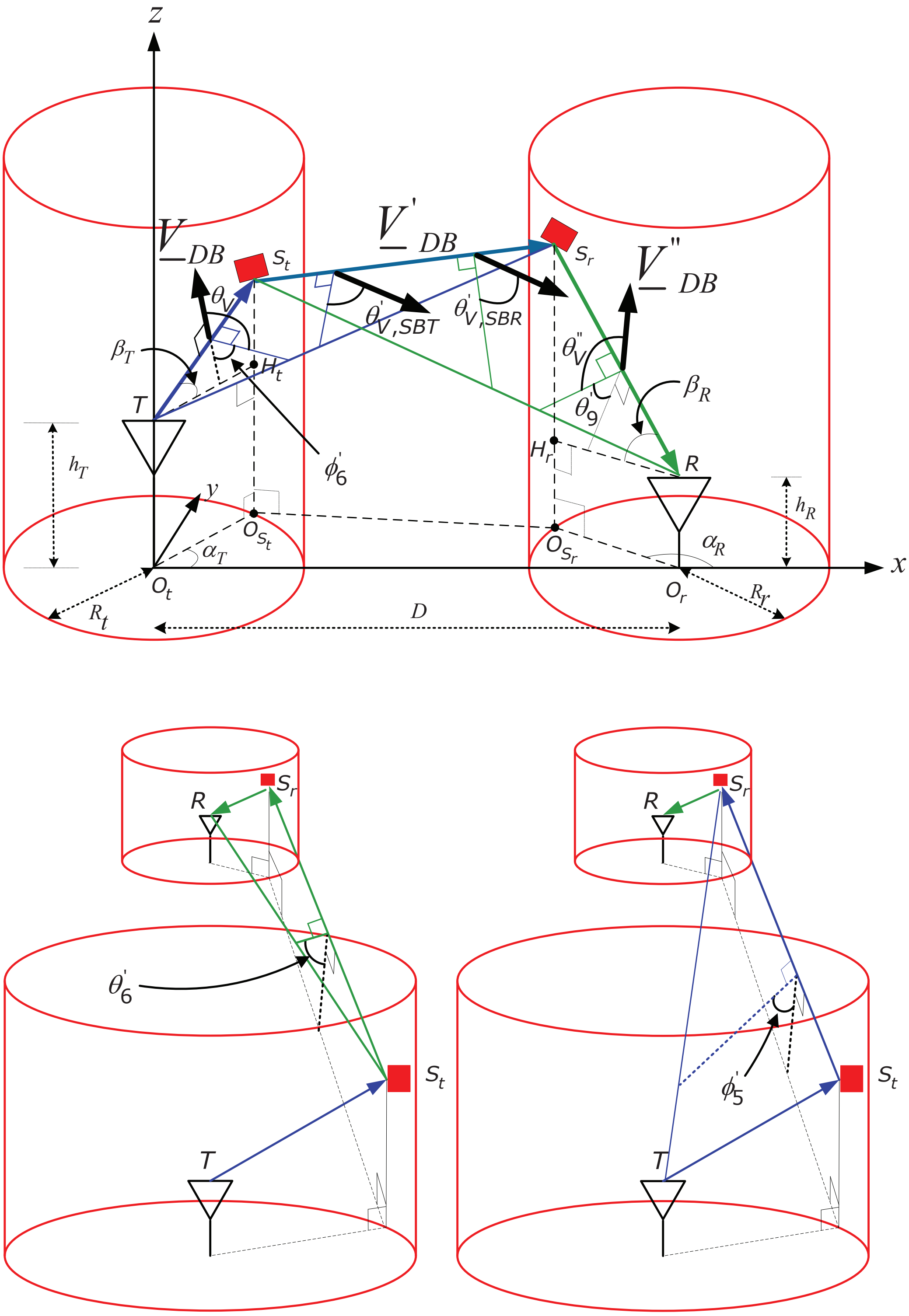

**Figure 7:** Double-bounced (DB) propagation mode for XPD on narrow-band M2M channels.

In a manner similar to the SBT and SBR propagation modes described earlier, the geometry in Figure 7 yields the DB channel polarization functions:

$$\begin{aligned}
&f_{VV}^{DB}(D, R_t, R_r, \alpha_T, \beta_T, \alpha_R, \beta_R) \\
&= \left|\cos\left(\theta_9' + \theta_V'' - \pi\right)\right| \\
&= \left|\cos\left(\theta_9' + \left(\pi - \theta_{V,SBR}'\right) - \pi\right)\right| \\
&= \left|\cos\left(\theta_9' + \left[\pi - \{\phi_5' + (\pi - \theta_V) - \theta_6'\}\right] - \pi\right)\right| \\
&= \left|\cos\left((\theta_9' + \theta_6') - (\phi_5' + \phi_6')\right)\right| \\
&= \Big|\left(\cos\theta_9'\cos\theta_6' - \sin\theta_9'\sin\theta_6'\right)\left(\cos\phi_5'\cos\phi_6' - \sin\phi_5'\sin\phi_6'\right) + \\
&\quad \left(\sin\theta_9'\cos\theta_6' + \cos\theta_9'\sin\theta_6'\right)\left(\sin\phi_5'\cos\phi_6' + \cos\phi_5'\sin\phi_6'\right)\Big|,
\end{aligned} \tag{47}$$

$$\begin{aligned}
&f_{HV}^{DB}(D, R_t, R_r, \alpha_T, \beta_T, \alpha_R, \beta_R) \\
&= \left|\sin\left(\theta_9' + \theta_V'' - \pi\right)\right| \\
&= \left|\sin\left((\theta_9' + \theta_6') - (\phi_5' + \phi_6')\right)\right| \\
&= \Big|\left(\sin\theta_9'\cos\theta_6' + \sin\theta_9'\cos\theta_6'\right)\left(\cos\phi_5'\cos\phi_6' - \sin\phi_5'\sin\phi_6'\right) - \\
&\quad \left(\cos\theta_9'\cos\theta_6' - \sin\theta_9'\sin\theta_6'\right)\left(\sin\phi_5'\cos\phi_6' + \cos\phi_5'\sin\phi_6'\right)\Big|.
\end{aligned} \tag{48}$$

Note that for angles $\theta_6'$, $\theta_9'$, $\phi_5'$, and $\phi_6'$, which are within the range 0° to 180°, the $\sin(\,\cdot\,)$ functions in (47) and (48) can be rewritten in the form $\sqrt{1-\cos^2(\,\cdot\,)}$, where the $\cos(\,\cdot\,)$ functions depend on $\alpha_R$, $\beta_R$, $\alpha_T$, $\beta_T$, $R_r$, $R_t$, and $D$ as shown in Appendix B. Similar to the SBT and SBR channel polarization functions, the DB channel polarization functions have the symmetry

$$f_{VV}^{DB} = f_{HH}^{DB},\ f_{HV}^{DB} = f_{VH}^{DB}\ . \tag{49}$$

### 3.2.4 XPD in M2M Multi-path Fading Channels

The M2M polarized channels can be modeled by using the channel-polarization functions for the SBR propagation mode in (88) – (91), the SBT propagation mode in

(44) – (46), and the DB propagation mode in (47) – (48) along with the conventional copolarized-channel impulse response previously derived in the literature for the exact same 3-D double-cylinder scattering geometry [25,26]. Consider, for example, the case of vertically polarized Tx and Rx antennas (VV-channel). The complex channel impulse response for a VV-channel with SBT, SBR, DB and LoS propagation modes can be expressed as

$$g_{VV}^{M2M}(t) = g_{VV}^{SBR}(t) + g_{VV}^{SBT}(t) + g_{VV}^{DB}(t) + g_{VV}^{LoS}(t) \ , \tag{50}$$

where

$$g_{VV}^{SBR}(t) = \sum_{n=1}^{N_1} \left( A_{V,n}^{SBR} f_{VV,n}^{SBR} \ e^{j\phi_n^{SBR}(t)} \right), \quad g_{VV}^{SBT}(t) = \sum_{n=1}^{N_2} \left( A_{V,n}^{SBT} f_{VV,n}^{SBT} \ e^{j\phi_n^{SBT}(t)} \right), \tag{51}$$

$$g_{VV}^{DB}(t) = \sum_{n=1}^{N_3} \left( A_{V,n}^{DB} f_{VV,n}^{DB} \ e^{j\phi_n^{DB}(t)} \right), \quad g_{VV}^{LoS}(t) = A_V^{LoS} \ e^{j\phi^{LoS}(t)}, \tag{52}$$

and the amplitudes and phases are

$$A_{V,n}^{SBR} = A_V^{SBR}(\alpha_{R,n}, \beta_{R,n}), \quad A_{V,n}^{SBT} = A_V^{SBT}(\alpha_{T,n}, \beta_{T,n}), \tag{53}$$

$$A_{V,n}^{DB} = A_V^{DB}(\alpha_{R,n}, \beta_{R,n}, \alpha_{T,n}, \beta_{T,n}), \tag{54}$$

$$\phi_n^{\text{case}}(t) = 2\pi(f_c + f_{D,n}^{\text{case}}) \left( t - (D_{ts,n}^{\text{case}} + D_{sr,n}^{\text{case}})/c_0 \right) + \phi_n^{\text{case}}, \ \text{for case} \in \{SBT, SBR\}, \tag{55}$$

$$\phi_n^{DB}(t) = 2\pi(f_c + f_{D,n}^{DB}) \left( t - (D_{TS_t,n}^{DB} + D_{S_tS_r}^{DB} + D_{S_rR,n}^{DB})/c_0 \right) + \phi_n^{DB}, \tag{56}$$

$$\phi^{LoS}(t) = 2\pi(f_c + f_D^{LoS}) \left( t - D_{tr}/c_0 \right), \tag{57}$$

and the Doppler and carrier frequencies are

$$\begin{aligned} f_{D,n}^{\text{case}} = \ & (v_R/\lambda) \cos\beta_{R,n} \cos(\gamma_R - \alpha_{R,n}) + (v_T/\lambda) \cos\beta_{T,n}^{\text{case}} \cos\left(\gamma_T - \alpha_{T,n}^{\text{case}}\right), \\ & \text{for case} \in \{SBT, SBR, DB\}, \end{aligned} \tag{58}$$

$$f_D^{LoS} = \frac{D}{\sqrt{D^2 + {\Delta_h}^2}} \left( (v_R/\lambda) \cos(\gamma_R - \pi) + (v_T/\lambda) \cos\gamma_T \right) \ , \tag{59}$$

$$f_c = c_0/\lambda \ . \tag{60}$$

Here, $v_T$ and $v_R$ ($\gamma_T$ and $\gamma_R$) are the velocities (moving directions with respect to the positive $x$-axis) of the Tx and Rx, respectively. For large $N_i,\ i = 1, 2, 3$ in (51) and (52), the central-limit theorem can be invoked and $g_{VV}^{M2M}(t)$ in (50) can be treated as complex Gaussian-random process. The term $g_{VV}^{LoS}(t)$ in (50) is the LoS component, and the terms $g_{VV}^{SBR}(t)$, $g_{VV}^{SBT}(t)$ and $g_{VV}^{DB}(t)$ contribute to the diffusive-scattering component of the received complex fading envelope. The channel-polarization functions can be expressed as

$$f_{VV,n}^{\text{case}} = f_{VV}^{\text{case}}\left(D, R_r, R_t, \alpha_{R,n}, \beta_{R,n}, \alpha_{T,n}, \beta_{T,n}\right), \text{ for case} \in \{LoS, SBT, SBR, DB\}. \tag{61}$$

The term $f_{XY}^{SBR}$ with $X, Y \in \{V, H\}$ uses $f_{VV}$, $f_{HV}$, $f_{HH}$ and $f_{VH}$ in (88) – (91). It is assumed that the phases $\{\phi_n^{\text{case}}\}$ with case $\in \{SBT, SBR, DB\}$ are i.i.d. uniform-random variables on the interval $[-\pi, \pi)$, and independent of the A/EAoDs, A/EAoAs and the radii of the cylinders.

In a manner analogous with (30) – (33), the power received at the Rx through the VV-channel can be written as

$$\begin{aligned} P_{VV}^{M2M} &= P_{VV}^{SBR} + P_{VV}^{SBT} + P_{VV}^{DB} + P_{VV}^{LoS} \\ &= (1+K)\left(P_{VV}^{SBR} + P_{VV}^{SBT} + P_{VV}^{DB}\right) \quad , \end{aligned} \tag{62}$$

where

$$P_{VV}^{SBR} = \frac{1}{2}\,\mathrm{E}\left[\left|g_{VV}^{SBR}(t)\right|^2\right] = \frac{1}{2}\,\mathrm{E}\left[\sum_{n=1}^{N_1}\left(A_{V,n}^{SBR} f_{VV,n}^{SBR}\right)^2\right] \quad , \tag{63}$$

$$P_{VV}^{SBT} = \frac{1}{2}\,\mathrm{E}\left[\left|g_{VV}^{SBT}(t)\right|^2\right] = \frac{1}{2}\,\mathrm{E}\left[\sum_{n=1}^{N_2}\left(A_{V,n}^{SBT} f_{VV,n}^{SBT}\right)^2\right] \quad , \tag{64}$$

$$P_{VV}^{DB} = \frac{1}{2}\,\mathrm{E}\left[\left|g_{VV}^{DB}(t)\right|^2\right] = \frac{1}{2}\,\mathrm{E}\left[\sum_{n=1}^{N_3}\left(A_{V,n}^{DB} f_{VV,n}^{DB}\right)^2\right] \quad , \tag{65}$$

$$P_{VV}^{LoS} = \frac{1}{2}\,\left|A_V^{LoS}\right|^2 = K\left(P_{VV}^{SBR} + P_{VV}^{SBT} + P_{VV}^{DB}\right) \quad . \tag{66}$$

Once again, $K$ denotes the Ricean K-factor. Further, as $N_i \to \infty$, we can write

$$P_{VV}^{SBR} = \frac{A_V^2}{2}\eta_{SBR}\int_{-\pi}^{\pi}\int_{-\beta_{R,Max}}^{\beta_{R,Max}} \left\{f_{VV}^{SBR}(D, R_r, \alpha_R, \beta_R)\right\}^2 p_r\left(\beta_R\right) p_r\left(\alpha_R\right)\ d\beta_R d\alpha_R\ , \tag{67}$$

$$P_{VV}^{SBT} = \frac{A_V^2}{2}\eta_{SBT}\int_{-\pi}^{\pi}\int_{-\beta_{T,Max}}^{\beta_{T,Max}} \left\{f_{VV}^{SBT}(D, R_t, \alpha_T, \beta_T)\right\}^2 p_r\left(\beta_T\right) p_r\left(\alpha_T\right)\ d\beta_R d\alpha_R\ , \tag{68}$$

$$\begin{aligned} P_{VV}^{DB} = \frac{A_V^2}{2}\eta_{DB}&\int_{-\pi}^{\pi}\int_{-\beta_{R,Max}}^{\beta_{R,Max}}\int_{-\pi}^{\pi}\int_{-\beta_{T,Max}}^{\beta_{T,Max}} \left\{f_{VV}^{DB}(D, R_t, R_r, \alpha_T, \beta_T, \alpha_R, \beta_R)\right\}^2 \\ &\times p_r\left(\beta_T\right) p_r\left(\alpha_T\right) p_r\left(\beta_R\right) p_r\left(\alpha_R\right) d\beta_T d\alpha_T\ d\beta_R d\alpha_R\ , \end{aligned} \tag{69}$$

where the parameters $\eta_{SBT}$, $\eta_{SBR}$ and $\eta_{DB}$ specify the relative power mixture of the SBT, SBR and DB propagation modes, such that $0 \leq \eta_{SBT}, \eta_{SBR}, \eta_{DB} \leq 1$, and $\eta_{SBT} + \eta_{SBR} + \eta_{DB} = 1$.

The AAoD and EAoD distributions of the SBT or DB waves, $p_t\left(\alpha_T\right)$ and $p_t\left(\beta_T\right)$, respectively, are assumed to have the same forms as the AAoA and EAoA distributions, $p_t\left(\alpha_R\right)$ and $p_t\left(\beta_R\right)$, by Tx – Rx symmetry [50], but the parameters in the distributions may be different. Thus, the AAoD and EAoD distributions are, respectively, modeled as [50, 52]:

$$p_t\left(\alpha_T\right) = \frac{\exp[k_T \cos(\alpha_T - \mu_T)]}{2\pi I_0(k_T)}\ , \quad \alpha_T \in [-\pi, \pi), \quad \mu_T \in [-\pi, \pi), \tag{70}$$

$$p_t\left(\beta_T\right) = \frac{\pi}{4\beta_{T,Max}} \cos\left(\frac{\pi}{2}\frac{\beta_T}{\beta_{T,Max}}\right)\ , \quad |\beta_T| \leq \beta_{T,Max} \leq \pi/2. \tag{71}$$

Here, $\mu_T$, $k_T$ and $\beta_{T,Max}$ are, respectively, the mean AAoD, the spread factor of the AAoD and the maximum EAoD. From empirical measurements, $\beta_{R,Max}$ and $\beta_{T,Max}$ are typically less than $20^\circ$ for M2M channels [50, 53].

Finally, to obtain $P_{HV}^{M2M}$, $P_{HH}^{M2M}$ and $P_{VH}^{M2M}$, we replace $f_{VV}^{\text{case}}$ such that case $\in \{SBT, SBR, DB\}$ in (67) – (69) with $f_{HV}^{\text{case}}$, $f_{HH}^{\text{case}}$ and $f_{VH}^{\text{case}}$, respectively, and $A_V$ is replaced with $A_H$ in the case of $P_{HH}^{M2M}$ or $P_{VH}^{M2M}$. The Ricean $K$-factor is zero for the cross-polarization (VH or HV) components, since these components are due to scattering and contain no LoS component. Finally, the average XPD values are obtained from (62) – (69), and their variants for $P_{HV}^{M2M}$, $P_{HH}^{M2M}$ and $P_{VH}^{M2M}$, as

$$\overline{XPD}_{VV/HV}^{M2M} = \frac{P_{VV}^{M2M}}{P_{HV}^{M2M}} \ , \ \overline{XPD}_{HH/VH}^{M2M} = \frac{P_{HH}^{M2M}}{P_{VH}^{M2M}} \ . \tag{72}$$

## *3.3 Reference Model Validation*

In this section, we compare analytical XPD results derived from our theoretical models developed in Sects. 3.1 and 3.2 with some previously reported XPD results obtained from empirical data [1, 7, 12]. It is shown that our geometrical theory of polarization/depolarization can successfully explain XPD phenomena observed in the measurement data.

### 3.3.1 Default Parameters of the XPD Sounding Campaigns

The empirical XPD data reported in [1,12] were based on narrow-band F2M channel measurements taken in a suburban area at 2.48 GHz, where the corresponding $h_T$ and $h_R$ in Figure 4 were 20 m and 3 m, respectively. On the other hand, the empirical XPD data reported in [7] were obtained in an urban area at 4.5 GHz with several different scenarios in the measurement route and local environment, and $h_T$ and $h_R$ were set to 35 m and 1.6 m. The parameters in (34) – (35) are set as $\mu_R = 180°$ and $\beta_{R,Max} = 40°$, unless otherwise stated, particularly when comparing our analytical XPD results with the XPD measurement data in [1,12]. It is stated in [1,12] that the direction of the strongest signal was the Tx–Rx bore sight path in most cases of their measurements, corresponding to $\mu_R = 180°$ in our model. The spread constant of the AAoA distribution, $k_R$, in (34) can exhibit substantial variation from one location to the next where the measurements were performed due to variations in the local scattering environment around the Rx. Finally, $R_r$ in Figure 4 is set to be 30 m.

### 3.3.2 Comparison of Analytical and Empirical Results-1: Suburban Area in San Jose

Figures 8 and 9 portray the analytical mean-XPD curves of F2M fading channels as $k_R$ varies from 0 to 9 and from 10 to 700, respectively. The same antenna configuration as that in [1,12] is utilized in the analysis to allow for comparison with the measurement data illustrated in Figure 8, which is a ±45° dual-polarization antenna at both the Tx and Rx. Notice that a directional Rx antenna with the azimuthal beamwidth of 90° and a gain of 12 dBi was used in the measurements in [1,12]. The XPD curve tends to decrease from roughly 6.5 dB to 0 dB as $k_R$ increases from 0 to 9 in Figure 8. On the other hand, the XPD curve increases from 0 dB to roughly 7.5 dB as $k_R$ increases from 10 to 700 in Figure 9. The XPD curve for the varying $k_R$ from 0 to 700 at a fixed Tx–Rx distance, $D = 1$ km, is also illustrated in the insert of Figure 9 to further illustrate the effect of $k_R$ on the XPD shown in Figures 8 and 9. The reason for this strong dependency of the mean XPD on $k_R$ will be explained later in detail when discussing Figure 10.

When $k_R$ is in the range 7 to 10, the XPD stays at around 0 dB regardless of the distance between the Tx and Rx, and it can be shown that the AAoA spread in (34) is roughly 90° when $k_R$ is 7 to 10 [52]. As the distance between the Tx and Rx, $D$, increases it is expected that $k_R$ will tend to decrease since the plane waves at the Rx for large distances and NLoS conditions will come from many angles because of local scattering; therefore, the azimuthal scattering will become more isotropic; $k_R = 0$ corresponds to the case of isotropic-azimuthal scattering. However, in the case of isotropic scattering the observed AAoA spread will be determined by the beam pattern of the 90° directional Rx antenna that was used to make the measurements. Thus, while the actual scattering environment may be near isotropic, i.e., $k_R \approx 0$, the observed value of $k_R$ will lay in the range 7 to 10. For this reason, the empirical XPD tends to converge toward 0 dB as $D$ increases, and it is in close agreement with our analytical-XPD results with $k_R$ in the range 7 to 10, as previously stated.

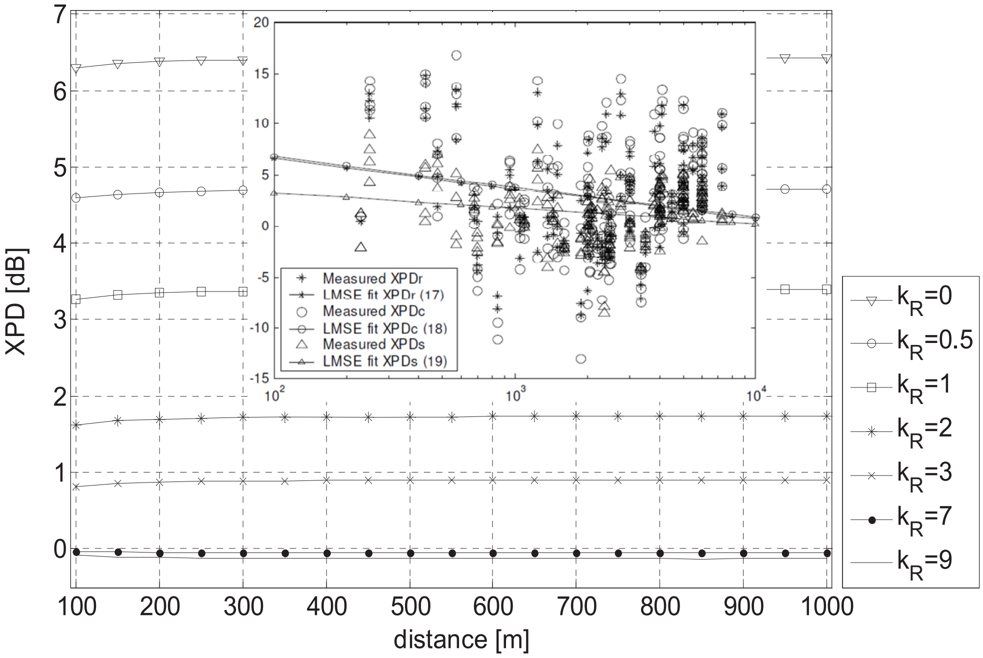

**Figure 8:** $\overline{XPD}^{F2M}$ curves for a variety of $k_R$ $(0 - 9)$ with Tx-Rx distance in the range 100 m to 1 km, and the measurement data in [1].

The AAoA spread factor, $k_R$, is expected to increase as the horizontal Tx–Rx distance, $D$, decreases. As the mobile station moves closer to the base station most of the scatters will tend to be in the direction of the Tx so that $k_R$ will tend to increase, and the scattering will be non-isotropic. If the AAoA distribution is modeled using the von Mises pdf in (34) with $\mu_R = 180°$, then the effective value of $k_R$ will be greater than 7, since a directional antenna with an azimuthal beamwidth of 90° was used in the measurements. Notice that as $k_R$ increases, the azimuthal-angular spread becomes narrower. When the actual AAoA-spread factor, $k_R$, is equal to 3 for example, $p_r(\alpha_R = 180°)|_{k_R=3} \simeq 0.66$, and the effective value of $k_R$ that is due to the directional Rx antenna gain of 12 dBi (15.8 in linear scale) for the direction of Tx–Rx boresight ($\alpha_R = 180°$) is roughly $0.66 \times 15.8 \simeq 10.43$, which is close to $p_r(\alpha_R = 180°)|_{k_R=700} \simeq 10.55$. Hence, while the actual value of the AAoA spread factor may be in the neighborhood of $k_R = 3$, the observed value may be considerably higher and in the range of $k_R = 700$ because of the gain of the directional measurement antenna.

The empirical-XPD data from [1, 12] are illustrated in Figure 8, where $\mathrm{XPD_r}$, $\mathrm{XPD_c}$ and $\mathrm{XPD_s}$ represent the XPD of the total received signal, the XPD of the time-invariant portion of the received signal, and the XPD of the time-varying portion of the received signal. The empirical data in [1, 12] shows that the least-mean-square-error (LMSE) curve fit for the XPD of total received signal is almost same as the XPD for only the time-invariant portion of the received signal. This is expected since the measurements in [1,12] were made with a stationary Rx. Most of the surrounding scatterers will be stationary and contribute to $\mathrm{XPD_c}$, while only the moving scatterers such as nearby-moving vehicles (which are not included in the proposed model) will contribute to $\mathrm{XPD_s}$. It is also shown that the LMSE curve fit of $\mathrm{XPD_r}$ tends to decrease from 6.5 dB to 0 dB as $D$ increases from 100 m to 10 km. This phenomenon can be explained by the XPD curve for varying $k_R$ inserted in Figure 9. A decrease in the effective value of $k_R$ from 550 to 7 corresponds to a decrease in the XPD from 6.5 to 0, as $D$ increases from 100 m to 10 km. Although an LMSE curve fit can be obtained from the measurement data, the measured-XPD values show substantial variation even at the same $D$ as portrayed in Figures 8 and 9. The reason is that the AAoA-spread factor, $k_R$, varies depending on the site-specific local scattering environment, even at the same $D$. The XPD is not directly dependent on $D$, but $k_R$ is expected to have a tendency to decrease with increasing $D$ as mentioned earlier, which is reflected on the LMSE curve in the illustrated empirical results. Finally, the analytical XPD curves in the range 1 km to 10 km are omitted from Figures 8 and 9, since the XPD remains constant after 1 km.

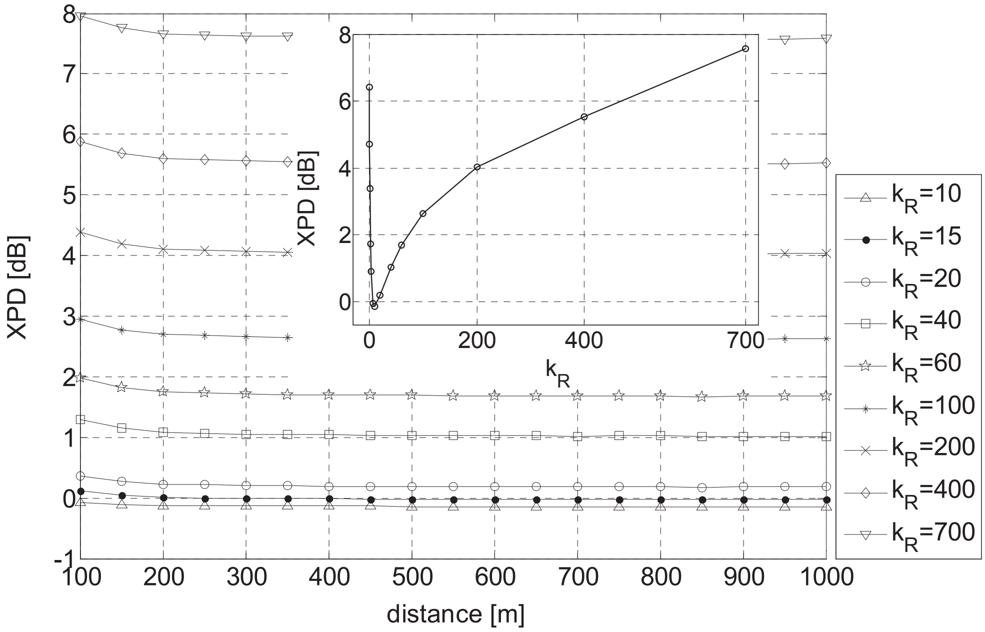

**Figure 9:** $\overline{XPD}^{F2M}$ curves for a variety of $k_R$ (10 – 700) with Tx-Rx distance in the range 100 m to 1 km.

The AAoA, $\alpha_R$, has a significant impact on the XPD as shown in Figure 10, and computing the XPD as a function of $\alpha_R$ provides insight for the mean XPD that is obtained when averaging over the AAoA and EAoA distributions. The XPD averaged over the EAoA distribution only at each AAoA, $\alpha_R$, is depicted in Figure 10. For AAoAs equal to 180°, 0° and 360°, which represent vertical CoP planes, the XPD goes infinity, meaning that there are no cross-polarization components at those angles. This makes sense given the geometry in Figure 4. The remarkable thing is that each XPD curve has a minimum point when the AAoA lays in the range 155° – 170°. The XPD at this minimum point is below 0 dB, which means that the power of the cross-polarization component is stronger than that of the copolarization component.

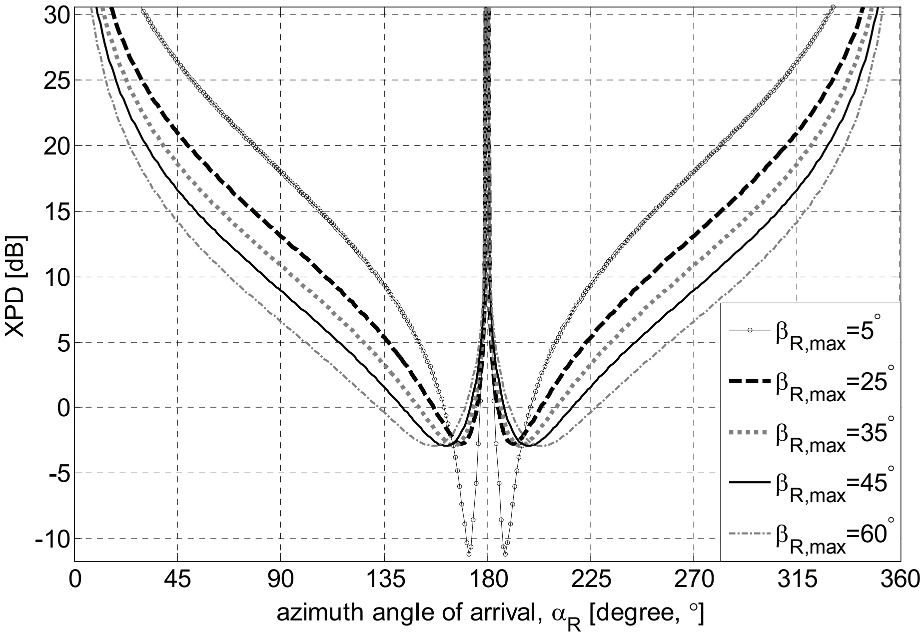

**Figure 10:** $\overline{XPD}^{F2M}$ curves for varying $\alpha_R$ and $\beta_{Max,R}$.

A larger maximum EAoA will result in a smaller mean XPD, since the XPD is below 0 dB over a larger AAoA range. If XPD is averaged over AAoA distribution with $\mu_R = 180°$ and $k_R$ varying from 0 to 9, it can be recognized that as $k_R$ increases the mean XPD decreases, since the impact of the small XPDs for AAoAs around the minimum point will dominate the high XPDs for AAoAs that are far from the minimum point. Furthermore, small changes in the AAoA distribution near 180° (Tx–Rx boresight) created by site-specific local scattering will cause significant changes in the mean XPD, which explains the high variance of the empirical XPD values observed in [1, 12].

### 3.3.3 Comparison of Analytical and Empirical Results-2: Urban Area in Tokyo

The proposed geometrical model can also explain the empirically derived XPD results reported in [7]. Figures 11 and 12 plot theoretical XPD results for the XPD measurement scenarios corresponding to Figures 9 and 10 in [7], respectively. The $x$-axis variable, $\phi_{(street,TxRx)}$ is the angle between the street line and the Tx–Rx bore sight line. As shown in Figure 7 of [7], at least in the location where the XPD sounding campaign was performed for the scenario in Figure 9 of [7], the plane waves received from the north direction of the street corridor were stronger than those received from any other direction including the Tx–Rx bore sight. For this reason, the mean AAoA, $\mu_R$, in our geometric model was set to point to the north direction of the street corridor at the Rx. In our geometric model, this mean AAoA is $\pi - \phi_{(street,TxRx)}$, since the direction of the Tx–Rx bore sight at the Rx is always equal to $\pi$ in the coordinates for the reference model shown in Figure 4. In a similar manner, for the scenario in Figure 10 of [7], $\mu_R = \pi + \phi_{(street,TxRx)}$, since the plane waves from the west direction of the street corridor were stronger and more intensely distributed than those received from other directions. In addition, the maximum EAoA, $\beta_R$ was set to be 45° and 30° in Figures 11 and 12, respectively, unless otherwise stated in the legend.

The XPD corresponding to each angle of arrival was computed, and the "effective XPD" was defined as weighted average of all such XPDs, where the weighting factor is the ratio of the received power measured at the corresponding angle of arrival to the sum of the received powers measured at all angles of arrival in [7]. In contrast, this proposal defines the mean XPD as the ratio of the averaged power of the copolarization components to that of the cross-polarization components, following the conventional definition of XPD. These two definitions of XPDs were computed from the proposed theoretical model, and the analytical "effective XPD" is compared with that obtained from the measurement data and reported in Figures 9 of [7]. Both definitions of the XPD obtained from the analysis, as well as the empirical "effective XPD" reported in [7] are plotted in Figure 11. The notations, $\mathrm{XPRC}^{\mathrm{MS}}$ and XPD represent the "effective XPD" defined in [7] and mean XPD defined in this proposal, respectively, and XPRC represents the cross-polar ratio centroid in [7]. Further, $\mathrm{XPRC}_{\mathrm{h}}^{\mathrm{MS}}$ and $\mathrm{XPRC}_{\mathrm{v}}^{\mathrm{MS}}$ represent the "effective XPD" measured with horizontally and vertically polarized Tx antennas, respectively. Finally, the labels in the legend of Figure 11 having the form $k_{R,1}, k_{R,2}$ are referring to the mixture-distribution of the AAoA,

$$\begin{aligned} p_r(\alpha_R) &= q_1\, p_{r,1}(\alpha_R) + (1-q_1)\, p_{r,2}(\alpha_R) \\ &= q_1 \frac{\exp[k_{R,1}\ \cos(\alpha_R - \mu_{R,1})]}{2\pi I_0(k_{R,1})} + (1-q_1)\, \frac{\exp[k_{R,2}\ \cos(\alpha_R - \mu_{R,2})]}{2\pi I_0(k_{R,2})}, \end{aligned} \quad (73)$$

where $0 \leq q_1 \leq 1$. The composite-AAoA distribution in (73) is a generalized version of the one introduced in [52]. This mixed-AAoA distribution was shown to provide a better fit in terms of minimum mean-square error (MMSE) in [52], and it also results in closer agreement with the empirical data in [7] than the non-mixed-AAoA distribution in (34).

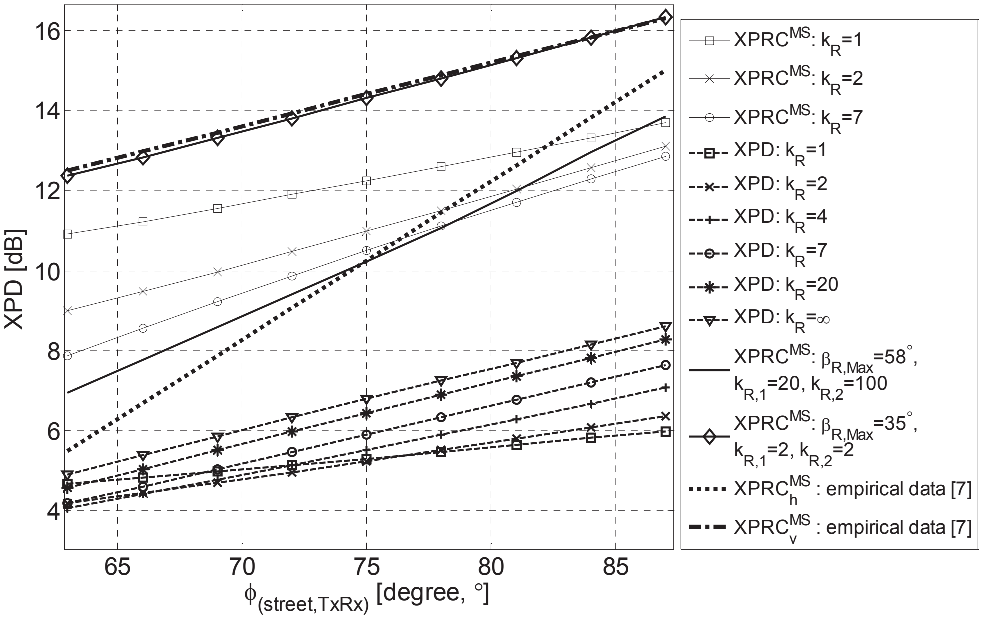

**Figure 11:** $\overline{XPD}^{F2M}$ and the "effective XPD" curves in the route Rx6 to Rx19 in Figure 9 of [7].

The "effective XPD", XPRC$^{\mathrm{MS}}$, obtained from the proposed theoretical model closely agrees with the empirically-obtained values in [7]. The empirical-XPD curve, XPRC$_{\mathrm{v}}^{\mathrm{MS}}$ in Figure 11 is in close agreement with the XPRC$^{\mathrm{MS}}$ curve when $k_{R,1} =$

$k_{R,2} = 2$, $\mu_{R,1} = \pi - \phi_{(street,TxRx)}$, $\mu_{R,2} = \big(\pi - \phi_{(street,TxRx)}\big) - \pi/2$, and $q_1 = 0.9$ in (73), and $\beta_{R,max} = 35°$. The other empirical XPD curve in Figure 11, $\mathrm{XPRC}_{\mathrm{h}}^{\mathrm{MS}}$ is also in good agreement with the $\mathrm{XPRC}^{\mathrm{MS}}$ curve when $k_{R,1} = 20$, $k_{R,2} = 100$, $\mu_{R,1} = \pi - \phi_{(street,TxRx)}$, $\mu_{R,2} = \big(\pi - \phi_{(street,TxRx)}\big) - \pi/2$, and $q_1 = 0.9$ in (73); and $\beta_{R,max} = 35°$. It is worth mentioning that the second mean-AAoA, $\mu_{R,2}$, corresponds to the direction of the east-side wall of the house or building at the Rx, which can cause strong SBR plane waves as measured in [7]. Note that it is usual for the second component of the mixed-AAoA distribution, which is non-isotropic in this case, to be concentrated along one direction in the two-dimensional (2-D) model of [52], and this principle was extended to the 3-D model in this proposal.

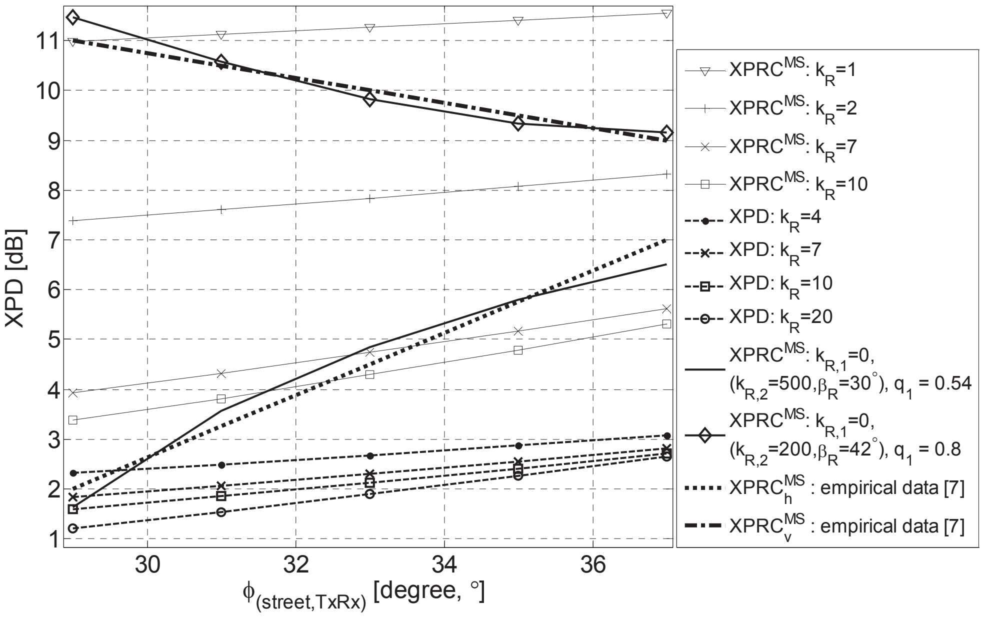

**Figure 12:** $\overline{XPD}^{F2M}$ and the "effective XPD" curves in the route Rx19 to Rx27 in Figure 10 of [7].

In Figure 12, the empirical curves $\mathrm{XPRC}_{\mathrm{v}}^{\mathrm{MS}}$ and $\mathrm{XPRC}_{\mathrm{h}}^{\mathrm{MS}}$ also agree closely with the theoretical results. The curve for $\mathrm{XPRC}_{\mathrm{v}}^{\mathrm{MS}}$ in Figure 12 is in close agreement with the $\mathrm{XPRC}^{\mathrm{MS}}$ curve when $k_{R,1} = 0$, $k_{R,2} = 200$, $\mu_{R,2} = \pi + \phi_{(street,TxRx)}$, and $q_1 = 0.8$ in (73). The parameter $\mu_{R,1}$ has no effect on the AAoA distribution in this case, since $k_{R,1} = 0$ which means that $p_{r,1}(\alpha_R) = 1/(2\pi)$ regardless of the value of $\mu_{R,1}$. The second component $p_{r,2}(\alpha_R)$ is substantially concentrated around the mean AAoA $\mu_{R,2} = \pi + \phi_{(street,TxRx)}$. The EAoA distribution associated with the second component, $p_{r,2}(\beta_R)$, is assumed to be $p_{r,2}(\beta_R) = \delta(\beta_R - 42°)$ which means that the plane waves with the second component only arrive with an EAoA equal to 42°. Finally, $\mathrm{XPRC}_{\mathrm{h}}^{\mathrm{MS}}$ in Figure 12 is also in close agreement with the $\mathrm{XPRC}^{\mathrm{MS}}$ curve when $k_{R,1} = 0$, $k_{R,2} = 500$, $\mu_{R,2} = \pi + \phi_{(street,TxRx)}$ and $q_1 = 0.54$ in (73). Once again $\mu_{R,1}$ is arbitrary in this case, since $k_{R,1} = 0$. Also, in this case $p_{r,2}(\beta_R) = \delta(\beta_R - 30°)$.

## *3.4 Analytical Results of the Reference Model*

This section presents some further analytical XPD results based on the mathematical reference models in Sections 3.1 and 3.2.

### 3.4.1 Default Parameter Setting

We assume a 2.48 GHz carrier frequency, and $h_T = h_R = 3$ m in Figures 6 and 7 for M2M channels. The reference model parameters for M2M channels in (34) – (35) and (70) – (71) are set to $\mu_R = 180°$, $\beta_{R,Max} = 15°$, $\mu_T = 0°$, $\beta_{T,Max} = 15°$, $\eta_{SBT} = 0.15$, $\eta_{SBR} = 0.35$, $\eta_{DB} = 0.5$, and $R_r = R_t = 10$ m, unless otherwise stated. The parameters $k_R$ and $k_T$ will be set to different values for each mean XPD curve. The default parameter values for M2M channels mentioned above are intended to show results with physically meaningful parameters, and also to demonstrate the reciprocity property between the SBT and SBR propagation modes as will be seen later in this section. Figures 14 and 15 show analytical XPD results for M2M channels, while Figures 13 and 16 show analytical XPD results for F2M channels. The reference model parameters in Figures 13 and 16 are set to be same as those in Figures 8 and 10, respectively, unless otherwise stated.

### 3.4.2 Further Analytical Results for the XPD and Rx Polarization Angle

Considering a F2M channel, Figure 13 portrays the mean XPD and the corresponding mean Rx polarization angle with respect to the vertically and horizontally polarized Rx antennas for different Tx polarization angles at a fixed Tx–Rx distance, $D = 1$ km. The Tx polarization angle in Figure 13 is defined as the angle between the Tx polarization vector and the horizontal polarization vector. That is, 0° and 90° polarization angles on the perpendicular plane of the wave correspond to horizontal and vertical polarization vectors, respectively. Further, the mean Rx polarization angle in Figure 13 is defined as $\arctan\left(\sqrt{\overline{XPD_{V/H}}}\right)$. The two functions in Figure 13 strongly depend on the polarization angle that the Tx antenna utilizes. Notice that $\overline{XPD_{V/H}}$ is the largest when the Tx polarization angle is not 90°, but 76° at $D = 1$ km. Of course the optimal Tx polarization angle will depend on the particular reference model parameters being used, especially the parameters used in the A/EAoA distributions.

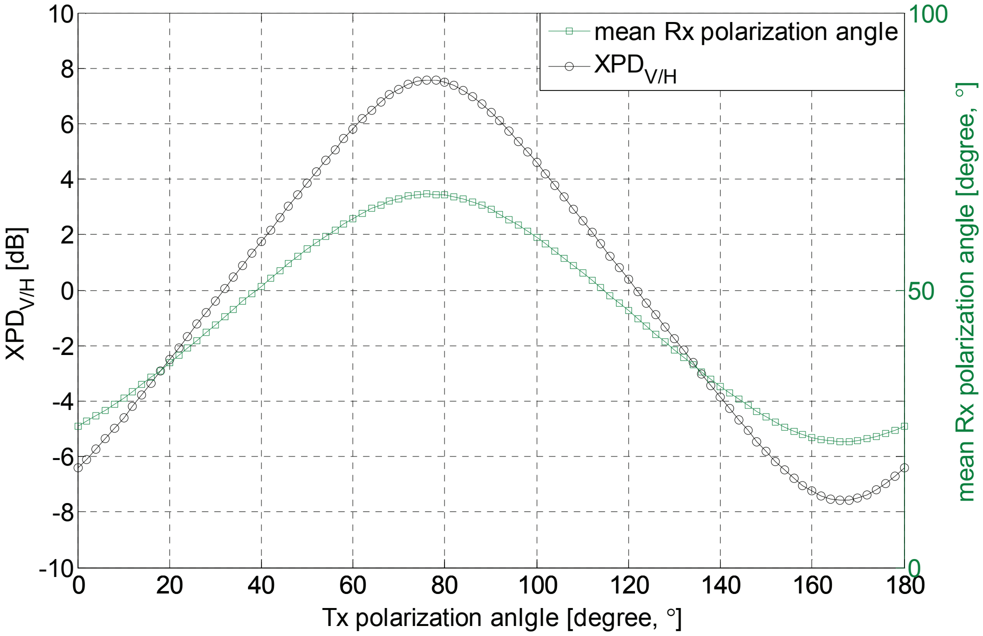

**Figure 13:** Mean polarization angle and $\overline{XPD}_{V/H}^{F2M}$ at the Rx, according to the polarization angle of the Tx: $D = 1$ km, $k_R = 0$.

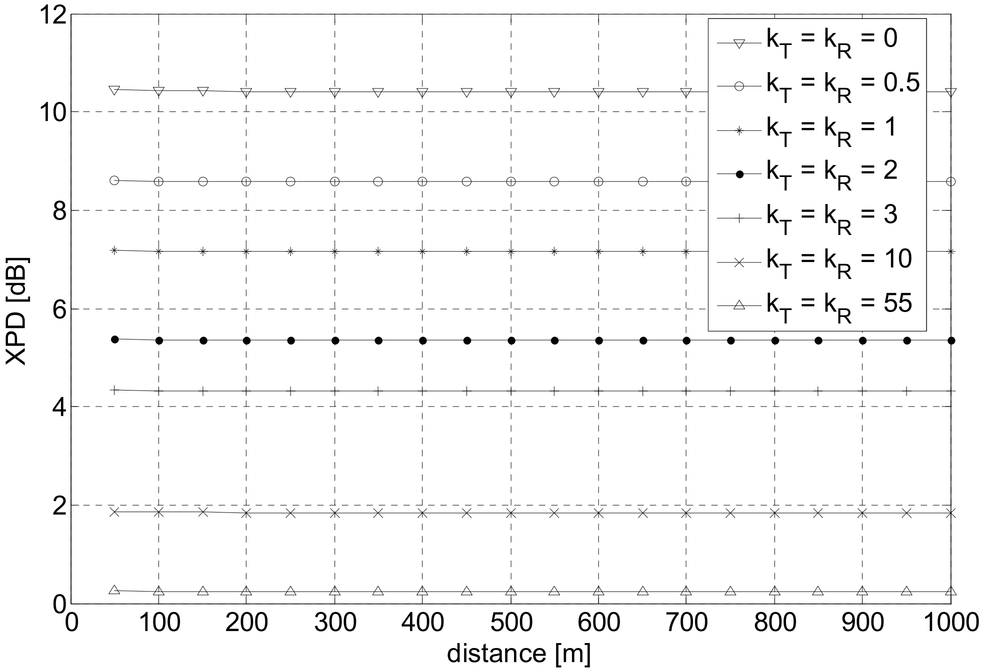

**Figure 14:** $\overline{XPD}^{M2M}$ curves for the SBT/SBR propagation with a variety of $k_R = k_T$ with Tx-Rx distance in the range 50 m to 1 km.

Considering a M2M channel, Figure 14 portrays the analytical mean XPD curves for the SBT or SBR propagation modes for various $k_R$ or $k_T$ ranging from 0 to 55. Each curve can be applied to both SBT and SBR propagation modes with the stated parameter settings, since there is a reciprocity between the SBT and SBR propagation modes. The same tendency as in Figure 8 is exhibited, except that the XPD curve decreases from 10.5 dB to 0 dB even when $k_R$ or $k_T$ increases up to 55. However, the XPD goes below 2 dB as $k_R$ or $k_T$ increases to 10 and, thus, channel depolarization can be significant not only in F2M channels but M2M channels as well, particularly when $k_R$ and $k_T$ lay' in the range 3 to 55 in Figure 14. It is notable that the channel depolarization for M2M channels in Figure 14 is less significant than that observed for F2M channels in Figure 8, for $k_R$ or $k_T$ in the range 0 to 2, corresponding to an isotropic or near-isotropic scattering environment. When $k_R$ or $k_T$ is in the range 55 to 700, the same tendency as in Figure 9 is observed except that XPD curve increases from 0.25 dB to 3.75 dB, and it is omitted owing to the complexity of the figure. Similar to Figures 8 and 9, the XPD is not directly dependent on $D$, and can show high variance depending on the values of $k_R$ and $k_T$ even at the same $D$ as depicted in Figure 14.

The XPD of M2M channels is derived by computing the ratio of the power of copolarization components in the SBT, SBR, DB and LoS propagation modes, if they exist, to that of the cross-polarization components in those propagation modes. As shown in Section 3.2, the contribution of SBT, SBR and DB propagation modes in the total received power can be adjusted via the weights, $\eta_{SBT}$, $\eta_{SBR}$ and $\eta_{DB}$. Assuming NLoS channel conditions ($K = 0$), Figure 15 shows that the final XPD curve that includes a weighted XPD contribution from each NLoS propagation mode is just a linear combination of the XPD curves of the three NLoS propagation modes.

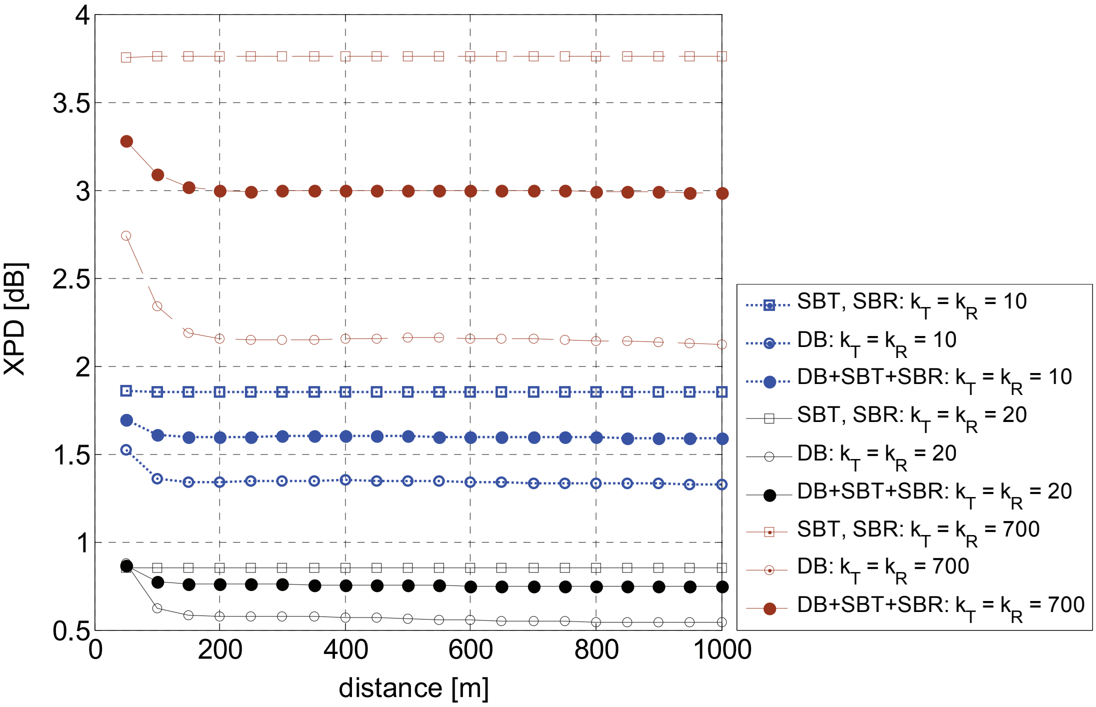

**Figure 15:** $\overline{XPD}^{M2M}$ curves for SBT, SBR and DB propagation modes and their combination.

Figure 15 includes two practical scenarios, $k_R = k_T = 10$ and $k_R = k_T = 20$, and a extreme scenario, $k_R = k_T = 700$. The XPD curve for the DB propagation mode tends to have values that are one-half to two-thirds of the values in the XPD curve for the SBT or SBR propagation modes with same $k_R$ and $k_T$. If $k_R = k_T \approx 0$, the XPD of SBT or SBR propagation mode is 10.5 dB in Figure 14 and, thus, the XPD of the DB propagation mode and the total XPD can be, respectively 5.5 and 8.0 dB. Hence, the total XPD can exhibit a substantial variation depending on the weights $\eta_{SBT}$, $\eta_{SBR}$ and $\eta_{DB}$. Further, if $k_R \neq k_T$ and the gap between the XPD values for the SBT/SBR and DB propagation modes is large, then the total XPD can exhibit higher variation than the aforementioned scenario. In conclusion, it is recognized that the total XPD can vary greatly depending on the site specific local scattering environments around the Tx and Rx as reflected by the weights $\eta_{SBT}$, $\eta_{SBR}$ and $\eta_{DB}$.

## *3.5 Explanation of Peculiarities in Empirical XPD Results*

There are several characteristics of the empirical XPD measurements in [7] that cannot be easily explained. For example, the empirical curves for $\mathrm{XPRC}_{\mathrm{v}}^{\mathrm{MS}}$ and $\mathrm{XPRC}_{\mathrm{h}}^{\mathrm{MS}}$ in Figure 12 show tendencies that are opposite to each other, as $\phi_{(street,TxRx)}$ increases from 29° to 37°. Also, the XPD at a certain locations is remarkably high, such as 40 dB. However, there is no explanation as to why the observed XPD behaves in this manner. Determining the individual XPD of each arriving plane wave is helpful for understanding such scattering environments.

Figure 16 depicts the XPD of a plane wave that has a fixed AAoA and EAoA in F2M fading channels. Figure 10 is similar, but plots the XPD averaged over the EAoA distribution for a single AAoA. In Figure 16, the bold gray line with the notation, $\beta_{Max,R} = 45°$ is the XPD curve averaged over the EAoA distribution with $\beta_{Max,R} = 45°$ to compare with the XPD curve for a particular EAoA. The portion of each curve below 0 dB exhibits significant variation of XPD as compared to the curves in Figure 10. This means that scatterers located at certain locations can produce particularly strong cross-polarization components. Note that the XPD averaged over the EAoA distribution such as the aforementioned bold gray line in Figure 10 does not exhibit a sharp drop in the XPD as observed in Figure 16, since the AAoA that yields an extreme drop in XPD depends on the particular EAoA.

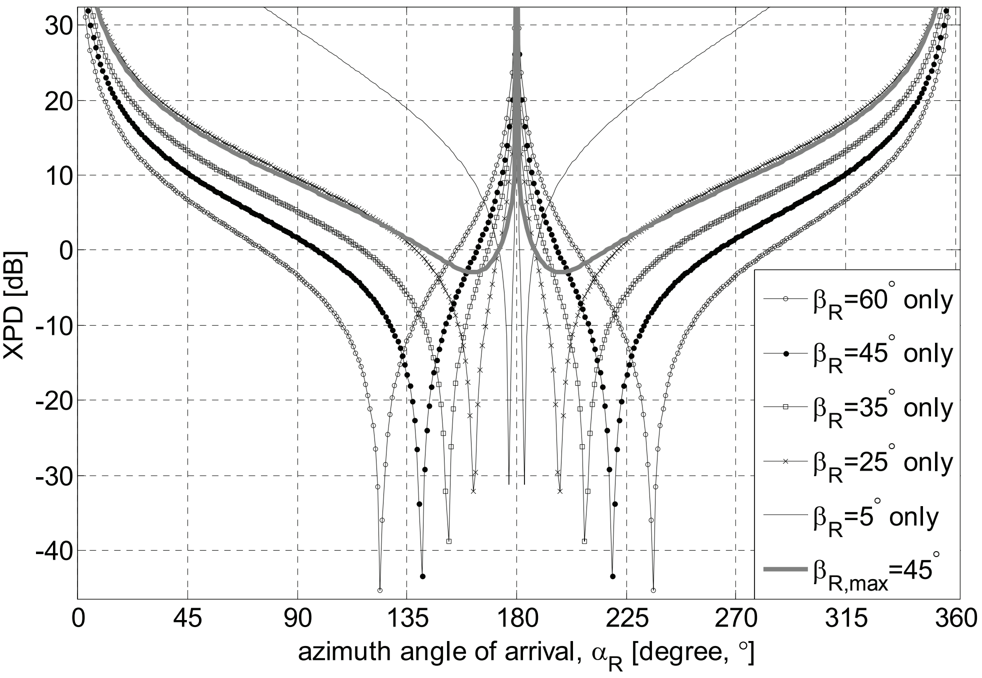

**Figure 16:** $\overline{XPD}^{F2M}$ curves of the SBR propagation mode for varying $\alpha_R$ and $\beta_R$.

If the plane waves in F2M channels arrive via a narrow EAoA range, some peculiar phenomena can occur. For the aforementioned scenario in Figure 12, $\mu_{R,2} = \pi + \phi_{(street,TxRx)}$ is varied from 209° to 217° as $\phi_{(street,TxRx)}$ increases from 29° to 37°. When $\beta_R = 45°$ in Figure 16, the minimum point at $\alpha_R = 219°$ is at the right side of the whole range of $\mu_{R,2}$, 209° to 217°, and the XPD decreases as $\phi_{(street,TxRx)}$ increases from 29° to 37°. This is the case for $\mathrm{XPRC}_{\mathrm{v}}^{\mathrm{MS}}$ in Figure 12. However, when $\beta_R = 25°$, the minimum point at $\alpha_R = 198°$ is at the left side of the whole range of $\mu_{R,2}$, 209° to 217°, and the the XPD increases as $\phi_{(street,TxRx)}$ increases from 29° to 37°. This is the case for $\mathrm{XPRC}_{\mathrm{h}}^{\mathrm{MS}}$ in Figure 12. Finally, a large XPD value of 40 dB is observed in [7] when a metallic garage door is located in the direction of $\alpha_R = 0°$ to 20°. Figure 16 shows that the XPD in this range of $\alpha_R$ is particularly high, which explains why this very large XPD value is observed.

Finally, we note that the XPD will vary in time with the same time rate of variation of log-normal shadowing. Under the assumption the that channel is locally wide-sense stationary, the locally observed XPD will not depend on the speed and moving direction of the Tx and Rx through the parameters $v_R$, $v_T$, $\gamma_R$ and $\gamma_T$. This can be readily seen from (63) – (66), where the ensemble averaging over the random phases $\{\phi_n^{\text{case}}\}$ for case $\in \{SBT, SBT, DB\}$ removes any dependency of the XPD on the exponential terms in the complex channel impulse response. However, the XPD can vary substantially with the Tx–Rx distance due to site specific changes in the local scattering environment around the Tx and Rx, i.e., the channel is *locally* wide-sense stationary. Hence, $v_R$, $v_T$, $\gamma_R$ and $\gamma_T$ will affect the time rate of variation of XPD in a manner similar to the way they affect the time rate of variation of log-normal shadowing.

## *3.6 Summary*

This chapter has proposed 3-D geometry-based mathematical reference models for XPD in F2M and M2M narrow-band fading channels. The models are validated based on measurement data in several aspects. To the best of our knowledge, the described geometrical theory for channel depolarization and the resulting XPD modeling methodology is the first to mathematically describe the mechanisms of channel depolarization and XPD. The proposed theory and methodology showed that the XPD depends greatly on the distribution of scatterers as represented by the pdfs of the A/EAoAs and A/EAoDs, while it does not much depend on the distance between the Tx and Rx. The analytical XPD results obtained with our reference model are in good agreement with empirically observed XPD values. The reference models can be used to study more generalized or specialized propagation scenarios, and to facilitate the practical exploitation of channel depolarization and XPD.

Finally, the geometrical theory of channel depolarization introduced in this chapter can be applied to other geometry-based channel models as well. However, we note that any such geometric channel model used to study channel depolarization must be a 3-D model. Any 2-D propagation model will have CoP planes that lay only in the $x-y$ plane. Hence, the polarization angles with any 2-D propagation model are always $90^o$ and no channel depolarization will occur.

# CHAPTER IV

# GEOMETRICALLY-BASED STATISTICAL MODEL FOR POLARIZED BODY-AREA NETWORK CHANNELS

A novel geometry-based propagation model for wide-band polarized body area network (BAN) channels is proposed by considering three wireless radio propagation modes: cylindrical-surface-scattered (CSS), body-scattered (BS), and ground-scattered (GS) propagation modes.[1] A conservation-of-polarization (CoP) plane methodology is applied to derive the channel polarization functions for the CSS and GS propagation modes, while those for the BS component are obtained by using a geometrical theory of diffraction. The statistical characteristics, such as the cross-polarization discrimination (XPD) and time-frequency correlation function (TF-CF) are derived for the model. Comparisons of the XPD and TF-CF obtained from the proposed model, with appropriate parameters, and those obtained from measurements are in excellent agreement with each other. The GS propagation mode is shown to be the most dominant component among aforementioned three propagation modes, and the azimuth angle of arrival has a significant effect on the XPD in the GS propagation mode.

This chapter proposes a theoretical model for the polarized BAN channel, characterized by either isotropic or non-isotropic azimuthal scattering and with either non-line-of-sight (NLoS) or line-of-sight (LoS) conditions between a Tx and Rx that

---

[1] This work in Chapter 4 was supported by the Space and Naval Warfare Systems Center Pacific and the Strategic Technology Office (STO) of DARPA under the direction of Dr. Bruce Fette. Distribution Statement "A" (Approved for Public Release, Distribution Unlimited). The U.S. Government is authorized to reproduce and distribute reprints for Government purposes notwithstanding any copyright notation thereon. The views and conclusions contained in this document are those of the authors and should not be interpreted as representing the official policies, either expressed or implied, of the Space and Naval Warfare Systems Center Pacific, of DARPA, or the U.S. Government.

are both located on the body. The polarized BAN channel is considered to have four propagation modes; scattered waves from the surrounding surfaces above the ground, from the ground, from the body; and the LoS wave. Scattered waves from the surrounding surfaces and body are modeled by CSS and BS propagation models, respectively, and those from the ground are modeled by a GS propagation model. The LoS component is often blocked by the human body, particularly when the Rx is located on the back of the body, and the Tx is located on the arm or leg. The main contributions are summarized as follows: 1) a unique three-dimensional (3-D) geometry-based model for the polarized wireless BAN channel with three different propagation modes; CSS, BS and GS propagation modes; 2) a theoretical modeling of the creeping wave using diffraction theories; 3) empirical validation of the proposed polarized BAN channel model at 13 GHz; 4) Observation that the GS propagation mode is the most dominant propagation mode in the TF-CF characteristics at 13 GHz; 5) analytical characterization of polarized BAN channels based on the proposed BAN channel model.

## *4.1 CSS/BS Propagation Mode in BAN Channels*

This section introduces our geometrical model for the CSS and BS propagation modes in BAN channels, and derives the channel polarization functions utilizing the conservation-of-polarization (CoP) plane methodology introduced in [9].

### 4.1.1 Geometric Single-Cylinder Model for CSS Propagation

As shown in Figure 17, our model assumes that some scatterers are distributed on a cylindrical surface that surrounds both the Tx and Rx.[2] These scatterers result in CSS propagation in wireless BAN channels. Both the Tx and Rx are located on the body at a short horizontal distance from each other in the order of 0.5 m; therefore,

---

[2] Here the term "scatterer" refers to a plane boundary that is typically much larger than a wavelength.

they are assumed to be surrounded by the same cylinder the center of which is at the Rx antenna. This unique geometry of the Tx, Rx, and scatterers in the wireless BAN channel creates different polarization functions and characteristics from those of the F2M/M2M channel in our earlier work [9], although they may look similar at a glance.

Cylindrical models have been suggested before for F2M channels [21,50] and M2M channels [9]. However, a cylindrical model has not been used previously for BAN polarized channels, where both the Tx and Rx are inside a single cylinder. The cylindrical scattering surface is characterized by its radius $R_r$, and the ray incident on the Rx antenna from each scatterer on the cylinder has an associated azimuth angle of arrival (AAoA), $\alpha_R$, and elevation angle of arrival (EAoA), $\beta_R$. Finally, $D$ is the horizontal distance between the Tx and Rx.

### 4.1.2 CSS Polarization Functions

The phenomenon of the BAN channel depolarization between a Tx and an Rx can be observed by the NLoS waves that arrive at the Rx via scattering objects. Figure 17 depicts a scenario where a vertically polarized wave emitted from the Tx can result in a horizontally polarized wave component being received at the Rx. Hence, channel depolarization occurs.

The conservation-of-polarization plane is defined as the Tx-scatterer-Rx plane [9]. The polarization angle associated with a CoP plane, denoted by $\theta_V$ in Figure 17, is defined as the angle between $\underline{V}$ and the line that includes the projection of $\underline{V}$ onto the CoP plane. Due to the conservation of polarization assumption, the angle between $\underline{V}$' and the line that includes the projection of $\underline{V}$' onto the same CoP plane in Figure 17 is equal to $\pi - \theta_V$ [9]. In the same manner as the CoP plane method in [9], the amplitude of the received wave at a vertically (horizontally) polarized Rx antenna via

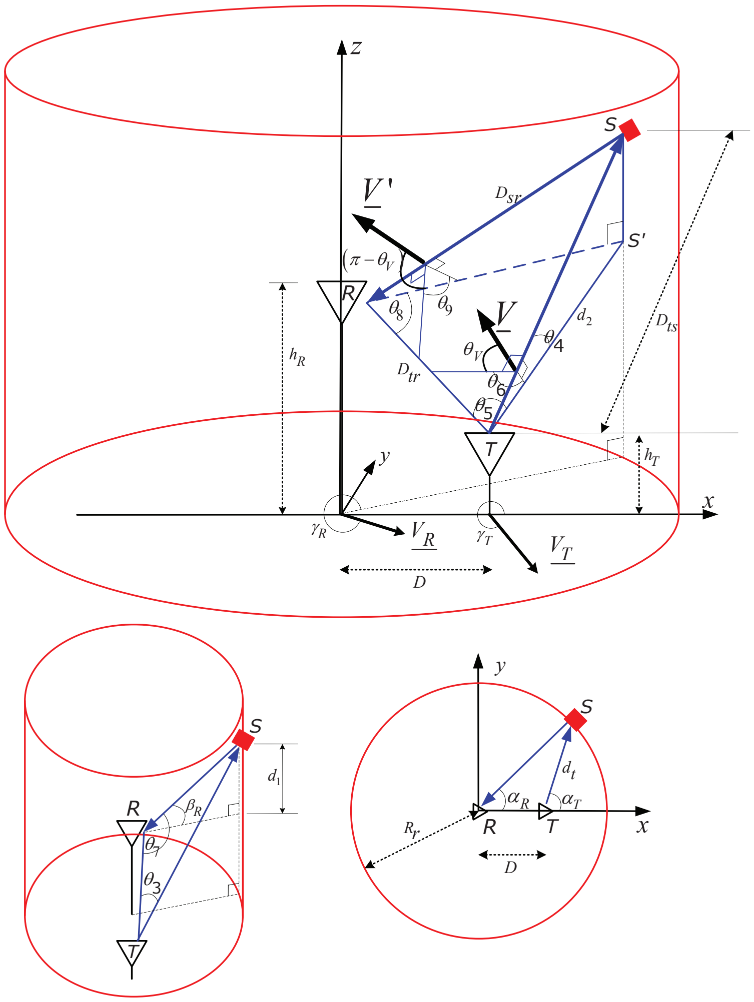

**Figure 17:** 3-D cylindrical surface scattering (CSS) model for BAN channels.

a single scatterer, $A_{VV}$ ($A_{HV}$) can be expressed as

$$\begin{bmatrix} A_{VV}^{CSS} \\ A_{HV}^{CSS} \end{bmatrix} = A_V^{CSS} \begin{bmatrix} f_{VV}^{CSS}(D, D_{ts}, D_{sr}, R_r, \alpha_R, \beta_R) \\ f_{HV}^{CSS}(D, D_{ts}, D_{sr}, R_r, \alpha_R, \beta_R) \end{bmatrix}, \tag{74}$$

where $A_V^{CSS}$ is the amplitude of $\underline{V}$' at the Rx. From the geometry in Figure 17, the distances are,

$$d_t = \sqrt{(D - R_r \cos\alpha_R)^2 + (R_r \sin\alpha_R)^2}, \tag{75}$$

$$D_{ts} = \sqrt{{d_t}^2 + (\Delta_h + R_r \tan\beta_R)^2}, \tag{76}$$

$$D_{sr} = R_r/\cos\beta_R, \;\; d_1 = R_r \tan\beta_R, \tag{77}$$

$$D_{tr} = \sqrt{D^2 + {\Delta_h}^2}, \;\; d_2 = \sqrt{{d_t}^2 + {\Delta_h}^2}, \tag{78}$$

where $\Delta_h = (h_T - h_R)$. Based on (75) – (78) and the law of cosines, the angles in Figure 17 can be written as

$$\begin{aligned}
\cos\theta_3 &= \frac{{D_{ts}}^2 + {D_{tr}}^2 - {D_{sr}}^2}{2D_{ts}D_{tr}} \\
&= \frac{a_1 - a_2 + a_3}{\sqrt{(a_1 - 2a_2 + 2a_3 + 1/\cos^2\beta_R)\, a_1}}, && (79)\\
\cos\theta_4 &= \frac{{D_{ts}}^2 + {d_2}^2 - {d_1}^2}{2D_{ts}d_2} \\
&= \frac{(1 + a_1 - 2a_2 + a_3)}{\sqrt{(a_1 - 2a_2 + 2a_3 + 1/\cos^2\beta_R)\,(1 + a_1 - 2a_2)}}, && (80)\\
\cos\theta_5 &= \frac{{d_2}^2 + {D_{tr}}^2 - {R_r}^2}{2d_2D_{tr}} = \frac{a_1 - a_2}{\sqrt{(1 + a_1 - 2a_2)\, a_1}}, && (81)\\
\cos\theta_6 &= \frac{\cos\theta_5 - \cos\theta_3\cos\theta_4}{\sqrt{(1 - \cos^2\theta_3)\,(1 - \cos^2\theta_4)}}, \quad \theta_V = \pi - \theta_6, && (82)\\
\cos\theta_7 &= \frac{{D_{sr}}^2 + {D_{tr}}^2 - {D_{ts}}^2}{2D_{sr}D_{tr}} = \frac{a_2 - a_3}{(1/\cos\beta_R)\sqrt{a_1}}, && (83)\\
\cos\theta_8 &= \frac{{D_{tr}}^2 + {R_r}^2 - {d_2}^2}{2D_{tr}R_r} = \frac{a_2}{\sqrt{a_1}}, \\
\cos\theta_9 &= \frac{\cos\theta_8 - \cos\theta_7\cos\beta_R}{\sqrt{(1 - \cos^2\theta_7)\,(1 - \cos^2\beta_R)}}, && (84)\\
a_1 &= \left(\frac{D}{R_r}\right)^2 + \left(\frac{\Delta_h}{R_r}\right)^2, \quad a_2 = \frac{D}{R_r}\cos\alpha_R\ , \quad a_3 = \frac{\Delta_h}{R_r}\tan\beta_R, && (85)
\end{aligned}$$

The angles $\cos\theta_6$ and $\cos\theta_9$ in (82) and (85), respectively, can be used to derive the channel polarization functions in (74); $f_{VV}^{CSS}$ and $f_{HV}^{CSS}$ for a vertically polarized Tx antenna, and $f_{HH}^{CSS}$ and $f_{VH}^{CSS}$ for a horizontally polarized Tx antenna. From the geometry in Figure 17, the amplitudes of the vertical and horizontal polarization components that are received from a vertically polarized transmitted wave are, respectively,

$$\begin{aligned}
A_{VV}^{CSS} &= A_V^{CSS} \left|\cos\left(\theta_9 + (\pi - \theta_V) - \pi\right)\right| && (86)\\
&= A_V^{CSS} \left|\cos\theta_6\cos\theta_9 - \sqrt{1 - \cos^2\theta_6}\sqrt{1 - \cos^2\theta_9}\right| \ , \\
A_{HV}^{CSS} &= A_V^{CSS} \left|\sin\left(\theta_9 + (\pi - \theta_V) - \pi\right)\right| && (87)\\
&= A_V^{CSS} \left|\cos\theta_6\sqrt{1 - \cos^2\theta_9} + \cos\theta_9\sqrt{1 - \cos^2\theta_6}\right| \ ,
\end{aligned}$$

where $\cos\theta_6$ and $\cos\theta_9$ in (86) and (87) are functions of $D$, $R_r$, $\alpha_R$, $\beta_R$ as is evident from (79) – (85). Comparing (86) and (87) with (74), the channel polarization functions $f_{VV}^{CSS}$ and $f_{HV}^{CSS}$ can be written as:

$$\begin{aligned}
& f_{VV}^{CSS}(D, D_{ts}, D_{sr}, R_r, \alpha_R, \beta_R) \\
& \equiv f_{VV}^{CSS}(D, R_r, \alpha_R, \beta_R) \\
& = \left| \cos\theta_6 \cos\theta_9 - \sqrt{1-\cos^2\theta_6}\sqrt{1-\cos^2\theta_9} \right| \ , \qquad (88) \\
& f_{HV}^{CSS}(D, D_{ts}, D_{sr}, R_r, \alpha_R, \beta_R) \\
& \equiv f_{HV}^{CSS}(D, R_r, \alpha_R, \beta_R) \\
& = \left| \cos\theta_6 \sqrt{1-\cos^2\theta_9} + \cos\theta_9 \sqrt{1-\cos^2\theta_6} \right| \ . \qquad (89)
\end{aligned}$$

In a similar fashion, the channel polarization functions $f_{HH}^{CSS}$ and $f_{VH}^{CSS}$ can be written as:

$$\begin{aligned}
& f_{VH}^{CSS}(D, D_{ts}, D_{sr}, R_r, \alpha_R, \beta_R) \\
& \equiv f_{VH}(D, R_r, \alpha_R, \beta_R) \\
& = \left| \cos\theta_6 \sqrt{1-\cos^2\theta_9} + \cos\theta_9 \sqrt{1-\cos^2\theta_6} \right| \ , \qquad (90) \\
& f_{HH}^{CSS}(D, D_{ts}, D_{sr}, R_r, \alpha_R, \beta_R) \\
& \equiv f_{HH}(D, R_r, \alpha_R, \beta_R) \\
& = \left| \cos\theta_6 \cos\theta_9 - \sqrt{1-\cos^2\theta_6}\sqrt{1-\cos^2\theta_9} \right| \ . \qquad (91)
\end{aligned}$$

Although the methodology in [9] is utilized to obtain polarization functions of the wireless BAN channel, and the polarization functions in (88) – (91) have same form as those in [9] with respect to $\cos\theta_6$ and $\cos\theta_9$, the parameters $a_1$, $a_2$, and $a_3$ upon which $\cos\theta_6$ and $\cos\theta_9$ depend for BAN channels are totally different from the parameters $a_1$, $a_2$, $a_3$, $a_4$, and $a_5$ upon which $\cos\theta_6$ and $\cos\theta_9$ depend for F2M/M2M channels in [9]. Hence, the polarization functions in (88) – (91) for BAN channels are completely different from those of F2M/M2M channels as well. Similar to F2M/M2M channels, a symmetry exists in the co- and cross-polarization functions such that

$$f_{VV}^{CSS} = f_{HH}^{CSS}, \ f_{HV}^{CSS} = f_{VH}^{CSS} \ . \tag{92}$$

### 4.1.3 Geometric Model for BS Propagation

The BS propagation mode occurs via diffracted waves on the human body otherwise known as creeping waves. Here, the geometrical theory of diffraction introduced in [54] and its multipolarization version in [55] along with other relevant literature such as [56, 57] are utilized to represent creeping waves in wireless BAN. The CoP plane, $T$-$S$-$R$ in Figure 17 along with the semi-infinite diffraction plane and equivalent reflection plane are depicted in Figure 18. The CoP plane corresponds to the sheet of the paper, while the diffraction/reflection plane is perpendicular to the sheet of the paper. The conventional semi-infinite diffraction plane, or so called knife edge, is assumed [57], and the diffraction points are assumed to be distributed on the cylindrical surface of the aforementioned BS propagation model with physically reasonable modeling parameters as will be discussed in Sect. 4.4. The series of diffracting obstacles, which each creeping wave confronts, can be replaced by a single equivalent diffracting obstacle as described in [56, 57], and we assume that the diffraction plane is normal to incident and diffracted waves according to the conventional manner [57]. Finally, the knife edge is assumed to equally divide the angle $\angle(T\text{-}S\text{-}R)$ as suggested in [55]. In this case, the BS propagation model can be utilized via replacing the knife edge with the equivalent reflection plane caused by the scatterer on the cylindrical surface as portrayed in Figure 18. Polarization functions of the creeping wave can be derived in the exactly same fashion as the CSS propagation model except that the parallel and perpendicular diffraction coefficients should be substituted for parallel and perpendicular reflection coefficients instead of the CoP plane assumption as described below.

In the diffraction of the wave that has the linear combination of parallel and

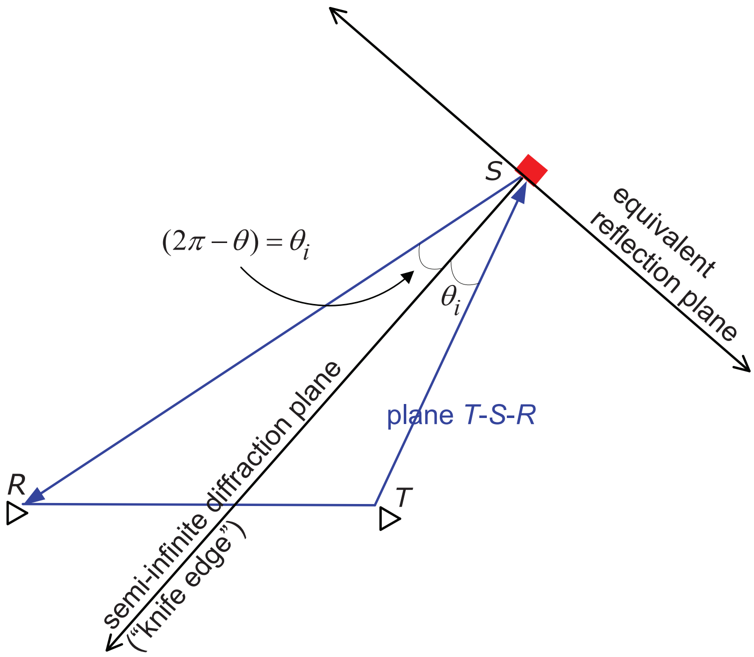

**Figure 18:** Semi-infinite diffraction plane and equivalent reflection plane in the BS propagation mode for creeping waves.

perpendicular polarization, the ideal condition such as the CoP plane in reflection cannot be assumed, since the parallel and perpendicular diffraction coefficients, $\zeta_{\|}$ and $\zeta_{\perp}$, respectively, cannot have the same form. However, in the scenario of Figure 18, they are expressed as [55]

$$\zeta_{\|}(\theta_i) = \frac{-\exp\left(-j\frac{\pi}{4}\right)}{2\sqrt{2\pi}}\left(-\sec\theta_i + 1\right), \quad \zeta_{\perp}(\theta_i) = \frac{-\exp\left(-j\frac{\pi}{4}\right)}{2\sqrt{2\pi}}\left(-\sec\theta_i - 1\right), \qquad (93)$$

where the incident angle, $\theta_i$, is conventionally defined as $\theta_i = \frac{1}{2}\angle(T\text{-}S\text{-}R)$, and finally, the vertical and horizontal polarization components of the diffracted wave can be obtained separately utilizing (93). Furthermore, parallel and perpendicular diffraction coefficients are functions of the geometrical modeling parameters, $D, R_r, \alpha_R$ and $\beta_R$ in Figure 17, since the following relations between $\theta_i$ and our geometrical channel modeling parameters are easily derived from (75) – (78).

$$
\begin{aligned}
\cos\theta_i &= \sqrt{\frac{1}{2}\left(\frac{{D_{ts}}^2+{D_{sr}}^2-{D_{tr}}^2}{2D_{ts}D_{sr}}+1\right)} \\
&= \sqrt{\frac{1}{2}\left(\frac{1/\cos\beta_R-(a_2-a_3)\cos\beta_R}{\sqrt{a_1-2a_2+2a_3+1/\cos^2\beta_R}}+1\right)} \quad , \qquad (94)
\end{aligned}
$$

where $a_i$ with $i = 1, 2, 3$ follows the definition in (85). From (93) – (94), it is obvious that parallel and perpendicular diffraction coefficients are the functions of channel modeling parameters $D, R_r, \alpha_R$, and $\beta_R$, i.e.,

$$\zeta_{\|}(\theta_i) = \zeta_{\|}(D, R_r, \alpha_R, \beta_R)\ ,\ \ \zeta_{\perp}(\theta_i) = \zeta_{\perp}(D, R_r, \alpha_R, \beta_R)\ . \qquad (95)$$

Note that these two functions vary differently with $D$, $R_r$, $\alpha_R$, and $\beta_R$ as described in (93) – (94). Finally, the geometrical diffraction coefficient ratio function, $R_\zeta(D, R_r, \alpha_R, \beta_R)$ is defined as follows:

$$R_\zeta = R_\zeta(D, R_r, \alpha_R, \beta_R) = \frac{\zeta_{\|}(D, R_r, \alpha_R, \beta_R)}{\zeta_{\perp}(D, R_r, \alpha_R, \beta_R)}\ . \qquad (96)$$

Transforming the polarization vector of the wave before the diffraction into that of the wave after the diffraction can be achieved by polarization vector decomposition along with geometrical diffraction coefficient functions. The polarization vector of a plane wave transmitted from the Tx, $\underline{V}$, is decomposed into its parallel and perpendicular polarization vector components, $\underline{V}_{\|}$ and $\underline{V}_{\perp}$, with respect to the CoP plane of the BS propagation model as

$$\underline{V} = \underline{V}_{\|} + \underline{V}_{\perp}. \qquad (97)$$

In the same manner, the polarization vector of the wave reflected from the scatterer, $\underline{V}'$, is expressed as

$$
\begin{aligned}
\underline{V}' &= \underline{V}'_{\|} + \underline{V}'_{\perp}, & (98)\\
\underline{V}'_{\|} &= \zeta_{\|}(D, R_r, \alpha_R, \beta_R)\ \underline{V}_{\|},\ \ \underline{V}'_{\perp} = \zeta_{\perp}(D, R_r, \alpha_R, \beta_R)\ \underline{V}_{\perp}. & (99)
\end{aligned}
$$

The amplitude of the vertical (horizontal) polarization component of $\underline{V}'$, $A_{VV}$ ($A_{HV}$) at the Rx is obtained by superimposing vertical (horizontal) polarization components of $\underline{V}'_{\|}$ and $\underline{V}'_{\perp}$. That is,

$$\begin{aligned}
A_{VV} &= A_V \frac{\left|\underline{V}'_{\|}\ \cos(\pi-\theta_9) + \underline{V}'_{\perp}\ \cos\left(\pi - \left(\theta_9 + \frac{\pi}{2}\right)\right)\right|}{|\underline{V}'|} \\
&= A_V \frac{\left|\zeta_{\|}\cos\theta_6\cos\theta_9 + \zeta_{\perp}\sin\theta_6\sin\theta_9\right|\,|\underline{V}|}{\sqrt{\left|{\zeta_{\|}}^2\cos^2\theta_6 + {\zeta_{\perp}}^2\sin^2\theta_6\right|}\ |\underline{V}|} \\
&= A_V\ \frac{\left|\zeta_{\|}\cos\theta_6\cos\theta_9 + \zeta_{\perp}\sin\theta_6\sin\theta_9\right|}{\sqrt{\left|{\zeta_{\|}}^2\cos^2\theta_6 + {\zeta_{\perp}}^2\sin^2\theta_6\right|}}\ , \qquad (100) \\
A_{HV} &= A_V \frac{\left|\underline{V}'_{\|}\ \sin(\pi-\theta_9) + \underline{V}'_{\perp}\ \sin\left(\pi - \left(\theta_9 + \frac{\pi}{2}\right)\right)\right|}{|\underline{V}'|} \\
&= A_V \frac{\left|\zeta_{\|}\cos\theta_6\sin\theta_9 - \zeta_{\perp}\sin\theta_6\cos\theta_9\right|}{\sqrt{\left|{\zeta_{\|}}^2\cos^2\theta_6 + {\zeta_{\perp}}^2\sin^2\theta_6\right|}}\ , \qquad (101)
\end{aligned}$$

where $A_V$ is the amplitude of $\underline{V}'$ at the Rx antenna, such that

$$A_{VV}{}^2 + A_{HV}{}^2 = A_V{}^2. \qquad (102)$$

$A_V{}^2$ can be adjusted according to any given power azimuth/elevation spectrum at the Rx.

Similar to the channel polarization functions of the CSS propagation mode, those of the BS propagation mode, which represents creeping waves, can be expressed as:

$$\begin{aligned}
f_{VV}(D, R_r, \alpha_R, \beta_R) &= \frac{|R_\zeta\cos\theta_6\cos\theta_9 + \sin\theta_6\sin\theta_9|}{\sqrt{\left|{R_\zeta}^2\cos^2\theta_6 + \sin^2\theta_6\right|}}\ , \qquad (103) \\
f_{HV}(D, R_r, \alpha_R, \beta_R) &= \frac{|R_\zeta\cos\theta_6\sin\theta_9 - \sin\theta_6\cos\theta_9|}{\sqrt{\left|{R_\zeta}^2\cos^2\theta_6 + \sin^2\theta_6\right|}}\ . \qquad (104)
\end{aligned}$$

Likewise, the other channel polarization functions for the horizontally polarized Tx antenna, $f_{VH}$ and $f_{HH}$ can be derived as:

$$\begin{aligned}
f_{VH}(D, R_r, \alpha_R, \beta_R) &= \frac{|R_\zeta\sin\theta_6\cos\theta_9 + \cos\theta_6\sin\theta_9|}{\sqrt{\left|{R_\zeta}^2\sin^2\theta_6 + \cos^2\theta_6\right|}}\ , \qquad (105) \\
f_{HH}(D, R_r, \alpha_R, \beta_R) &= \frac{|R_\zeta\sin\theta_6\sin\theta_9 - \cos\theta_6\cos\theta_9|}{\sqrt{\left|{R_\zeta}^2\sin^2\theta_6 + \cos^2\theta_6\right|}}\ . \qquad (106)
\end{aligned}$$

Note that there is no symmetry in the co and cross-polarization functions, which is due to the geometrical diffraction coefficient ratio function, $R_\zeta$, although $f_{VV}$ and $f_{HV}$ have similar formats with those of $f_{HH}$ and $f_{VH}$, respectively. Finally, it is worth mentioning that the polarization functions in (103) – (106) are normalized such that

$$f_{VV}{}^2 + f_{HV}{}^2 = 1 \ , \ \ f_{HH}{}^2 + f_{VH}{}^2 = 1 \ . \tag{107}$$

The creeping wave on the human body, naturally, tends to have a general direction, which is from the Tx to the Rx. Therefore, the channel modeling parameters regarding the AAoA/EAoA distribution can be adjusted to reflect the general direction of the creeping wave on the channel model as will be seen in Sect. 4.4. The creeping wave usually has the twice path loss exponent of the CSS and GS propagation modes because of the large diffraction loss around the body [32, 33]. Moreover the BS component suffers higher path losses and shadow standard deviations than the CSS or GS components as shown in [30].

## *4.2 GS Propagation Mode in BAN Channels*

Ground scattering is an important component in BAN channels, since the ground often exists at a very short distance from both the Tx and Rx, as reported previously in the literature [34, 36, 37]. The GS propagation mode is almost always present as a dominant propagation component, particularly when the Tx and Rx are located on different sides of the body, since the creeping wave is severely attenuated owing to the multiple diffraction [34, 36, 37]. It will be shown later in Sect. 4.4 that the GS propagation components dominate the BAN channel characteristics. This section suggests a novel geometrical model for the GS propagation mode, and derives the corresponding channel polarization functions.

Our geometrical model for the GS propagation mode is described in Figure 19 where scatterers are distributed on the circumference of a circle on the ground in the vicinity of both the Tx and Rx. Again, similar to the CSS propagation mode, both the Tx and Rx are located inside the ground circle. The scattering circle is characterized by its radius $R_r$, and the AAoA $\alpha_R$ and EAoA $\beta_R$ are defined in the same fashion as in Sect. 4.1. For the GS waves, the polarization functions can be derived as a function of $\alpha_R$, $R_r$, and the horizontal distance between the Tx and Rx antennas, $D$.

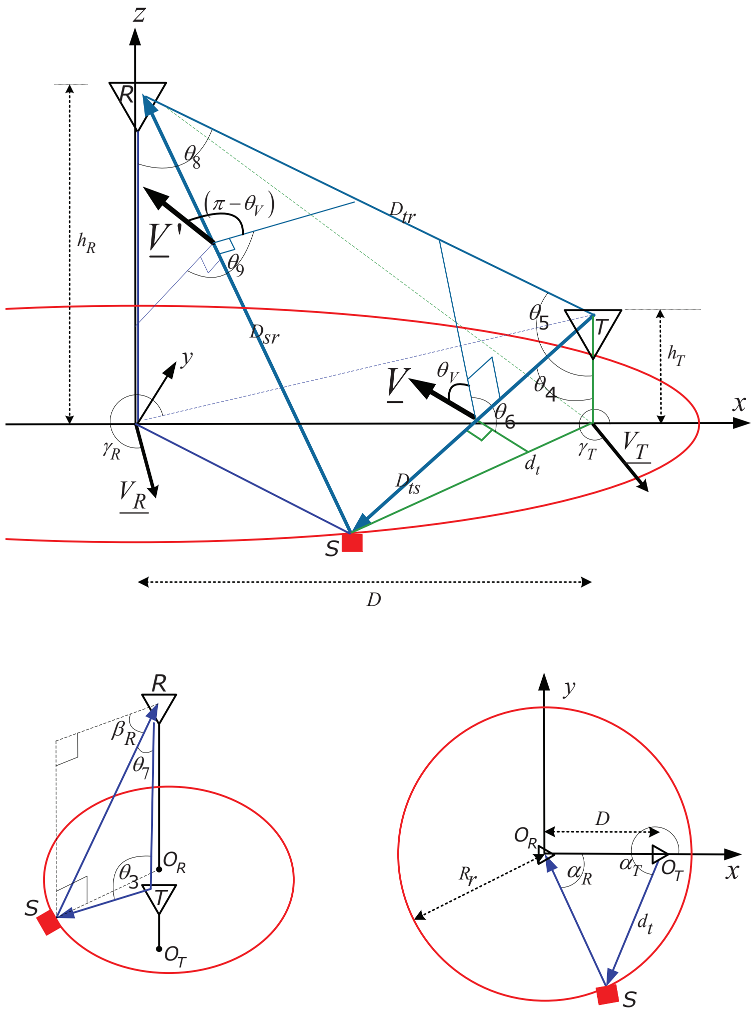

**Figure 19:** 3-D ground scattering (GS) model for BAN channels.

Figure 19 portrays the mechanism of the GS propagation mode. Similar to the CSS propagation mode described in Sect. 4.1, the cross-polarization components arising from the GS propagation mode tend to be dominated by $\alpha_R$ and $R_r$.

We first consider a single vertically polarized GS plane wave from the Tx. The polarization angle of $\underline{V}$, $\phi_V$, in Figure 19 is defined as the angle between $\underline{V}$ and the line that includes the projection of $\underline{V}$ onto the corresponding CoP-plane. Then the angle between $\underline{V}$' and a line that includes its projection onto the CoP-plane is assumed to be equal to $\pi - \phi_V$, as stated in Sect. 4.1 [9]. The geometry in Figure 19 implies that the amplitude of the received GS plane wave at a vertically and horizontally polarized Rx antenna, $A_{VV}^{GS}$ and $A_{HV}^{GS}$, respectively, can be expressed as

$$\begin{bmatrix} A_{VV}^{GS} \\ A_{HV}^{GS} \end{bmatrix} = A_V^{GS} \begin{bmatrix} f_{VV}^{GS}(D, D_{ts}, D_{sr}, R_r, \alpha_R) \\ f_{HV}^{GS}(D, D_{ts}, D_{sr}, R_r, \alpha_R) \end{bmatrix}, \tag{108}$$

where $A_V^{GS}$ is the amplitude of $\underline{V}$' at the Rx antenna. From the geometry in Figure 19, the distances are

$$\begin{aligned} d_t &= \sqrt{(D - R_r \cos\alpha_R)^2 + (R_r \sin\alpha_R)^2}, &(109)\\ D_{ts} &= \sqrt{{d_t}^2 + {h_T}^2}, &(110)\\ D_{sr} &= \sqrt{{R_r}^2 + {h_R}^2},\ \ D_{tr} = \sqrt{D^2 + {\Delta_h}^2}, &(111)\\ D_{OT} &= \sqrt{D^2 + {h_T}^2},\ \ D_{O_TR} = \sqrt{D^2 + {h_R}^2}, &(112) \end{aligned}$$

where $\Delta_h = (h_T - h_R)$. Based on (109) – (112) and the law of cosines, the angles in Figure 19 can be written as

$$\begin{aligned} \cos\theta_3 &= \frac{{D_{ts}}^2 + {D_{tr}}^2 - {D_{sr}}^2}{2 D_{ts} D_{tr}} \\ &= \frac{{b_1}^2 - b_1 \cos\alpha_R + b_2 - b_1 b_2}{\sqrt{\left(1 + {b_1}^2 - 2b_1\cos\alpha_R + {b_2}^2\right)\left({b_1}^2 + {b_2}^2 + {b_3}^2 - 2b_1 b_2\right)}}, &(113)\\ \cos\theta_4 &= \frac{h_t}{D_{ts}} = \frac{b_2}{\sqrt{1 + {b_1}^2 - 2b_1\cos\alpha_R + {b_2}^2}}, &(114)\\ \cos\theta_5 &= \frac{{D_{tr}}^2 + {h_T}^2 - D_{O_TR}}{2 D_{tr} h_T} = \frac{{b_2}^2 - b_2 b_3}{b_2\sqrt{\left({b_1}^2 + {b_2}^2 + {b_3}^2 - 2b_2 b_3\right)}}, &(115)\\ \cos\theta_6 &= \frac{\cos\theta_5 - \cos\theta_3\cos\theta_4}{\sqrt{(1 - \cos^2\theta_3)(1 - \cos^2\theta_4)}},\ \ \theta_V = \pi - \theta_6, &(116) \end{aligned}$$

$$\begin{aligned}
\cos\theta_7 &= \frac{{D_{sr}}^2 + {D_{tr}}^2 - {D_{ts}}^2}{2D_{sr}D_{tr}} = \frac{b_1\cos\alpha_R - b_2b_3 + {b_3}^2}{\sqrt{\left(1+{b_3}^2\right)\left({b_1}^2+{b_2}^2+{b_3}^2-2b_2b_3\right)}}, && (117)\\
\cos\theta_8 &= \frac{{D_{tr}}^2 + {h_R}^2 - {D_{OT}}^2}{2D_{tr}h_R} = \frac{-b_2b_3 + {b_3}^2}{b_3\sqrt{\left({b_1}^2+{b_2}^2+{b_3}^2-2b_2b_3\right)}}, && (118)\\
\cos\theta_9 &= \frac{\cos\theta_8 - \cos\theta_7\cos\beta_R}{\sqrt{(1-\cos^2\theta_7)\,(1-\cos^2\beta_R)}}, && (119)\\
b_1 &= \frac{D}{R_r},\;\; b_2 = \frac{h_T}{R_r},\;\; b_3 = \frac{h_R}{R_r}, && (120)
\end{aligned}$$

Finally, $\cos\theta_6$ and $\cos\theta_9$ in (116) and (119), respectively, are used to derive the channel polarization functions $f_{VV}^{GS}$, $f_{HV}^{GS}$, $f_{HH}^{GS}$ and $f_{VH}^{GS}$ in (108).

The amplitudes of the vertical and horizontal polarization components at the Rx antenna in (108) are, respectively,

$$\begin{aligned}
A_{VV}^{GS} &= A_V^{GS}\left|\cos\left(\theta_9 + (\pi - \theta_V) - \pi\right)\right|\\
&= A_V^{GS}\left|\cos\theta_6\cos\theta_9 - \sqrt{1-\cos^2\theta_6}\sqrt{1-\cos^2\theta_9}\right|\;, && (121)\\
A_{HV}^{GS} &= A_V^{GS}\left|\sin\left(\theta_9 + (\pi - \theta_V) - \pi\right)\right|\\
&= A_V^{GS}\left|\cos\theta_6\sqrt{1-\cos^2\theta_9} + \cos\theta_9\sqrt{1-\cos^2\theta_6}\right|\;, && (122)
\end{aligned}$$

From (109) – (120), $\cos\theta_6$ and $\cos\theta_9$ in (116) and (119) can be expressed as a function of $D$, $R_r$ and $\alpha_R$. Comparing (121) and (122) with (108), the GS channel polarization functions $f_{VV}^{GS}$ and $f_{HV}^{GS}$ can be written as:

$$\begin{aligned}
& f_{VV}^{GS}(D, D_{ts}, D_{sr}, R_r, \alpha_R, \beta_R)\\
&\equiv f_{VV}^{GS}(D, R_r, \alpha_R)\\
&= \left|\cos\theta_6\sqrt{1-\cos^2\theta_9} + \cos\theta_9\sqrt{1-\cos^2\theta_6}\right|\;, && (123)\\
& f_{HV}^{GS}(D, D_{ts}, D_{sr}, R_t, \alpha_R, \beta_R)\\
&\equiv f_{HV}^{GS}(D, R_r, \alpha_R)\\
&= \left|\cos\theta_6\cos\theta_9 - \sqrt{1-\cos^2\theta_6}\sqrt{1-\cos^2\theta_9}\right|\;. && (124)
\end{aligned}$$

Similar to the CSS propagation mode, a symmetry exists in the GS channel polarization functions such that

$$f_{VH}^{GS} = f_{HV}^{GS}, \; f_{HH}^{GS} = f_{VV}^{GS} \; . \tag{125}$$

## 4.3 Statistical Model for Polarized BAN Channels

### 4.3.1 Input Delay-spread Function and Time-variant Transfer Function

The BAN polarized multi-path fading channels can be modeled by using the channel polarization functions for the CSS propagation mode in (88) – (91), the BS propagation mode in (103) – (106), and the GS propagation mode in (123) – (125) along with the conventional input delay-spread function of the copolarized channel. Lastly, by embedding a path loss model into the polarized BAN channel model, we can obtain a *wide-band* polarized BAN channel as described in the sequel.

We first consider the case of vertically polarized Tx antenna and a horizontally polarized Rx antenna (HV-channel). The complex low-pass channel input delay-spread function for the HV-channel with CSS, GS, BS and LoS propagation modes can be expressed as:

$$h_{HV}^{BAN}(t,\tau) \;=\; h_{HV}^{CSS}(t,\tau) + h_{HV}^{GS}(t,\tau) + h_{HV}^{BS}(t,\tau) + h_{HV}^{LoS}(t,\tau), \tag{126}$$

where,

$$\begin{aligned}
h_{HV}^{CSS}(t,\tau) &= \sum_{n=1}^{N^{CSS}} \left( A_{V,n}^{CSS} f_{HV,n}^{CSS} \; e^{j\phi_n^{CSS}(t)} \; \delta(\tau - \tau_n) \right), &(127)\\
h_{HV}^{GS}(t,\tau) &= \sum_{n=1}^{N^{GS}} \left( A_{V,n}^{GS} f_{HV,n}^{GS} \; e^{j\phi_n^{GS}(t)} \; \delta(\tau - \tau_n) \right), &(128)\\
h_{HV}^{BS}(t,\tau) &= \sum_{n=1}^{N^{BS}} \left( A_{V,n}^{BS} f_{HV,n}^{BS} \; e^{j\phi_n^{BS}(t)} \; \delta(\tau - \tau_n) \right), &(129)\\
h_{HV}^{LoS}(t,\tau) &= A_{V}^{LoS} \; e^{j\phi^{LoS}(t)} \; \delta(\tau - \tau^{LoS}), &(130)
\end{aligned}$$

and where the amplitudes and phases are

$$
\begin{aligned}
A_{V,n}^{CSS} &= A_V^{CSS}(\alpha_{R,n}, \beta_{R,n}, R_{r,n}^{CSS}) \\
&= \frac{A_V^{\mathrm{T_x}}}{\sqrt{10^{P_{\text{loss, dB}}^{\text{co}-\text{Pol}}(\alpha_{R,n},\beta_{R,n},R_{r,n}^{CSS})/10}}}\,, \qquad (131) \\
A_{V,n}^{GS} &= A_V^{GS}(\alpha_{R,n}, R_{r,n}^{GS}), \\
&= \frac{A_V^{\mathrm{T_x}}}{\sqrt{10^{P_{\text{loss, dB}}^{\text{co}-\text{Pol}}(\alpha_{R,n},R_{r,n}^{GS})/10}}}\,, \qquad (132) \\
A_{V,n}^{BS} &= A_V^{BS}(\alpha_{R,n}, \beta_{R,n}, R_{r,n}^{BS}) \\
&= \frac{A_V^{\mathrm{T_x}}}{\sqrt{10^{P_{\text{loss, dB}}^{\text{co}-\text{Pol}}(\alpha_{R,n},\beta_{R,n},R_{r,n}^{BS})/10}}}\,, \qquad (133) \\
\phi_n^{\text{case}}(t) &= -2\pi\left((f_c + f_{D,n}^{\text{case}})\tau_n - f_{D,n}^{\text{case}}\ t\right) + \phi_n^{\text{case}}, \qquad (134) \\
\tau_n &= (D_{ts,n}^{\text{case}} + D_{sr,n}^{\text{case}})/c_0 \ \text{ for case} \in \{CSS, GS, BS\}, \qquad (135) \\
\phi^{LoS}(t) &= -2\pi\left((f_c + f_D^{LoS})\tau^{LoS} - f_D^{LoS}\ t\right),\ \tau^{LoS} = D_{tr}/c_0. \qquad (136)
\end{aligned}
$$

Notice that the path losses for the different paths, indexed by $n$, are taken into account, and the path loss model is expressed as

$$P_{\text{loss, dB}}^{\text{co}-\text{Pol}}(\alpha_{R,n}, \beta_{R,n}, R_{r,n}^{CSS}) = P_{0,\text{loss}}^{\text{co}-\text{Pol}} + 10\beta\log\left((D_{ts,n}^{CSS} + D_{sr,n}^{CSS})/d_0\right), \tag{137}$$

$$P_{\text{loss, dB}}^{\text{co}-\text{Pol}}(\alpha_{R,n}, R_{r,n}^{GS}) = P_{0,\text{loss}}^{\text{co}-\text{Pol}} + 10\beta\log\left((D_{ts,n}^{GS} + D_{sr,n}^{GS})/d_0\right), \tag{138}$$

$$P_{\text{loss, dB}}^{\text{co}-\text{Pol}}(\alpha_{R,n}, \beta_{R,n}, R_{r,n}^{BS}) = P_{0,\text{loss}}^{\text{co}-\text{Pol}} + 20\beta\log\left((D_{ts,n}^{BS} + D_{sr,n}^{BS})/d_0\right), \tag{139}$$

where $P_{0,\text{loss}}^{\text{co}-\text{Pol}}$ is the path loss in dB at a reference distance $d_0$, and $\beta$ is the path loss exponent. Empirically derived values for $d_0$ and $\beta$ will be provided in Sect. 4.4. In (134) – (136), the Doppler and carrier frequencies are

$$
\begin{aligned}
f_{D,n}^{\text{case}} &= (v_R/\lambda)\cos\beta_{R,n}\cos(\gamma_R - \alpha_{R,n}) + (v_T/\lambda)\cos\beta_{T,n}^{\text{case}}\cos\left(\gamma_T - \alpha_{T,n}^{\text{case}}\right) \\
&\quad \text{for case} \in \{CSS, GS, BS\}, \qquad (140) \\
f_D^{LoS} &= \frac{D}{\sqrt{D^2 + {\Delta_h}^2}}\left((v_R/\lambda)\cos(\gamma_R - \pi) + (v_T/\lambda)\cos\gamma_T\right), \qquad (141) \\
f_c &= c_0/\lambda. \qquad (142)
\end{aligned}
$$

Here, $v_T$ and $v_R$ ($\gamma_T$ and $\gamma_R$) are the velocities (moving directions with respect to the positive $x$-axis) of the Tx and Rx, respectively. For large $N^{\text{case}}$, case $\in$

$\{CSS, GS, BS\}$ in (127) – (129), the central limit theorem can be invoked and $h_{HV}^{BAN}(t,\tau)$ in (126) can be treated as complex Gaussian random process. The term $h_{HV}^{LoS}(t,\tau)$ in (126) is the LoS component, and the terms $h_{HV}^{CSS}(t,\tau)$, $h_{HV}^{GS}(t,\tau)$ and $h_{HV}^{BS}(t,\tau)$ contribute to the diffuse component of the received complex fading envelope. The channel polarization functions can be expressed as:

$$f_{HV,n}^{\text{case}} \;=\; f_{HV}^{\text{case}}\left(D, R_r, \alpha_{R,n}, \beta_{R,n}\right) \text{ for case} \in \{CSS, GS, BS\}. \qquad (143)$$

It is assumed that the phases $\{\phi_n^{\text{case}}\}$ with case $\in \{CSS, GS, BS\}$ are independent and identically distributed (i.i.d.) uniform random variables on the interval $[-\pi, \pi)$, and independent of the A/EAoDs, A/EAoAs, and the radii of the scattering cylinders/circles.

The time-variant transfer function, which is the Fourier transform of the channel input delay-spread function, is needed to derive the time-frequency correlation function (TF-CF) of the channel. Later we will compare the frequency correlation function of the proposed theoretical model with that obtained from empirical measurements in Sect. 4.4. From (126) – (130), the time-variant transfer function of the BAN polarized channel is

$$\begin{aligned} T_{HV}^{BAN}(t,f) &= \mathcal{F}_\tau\left\{h_{HV}^{BAN}(t,\tau)\right\} \\ &= T_{HV}^{CSS}(t,f) + T_{HV}^{GS}(t,f) + T_{HV}^{BS}(t,f) + T_{HV}^{LoS}(t,f), \end{aligned} \qquad (144)$$

where

$$\begin{aligned} T_{HV}^{\text{case}}(t,f) &= \mathcal{F}_\tau\left\{h_{HV}^{\text{case}}(t,\tau)\right\} \\ &= \sum_{n=1}^{N^{\text{case}}} \left(A_{V,n}^{\text{case}} f_{HV,n}^{\text{case}}\; e^{j\phi_n^{\text{case}}(t)}\; e^{-j2\pi f\tau_n}\right) \text{ for case} \in \{CSS, GS, BS\}, \end{aligned} \qquad (145)$$

and

$$\begin{aligned} T_{HV}^{LoS}(t,f) &= \mathcal{F}_\tau\left\{h_{HV}^{LoS}(t,\tau)\right\} \\ &= A_V^{LoS}\; e^{j\phi_n^{LoS}(t)}\; e^{-j2\pi f\tau^{LoS}}. \end{aligned} \qquad (146)$$

In a similar fashion, the channel input delay-spread functions (time-variant transfer functions) for the VV-, VH- and HH-channels, given by $h_{VV}^{BAN}(t,\tau)$ $(T_{VV}^{BAN}(t,f))$, $h_{VH}^{BAN}(t,\tau)$ $(T_{VH}^{BAN}(t,f))$ and $h_{HH}^{BAN}(t,\tau)$ $(T_{HH}^{BAN}(t,f))$, respectively, can be obtained with their polarization functions, $f_{VV}^{\text{case}}$, $f_{VH}^{\text{case}}$ and $f_{HH}^{\text{case}}$ with case $\in \{CSS, GS, BS\}$, respectively.

### 4.3.2 Received Signal Power and XPD of the Polarized BAN Channel

By using the complex low-pass channel input delay-spread function and the aforementioned properties, it is straightforward to obtain the received power through the HV-channel at the Rx as follows:

$$\begin{aligned} P_{HV}^{BAN} &= P_{HV}^{CSS} + P_{HV}^{GS} + P_{HV}^{BS} + P_{HV}^{LoS} \\ &= (1+K)\left(P_{HV}^{CSS} + P_{HV}^{GS} + P_{HV}^{BS}\right), \end{aligned} \tag{147}$$

where

$$\begin{aligned} P_{HV}^{CSS} &= \frac{1}{2}\mathrm{E}\left[\left|h_{HV}^{CSS}(t,\tau)\right|^2\right] \\ &= \frac{1}{2}\mathrm{E}\left[\left(\sum_{n=1}^{N^{CSS}} A_{V,n}^{CSS} f_{HV,n}^{CSS}\, e^{j\phi_n(t)}\right)\left(\sum_{m=1}^{N^{CSS}} A_{V,n}^{CSS} f_{HV,n}^{CSS}\, e^{-j\phi_m(t)}\right)\right] \\ &= \frac{1}{2}\mathrm{E}\left[\sum_{n=1}^{N^{CSS}} \left(A_{V,n}^{CSS} f_{HV,n}^{CSS}\right)^2\right], \end{aligned} \tag{148}$$

$$P_{HV}^{GS} = \frac{1}{2}\mathrm{E}\left[\left|h_{HV}^{GS}(t,\tau)\right|^2\right] = \frac{1}{2}\mathrm{E}\left[\sum_{n=1}^{N^{GS}} \left(A_{V,n}^{GS} f_{HV,n}^{GS}\right)^2\right], \tag{149}$$

$$P_{HV}^{BS} = \frac{1}{2}\mathrm{E}\left[\left|h_{HV}^{BS}(t,\tau)\right|^2\right] = \frac{1}{2}\mathrm{E}\left[\sum_{n=1}^{N^{BS}} \left(A_{V,n}^{BS} f_{HV,n}^{BS}\right)^2\right], \tag{150}$$

$$P_{HV}^{LoS} = \frac{1}{2}\left|A_V^{LoS}\right|^2 = K\left(P_{HV}^{CSS} + P_{HV}^{GS} + P_{HV}^{BS}\right). \tag{151}$$

The parameter $K$ in (147) is the Ricean K-factor, which is assumed zero for the cross-polarization (VH or HV) components, since these components are due to scattering and contain no LoS component. The third equality in (148) is due to the fact that the phases $\{\phi_n^{\text{case}}\}$ with case $\in \{CSS, GS, BS\}$ in (134) are i.i.d. uniform random variables on the interval $[-\pi, \pi)$. Further, as $N_i \to \infty$, the discrete AAoAs, $\alpha_{R,n}$, and discrete EAoAs, $\beta_{R,n}$, can be replaced with continuous random variables $\alpha_R$ and $\beta_R$ having the joint probability density function (pdf), $p(\alpha_R, \beta_R)$. Here, we assume that the azimuth and elevation angles of arrival are independent of each other such that the joint pdf $p(\alpha_R, \beta_R)$ can be decomposed as $p(\alpha_R)p(\beta_R)$. The total power of the vertical and horizontal polarization components can be derived via the superposition of the CoP-plane components by averaging over the pdfs of the AAoA and EAoA, $p(\alpha_R)$ and $p(\beta_R)$, respectively by taking into account the statistical distribution of scatterers. It follows that for the HV-channel and CSS component,

$$P_{HV}^{CSS} = \frac{1}{2}\int_{-\pi}^{\pi}\int_{-\beta_{R,Max}}^{\beta_{R,Max}} \left(A_V^{CSS} f_{HV}^{CSS}\right)^2_{(D,R_r,\alpha_R,\beta_R)} p_r\left(\beta_R\right) p_r\left(\alpha_R\right)\ d\beta_R d\alpha_R\ , \quad (152)$$

where $\beta_{R,Max}$ is the absolute value of the maximum EAoA. It is worth clarifying that not only $f_{HV}^{CSS}$ but also $A_V^{CSS}$ is a function of $D, R_r, \alpha_R, \beta_R$ since the path loss model is embedded in $A_V^{CSS}$.

Similar to (152), the received power of the CSS propagation mode at the Rx with a vertically polarized Rx antenna and a vertically polarized Tx antenna (VV-channel), a vertically polarized Rx antenna and a horizontally polarized Tx antenna (VH-channel), and horizontally polarized Rx and Tx antennas (HH-channel), denoted by $P_{VV}^{CSS}$, $P_{VH}^{CSS}$, and $P_{HH}^{CSS}$, respectively, can be expressed as:

$$P_{VV}^{CSS} = \frac{1}{2}\int_{-\pi}^{\pi}\int_{-\beta_{R,Max}}^{\beta_{R,Max}} \left(A_V^{CSS} f_{VV}^{CSS}\right)^2_{(D,R_r,\alpha_R,\beta_R)} p_r\left(\beta_R\right) p_r\left(\alpha_R\right)\ d\beta_R d\alpha_R\ , \quad (153)$$

$$P_{VH}^{CSS} = \frac{1}{2}\int_{-\pi}^{\pi}\int_{-\beta_{R,Max}}^{\beta_{R,Max}} \left(A_H^{CSS} f_{VH}^{CSS}\right)^2_{(D,R_r,\alpha_R,\beta_R)} p_r\left(\beta_R\right) p_r\left(\alpha_R\right)\ d\beta_R d\alpha_R\ , \quad (154)$$

$$P_{HH}^{CSS} = \frac{1}{2}\int_{-\pi}^{\pi}\int_{-\beta_{R,Max}}^{\beta_{R,Max}} \left(A_H^{CSS} f_{HH}^{CSS}\right)^2_{(D,R_r,\alpha_R,\beta_R)} p_r\left(\beta_R\right) p_r\left(\alpha_R\right)\ d\beta_R d\alpha_R\ . \quad (155)$$

The received power for the BS propagation mode, $P_{VV}^{BS}$, $P_{HV}^{BS}$, $P_{VH}^{BS}$ and $P_{HH}^{BS}$, can be obtained from the CSS model with values for the modeling parameters, particularly the scattering radius $R_r$, that are appropriate for the BS propagation mode and replacing $\left(A_V^{CSS} f_{HV}^{CSS}\right)$, $\left(A_V^{CSS} f_{VV}^{CSS}\right)$, $\left(A_V^{CSS} f_{VH}^{CSS}\right)$ and $\left(A_V^{CSS} f_{HH}^{CSS}\right)$ with $\left(A_V^{BS} f_{HV}^{BS}\right)$, $\left(A_V^{BS} f_{VV}^{BS}\right)$, $\left(A_V^{BS} f_{VH}^{BS}\right)$ and $\left(A_V^{BS} f_{HH}^{BS}\right)$, respectively.

Several different distributions have been suggested in the literature to characterize the AAoA distribution in various radio propagation environments, such as uniform, Gaussian and Laplacian. Here we use the von Mises distribution, defined as [52]

$$p_r\left(\alpha_R\right) = \frac{\exp[k_R \cos(\alpha_R - \mu_R)]}{2\pi I_0(k_R)}\ ,\ k_R \geq 0\ , \quad (156)$$

where $\alpha_R \in [-\pi, \pi)$, $I_0(\ \cdot\ )$ is the zero-order modified Bessel function of the first kind, $\mu_R \in [-\pi, \pi)$ is the mean AAoA of the scatterers in the $x$ - $y$ plane with respect to the positive $x$ axis, and $k_R$ controls the spread of the scatterers around the mean AAoA $\mu_R$. When $k_R = 0$ the von Mises distribution reduces to the uniform distribution $p_r\left(\alpha_R\right) = 1/(2\pi)$ corresponding to isotropic azimuthal scattering, while as $k_R$ increases the AAoA distribution becomes increasingly nonisotropic and concentrated around the mean AAoA, $\mu_R$ [52]. For the EAoA distribution, we use the cosine pdf [50]

$$p_r\left(\beta_R\right) = \frac{\pi}{4\beta_{R,Max}} \cos\left(\frac{\pi}{2}\frac{\beta_R}{\beta_{R,Max}}\right)\ , \quad (157)$$

$$|\beta_R| \leq \beta_{R,Max} \leq \pi/2\ , \quad (158)$$

Of course, other suitable distributions for $p_r\left(\alpha_R\right)$ and $p_r\left(\beta_R\right)$ can be used as well at this stage that may be more or less effective. The antenna gain pattern can also be considered in our theoretical channel model by adjusting parameters relating AAoA and EAoA distributions in (156) – (158) in a similar manner with our earlier work in [9].

In a manner analogous with (148) and (152) – (155), the power received at the Rx in the GS propagation mode can be written as

$$P_{HV}^{GS} = \frac{1}{2}\int_{-\pi}^{\pi} \left(A_V^{GS} f_{HV}^{GS}\right)^2_{(D,R_r,\alpha_R)} p_r\left(\alpha_R\right) d\alpha_R \ , \tag{159}$$

$$P_{VV}^{GS} = \frac{1}{2}\int_{-\pi}^{\pi} \left(A_V^{GS} f_{VV}^{GS}\right)^2_{(D,R_r,\alpha_R)} p_r\left(\alpha_R\right) d\alpha_R \ , \tag{160}$$

$$P_{VH}^{GS} = \frac{1}{2}\int_{-\pi}^{\pi} \left(A_V^{GS} f_{VH}^{GS}\right)^2_{(D,R_r,\alpha_R)} p_r\left(\alpha_R\right) d\alpha_R \ , \tag{161}$$

$$P_{HH}^{GS} = \frac{1}{2}\int_{-\pi}^{\pi} \left(A_V^{GS} f_{HH}^{GS}\right)^2_{(D,R_r,\alpha_R)} p_r\left(\alpha_R\right) d\alpha_R \ . \tag{162}$$

Note that for the GS plane waves, the AAoDs and EAoDs, and also the EAoAs $\beta_R$ are dependent upon and are fixed by the AAoAs $\alpha_R$ and the radius of the ground circle $R_r$. Hence, only the scattering distribution for $\alpha_R$ needs to be taken into account in (159) – (162). In the same manner as (147), we can obtain $P_{VV}^{BAN}$, $P_{VH}^{BAN}$ and $P_{HH}^{BAN}$ using (153) – (155) and (159) – (162).

Finally, the average XPD values can obtained from (147) and its variants for $P_{VV}^{BAN}$, $P_{VH}^{BAN}$ and $P_{HH}^{BAN}$, as

$$\overline{XPD}_{VV/HV}^{BAN} = \frac{P_{VV}^{BAN}}{P_{HV}^{BAN}} \ , \ \overline{XPD}_{HH/VH}^{BAN} = \frac{P_{HH}^{BAN}}{P_{VH}^{BAN}} \ . \tag{163}$$

### 4.3.3 Time-frequency Correlation Function

The time-frequency correlation function (TF-CF) is an important statistical function for the wireless communication channel and, in particular, the frequency correlation function (F-CF) is utilized to validate our theoretical model with measurement data in this chapter. The normalized TF-CF is obtained from time-variant transfer function in (144) as

$$R^{BAN}_{HV,HV}(\Delta t, \Delta f) \;\triangleq\; \frac{\mathrm{E}\left[T^{BAN}_{HV}(t,f)^{*}\; T^{BAN}_{HV}(t+\Delta t, f+\Delta f)\,\right]}{\mathrm{E}\left[\left|T^{BAN}_{HV}(t,f)\,\right|^{2}\right]}\;. \tag{164}$$

The time-variant transfer functions of CSS, GS and BS propagation modes, $T^{CSS}_{HV}(t,f)$, $T^{GS}_{HV}(t,f)$ and $T^{BS}_{HV}(t,f)$ are independent zero-mean complex Gaussian random processes. Therefore,

$$\begin{aligned} R^{BAN}_{HV,HV}(\Delta t, \Delta f) \;&=\; R^{CSS}_{HV,HV}(\Delta t, \Delta f) + R^{GS}_{HV,HV}(\Delta t, \Delta f) + R^{BS}_{HV,HV}(\Delta t, \Delta f) \\ &+\; R^{LoS}_{HV,HV}(\Delta t, \Delta f), \end{aligned} \tag{165}$$

where

$$R^{\text{case}}_{HV,HV}(\Delta t, \Delta f) \triangleq \frac{\mathrm{E}\left[T^{\text{case}}_{HV}(t,f)^{*}\; T^{\text{case}}_{HV}(t+\Delta t, f+\Delta f)\,\right]}{\mathrm{E}\left[\left|T^{\text{case}}_{HV}(t,f)\,\right|^{2}\right]} \tag{166}$$

$$\text{for case} \in \{CSS, GS, BS, LoS\}$$

$$= \begin{cases} \dfrac{\sum\limits_{n=1}^{N^{\text{case}}} \mathrm{E}\left[\left(A^{\text{case}}_{V,n} f^{\text{case}}_{HV,n}\right)^{2}\; e^{j2\pi\left(f_{D,n}\Delta t - \Delta f \tau_n\right)}\right]}{\mathrm{E}\left[\left|T^{\text{case}}_{HV}(t,f)\,\right|^{2}\right]} & \text{for case} \in \{CSS, GS, BS\}, \\ e^{j2\pi\left(f^{LoS}_{D}\Delta t - \Delta f \tau^{LoS}\right)} & \text{for case} = LoS. \end{cases} \tag{167}$$

In other words, the TF-CF of the wide-band BAN polarized fading channel is the sum of TF-CFs of CSS, GS, BS and LoS propagation modes if each of them exists. Further, the TF-CF of each propagation mode can be expressed as:

$$R^{CSS/BS}_{HV,HV}(\Delta t, \Delta f) = \tag{168}$$

$$\frac{\frac{1}{2}\int\limits_{-\pi}^{\pi}\int\limits_{-\beta_{R,Max}}^{\beta_{R,Max}} \left(A^{CSS/BS}_{V} f^{CSS/BS}_{HV}\right)^{2}_{(D,R_r,\alpha_R,\beta_R)} e^{j2\pi\left(f_{D,n}\Delta t - \Delta f \tau_n\right)}\; p_r\left(\beta_R\right) p_r\left(\alpha_R\right) d\beta_R d\alpha_R}{P^{CSS/BS}_{HV}}\;,$$

$$R^{GS}_{HV,HV}(\Delta t, \Delta f) =$$

$$\frac{\frac{1}{2}\int\limits_{-\pi}^{\pi}\int\limits_{-\beta_{R,Max}}^{\beta_{R,Max}} \left(A^{GS}_{V} f^{GS}_{HV}\right)^{2}_{(D,R_r,\alpha_R)} e^{j2\pi\left(f_{D,n}\Delta t - \Delta f \tau_n\right)}\; p_r\left(\alpha_R\right) p_r\left(R_r\right)\; d\alpha_R dR_r}{P^{GS}_{HV}}\;. \tag{169}$$

Again, $A_V^{CSS/BS}$ in (168) and $A_V^{GS}$ in (169) includes the path loss model, and they depend on each propagation path that is represented by $D$, $R_r$, $\alpha_R$ and $\beta_R$. The TF-CFs of the VV, VH and HH-channels, $R^{BAN}_{VV,VV}(\Delta t, \Delta f)$, $R^{BAN}_{VH,VH}(\Delta t, \Delta f)$ and $R^{BAN}_{HH,HH}(\Delta t, \Delta f)$, can be easily expressed in the same way as that of the HV-channel. Therefore, their derivations are omitted.

## 4.4 Reference Model Verification

In this section, we compare analytical results derived from the geometric model developed in Sects. 4.1 – 4.3 with empirical data obtained from our own measurements. Measurements were conducted using custom built patch antennas, similar to the planar rectangular patch antenna on a flat hand-held device layer in [42], but at a carrier frequency of 13 GHz. Note that the carrier frequency is adjustable in our channel models depending on the given system requirement. As in [42], the antenna is lightweight and flexible, and its gain pattern can be regarded as semi-isotropic for the outside direction of the body. Furthermore, this antenna is almost non-sensitive to the background environment below its ground plane as described in [42]; therefore, we could focus on the wireless BAN channel modeling, which is the topic of this chapter, without the consideration of the body-antenna coupling effect. An HP-Agilent N5242A was used as a nonlinear vector network analyzer (VNA), signal generator, and spectrum analyzer, along with an HP-Agilent 85131F flexible cable. The frequency bandwidth is approximately 1 GHz, and the amplitude and phase of the channel impulse response are measured every 13.25 kHz to derive the F-CF.

The free space path loss was measured in an anechoic chamber using the aforementioned equipment. From the empirical data, analytical path loss model is first determined and embedded in the proposed BAN channel model. The incorporation of such a path loss model leads to close agreement between the analytical results from our BAN channel model and those derived from empirical measurements, and it also yields a wide-band model. Our analytical path loss model is derived according to the empirical data in Figure 20. Notice that each empirical data point in the figure is the result of averaging over 800 different measurement values around 13 GHz. The path loss $P_{0,\mathrm{loss}}^{\mathrm{co-Pol}}$ at a reference distance $d_0$ and the path loss exponent $\beta$ in (137) – (139) are

$$P_{0,\mathrm{loss}}^{\mathrm{co-Pol}} = 4.9726 \text{ dB at } d_0 = 16.5 \text{ cm}, \quad (170)$$

$$\beta = 2.7. \quad (171)$$

Figure 20 shows that the path loss model in (137) – (139) with the aforementioned constants, $P_{0,\mathrm{loss}}^{\mathrm{co-Pol}}$, $d_0$ and $\beta$ is in close agreement with the empirical data.

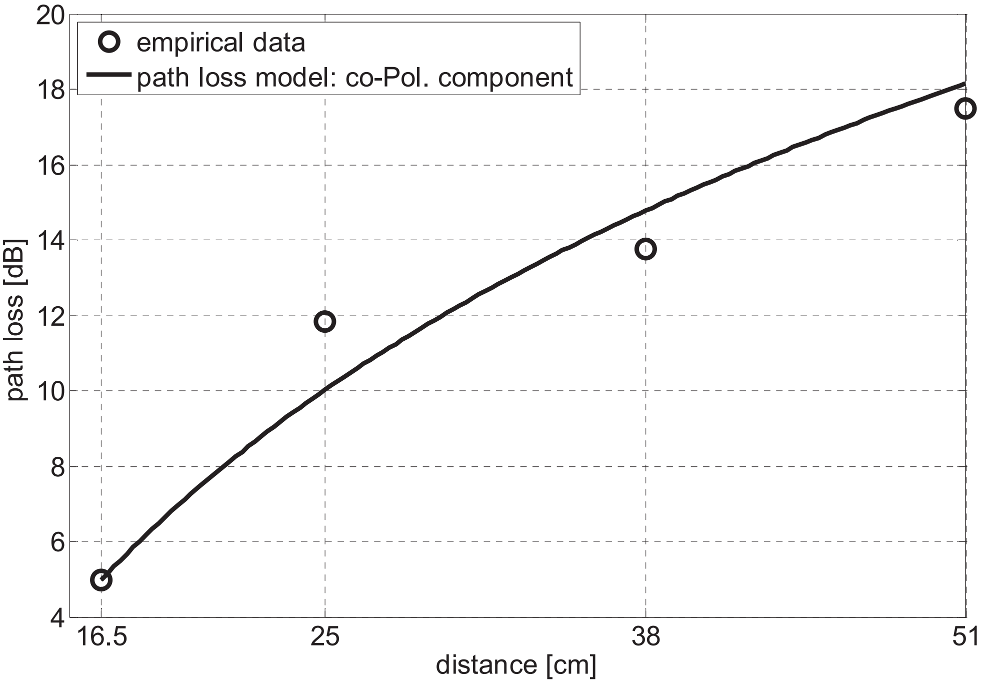

**Figure 20:** Empirical path loss model for 13 GHz BAN channels.

### 4.4.1 Default Parameters of the BAN Channel Model and Measurements

The Tx is located on the left ankle, the left wrist, or the front torso (the center of the abdomen) depending on a given scenario, while the Rx is always located on the back waist. However, the scenario of the Tx on the left ankle and the Rx on the back waist is considered for verification in this section, since we get the similar F-CF results in each scenario. The orientation of the Tx antenna is set to the vertical polarization, whereas that of the Rx antenna is set to both vertical and horizontal polarization for any given scenario, and measurement campaign is performed for each Rx antenna orientation. The distance between the Tx/Rx antenna and body surface is around 1 cm, the human body has no mobility, and maintains standing posture, unless otherwise stated. Finally, this measurement is performed by a normal adult female (55 kg, 163 cm).

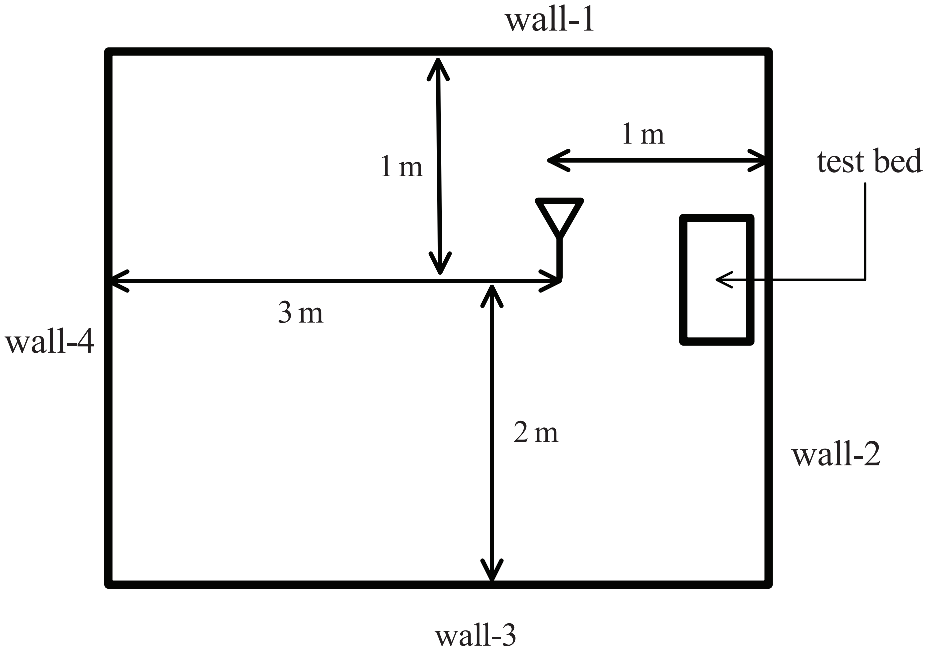

**Figure 21:** Floor plan of the measurement room.

Based on the above descriptions, the fixed parameters in Figures 17 and 19 for the CSS/BS and GS propagation modes, respectively, are $h_T = 0.2$ m, $h_R = 0.5$ m, and $D = 0.4$ m. Figure 21 shows the basic floor plan and configuration of the measurement room. First, the effects of four walls, Wall-1, 2, 3 and 4 are considered by using four cylinders, one cylinder for each wall, along with a composite von Mises distribution having four components, one component for each wall. Later a simplified CSS propagation model will be supplied that just uses a single cylinder and a single von Mises distribution. The modeling parameters corresponding to Wall-1, 2, 3 and 4 are set as:

$$R_1^{CSS} = R_2^{CSS} = 1 \text{ m},\ R_3^{CSS} = 2 \text{ m},\ R_4^{CSS} = 3 \text{ m}, \tag{172}$$

$$\mu_{R,1}^{CSS} = 90^\circ,\ \mu_{R,2}^{CSS} = 0^\circ, \mu_{R,3}^{CSS} = 270^\circ,\ \mu_{R,4}^{CSS} = 180^\circ, \tag{173}$$

$$k_{R,1}^{CSS} = k_{R,2}^{CSS} = k_{R,3}^{CSS} = k_{R,4}^{CSS} = 10, \tag{174}$$

$$\beta_{R,Max}^{CSS} = 15^\circ, \tag{175}$$

where $R_k^{CSS}$, $\mu_{R,k}^{CSS}$ and $k_{R,1}^{CSS}$, $k \in \{1, 2, 3, 4\}$ are, respectively, the radius of the cylinder in Figure 17, mean AAoA and angular spread constant in (156) for wall-$k$ in Figure 21. Further, the parameters for the GS propagation mode are

$$R^{GS} = 0.55 \text{ m},\ \mu_R^{GS} = 30^\circ,\ k_R^{GS} = 0.7. \tag{176}$$

Lastly, the parameters related to the BS propagation mode are as follows:

$$R_r^{BS} = 0.45 \text{ m},\ \mu_R^{BS} = 0^\circ,\ k_R^{BS} = 100,\ \beta_{R,Max}^{BS} = 45^\circ. \tag{177}$$

In the BS propagation mode representing creeping waves, the general propagating direction of the creeping wave is from the Tx to the Rx, which is the rationale that $\mu_R^{BS} = 0^\circ$, and $k_R^{BS}$ is set large value.

### 4.4.2 Model Verification and Results

The F-CF for the CSS propagation mode consists of four F-CF components, corresponding to Wall-1, 2, 3 and 4 in Figure 21, i.e.,

$$\begin{aligned} R_{VV,VV}^{CSS} &= q_1\, R_{VV,VV}^{CSS,1} + q_2\, R_{VV,VV}^{CSS,2} + q_3\, R_{VV,VV}^{CSS,3} + q_4\, R_{VV,VV}^{CSS,4}\ , \\ & \quad q_1 + q_2 + q_3 + q_4 = 1,\ 0 \le q_1,\ q_2,\ q_3,\ q_4 \le 1, \end{aligned} \tag{178}$$

where $R_{VV,VV}^{CSS,k}$, $k \in \{1, 2, 3, 4\}$ is the F-CF of the received signals scattered from Wall-$k$. The weights, $q_1$, $q_2$, $q_3$ and $q_4$ are all set to 1/4 in the analytical results, but they are adjustable according to the given surroundings. The 4-cylinder CSS propagation model utilized to represent corresponding four walls in Figure 21 requires a large number of modeling parameters. Here we simplify it to a 1-cylinder CSS propagation model by considering only the dominant scatterers. Here, the simplified 1-cylinder CSS propagation modeling parameters are chosen as

$$R^{CSS} = 1 \text{ m}, \ \mu_R^{CSS} = 90^\circ, \ k_R^{CSS} = 1, \tag{179}$$

while the other parameters are same as described in Sect. 4.4.1.

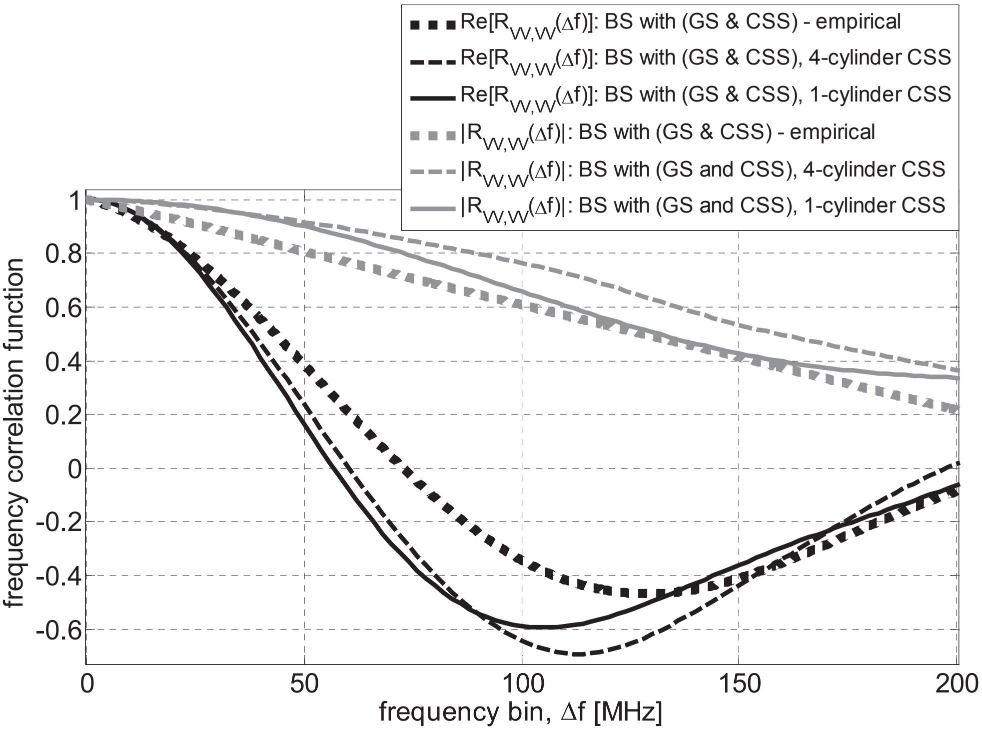

**Figure 22:** Comparison of the frequency correlation (F-CF) functions utilizing 4-cylinder CSS and simplified 1-cylinder CSS propagation models with the empirical F-CF.

The final F-CF utilizing a 1-cylinder CSS propagation model is portrayed together along with the F-CF using a 4-cylinder CSS propagation model and the empirical F-CF in Figure 22. In case of VV-channel, the 1-cylinder CSS propagation model and measurement data have less than half difference between the 4-cylinder CSS propagation model and measurement data. Clearly, a 1-cylinder CSS propagation model is in good agreement with the empirical F-CF and represents a good tradeoff between modeling complexity and modeling accuracy. Subsequent results below assume a 1-cylinder CSS model.

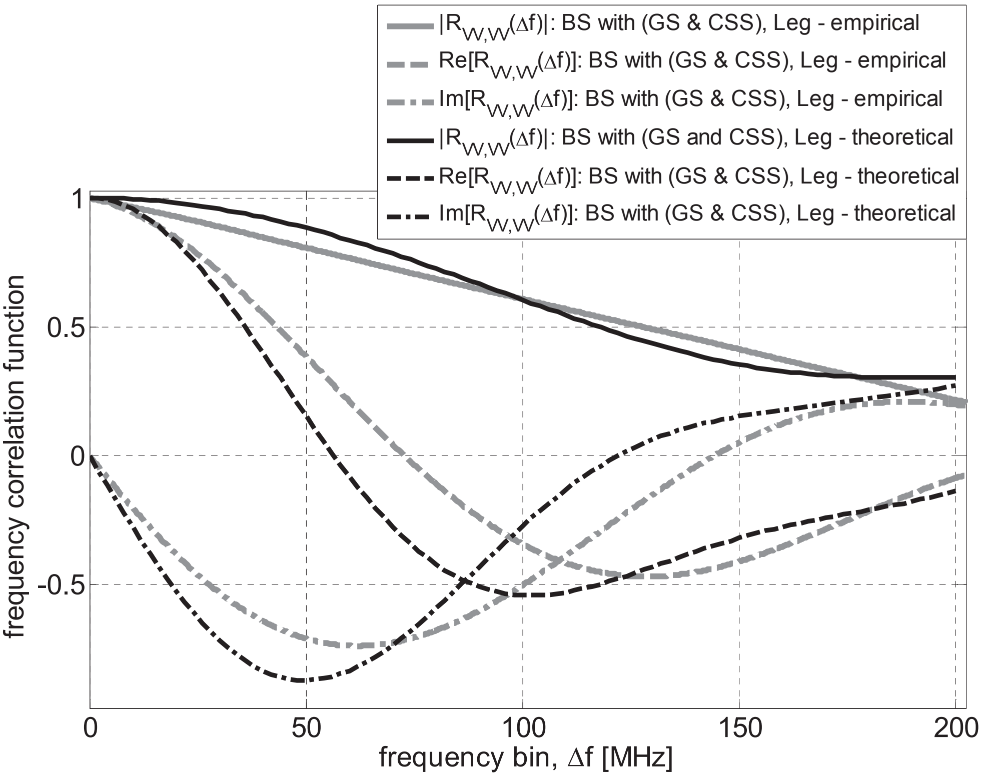

**Figure 23:** Comparison of the theoretical and empirical frequency correlation functions for the VV-channel.

Figures 23 and 24 compare the analytical frequency correlation functions (F-CFs) with the empirical F-CFs for the VV and HV-channels, respectively. In each figure, the magnitude and real/imaginary parts of the analytical and empirical F-CFs are portrayed. The analytical F-CFs, $R^{BAN}_{HV,HV}(\Delta t = 0, \Delta f)$ and $R^{BAN}_{VV,VV}(\Delta t = 0, \Delta f)$, obtained from the proposed BAN channel model are in good agreement with the empirical ones as shown in Figures 23 and 24. The average of difference between the magnitudes of theoretical and empirical F-CFs is only 0.1 in Figure 23, while that average difference is 0.17 in Figure 24. It is worth mentioning that not only $R^{BAN}_{HV,HV}$ but also $R^{BAN}_{VV,VV}$, which is the F-CF of the copolarized channel, is dependent on the

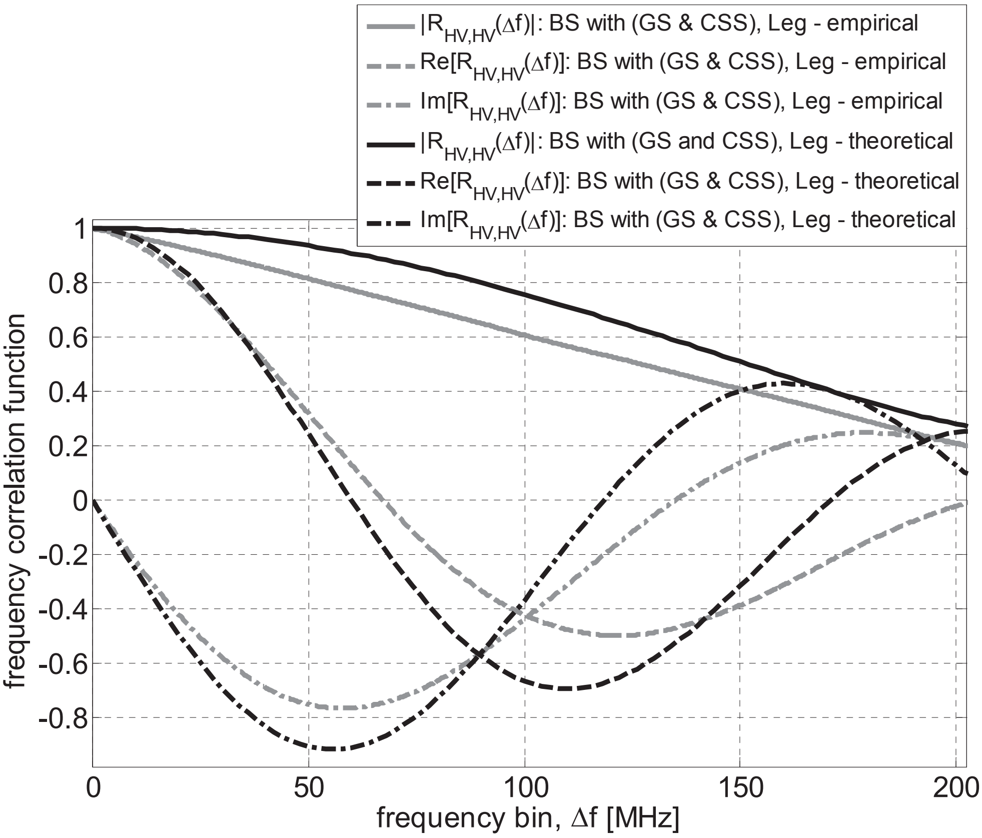

**Figure 24:** Comparison of the theoretical and empirical frequency correlation functions for the HV-channel.

polarization functions derived from the CoP-plane method, since the time-variant transfer function of the VV-channel, $T_{VV}^{BAN}(t, f)$ also depends on the polarization functions for the CSS, GS and BS propagation modes even in the VV-channel.

The impact of the F-CF for each propagation mode on the overall F-CF obtained by superimposing all the propagation modes is interesting since it may reveal a dominant propagation mode in BAN channels, which in turn could lead to further model simplification. The F-CFs of the GS, CSS and BS propagation modes, $R_{VV,VV}^{GS}$, $R_{VV,VV}^{CSS}$ and $R_{VV,VV}^{BS}$, respectively, together with the overall F-CF $R_{VV,VV}^{BAN}$ in the VV-channel are depicted in Figure 25. Observe that the overall F-CF $R_{VV,VV}^{BAN}$ tends to follow the shape and tendency of the F-CF for the GS propagation mode $R_{VV,VV}^{GS}$, while the F-CFs of the CSS and BS propagation modes, $R_{VV,VV}^{CSS}$ and $R_{VV,VV}^{BS}$ are quite different from the overall F-CF $R_{VV,VV}^{BAN}$. From this result, we can conclude that the

GS propagation mode largely dominates the CSS and BS propagation modes in BAN channels at 13 GHz.

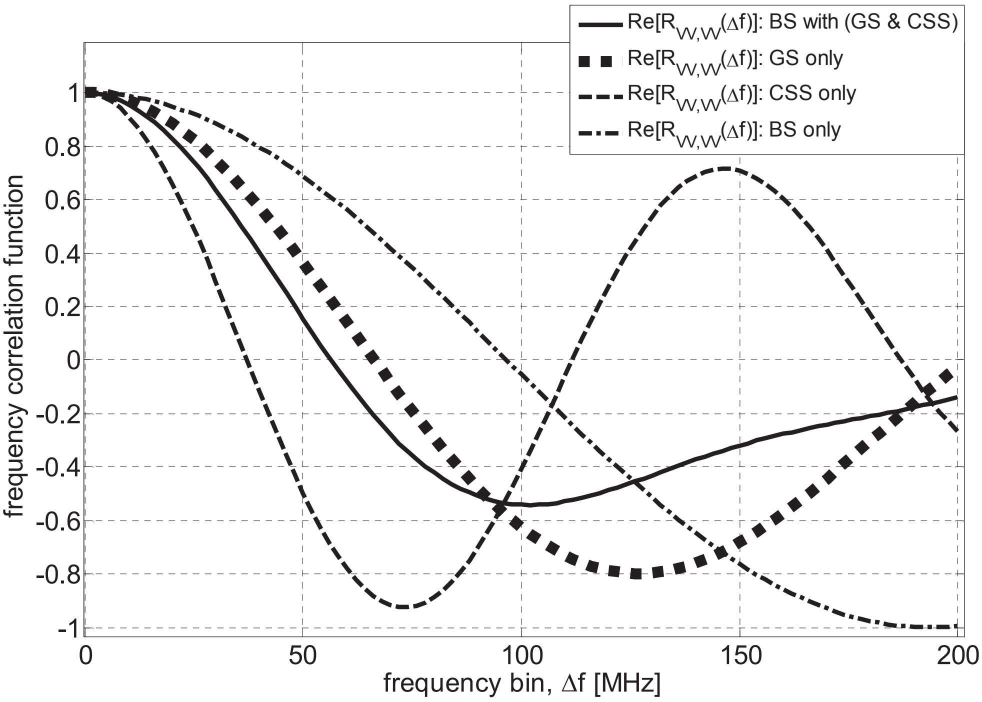

**Figure 25:** Frequency correlation functions for the GS, CSS, BS propagation modes, and the overall frequency correlation function.

Finally, Figure 26 shows some analytically derived XPD results for the GS propagation mode. This figure shows the XPD for each AAoA $\alpha_R$, for various scattering radii, $R_r$. We note that the radius of the scattering ground circle, $R_r$ in the range 0.5 m to 1.5 m is practical [34, 36]. The EAoA $\beta_R$ is determined by the AAoA $\alpha_R$ and the radius of the scattering ground circle, $R_r$ in the GS propagation model as described in Sect. 4.2 with Figure 19. The AAoA $\alpha_R$ is seen to have a significant effect on the XPD in the GS propagation mode. The portion of the XPD curves below or around 0 dB is substantial in the GS propagation mode, particularly, with $R_r = 0.5$ m $\sim$ 1.0 m. This means that the channel depolarization due to the GS wave components can be significant, and we have already shown that the GS propagation mode dominates the overall BAN channel behavior.

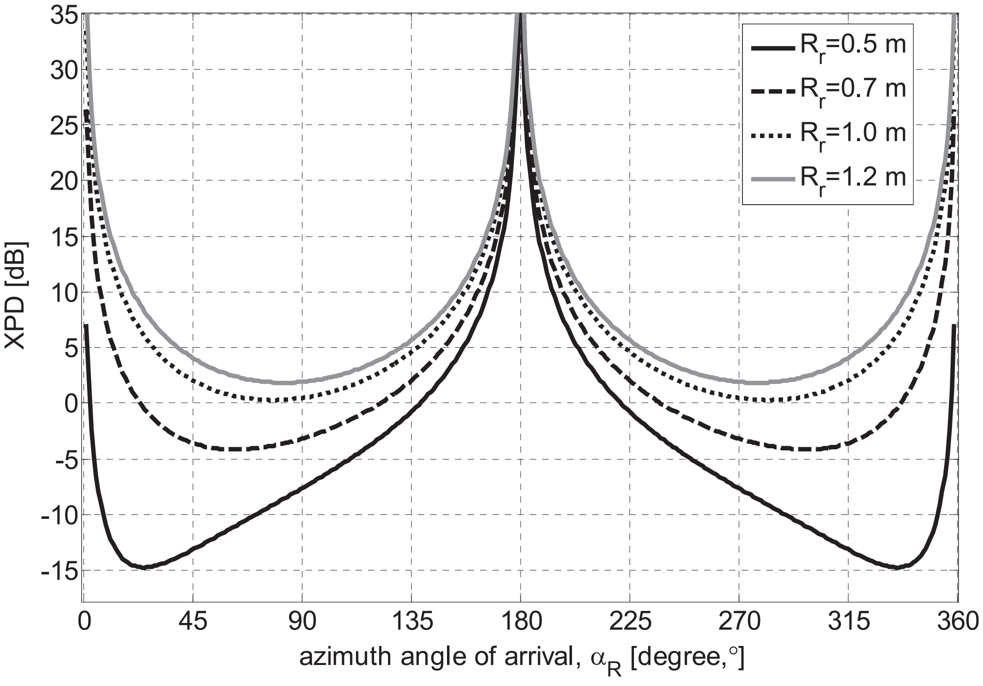

**Figure 26:** $\overline{XPD}^{GS}$ curves for a variety of $R_r$ with each $\alpha_R$.

## *4.5 Summary*

A novel 3-D geometrical model for polarized BAN channels has been proposed in this chapter. The model consists of three propagation components; cylindrical surface scattered (CSS), body scattered (BS), and ground scattered (GS). The effect of the body on the polarized wireless BAN channel, which is mainly composed of creeping wave component and on-body reflecting wave component may be included in an overall BS component based on CSS. Empirical measurements were taken to verify our BAN channel model. To verify our BAN channel model, the analytically derived TF-CF, with appropriate modeling parameters, is compared with the empirically measured TF-CF. The results are in excellent agreement. By using the verified model, the GS propagation component is shown to dominate the CSS and BS modes, in terms of the first order statistics of a polarized BAN channel at 13 GHz. Moreover, channel depolarization due to the GS wave components can be significant.

# CHAPTER V

# POLARIZATION DIVISION MULTIPLE ACCESS ON NLOS WIDE-BAND WIRELESS FADING CHANNELS

A cellular down-link *Polarization Division Multiple Access (PDMA)* scheme with *polarization-filtering detection* and *collaborative transmitter-receiver-polarization adjustment* is proposed for wide-band non-line-of-sight (NLoS) wireless polarized fading channels. The fundamental novelty of the proposed scheme is that it can adjust transmit polarization angles to change the channel impulse response itself and yield a more desirable complex cross-polarization discrimination (XPD) observed at receivers. This is a significant difference between the proposed scheme and the conventional multiple-input multiple-output (MIMO) systems. The capacity analysis of the proposed PDMA scheme is provided, and the feasibility and satisfactory performance of the scheme are demonstrated even when serious time-variant channel depolarization and polarization mismatch between receivers occur. The proposed cellular down-link PDMA scheme uses synchronous orthogonal frequency division multiple access (OFDMA) with an equally spaced pilot symbol allocation and a channel estimator. Excellent symbol error rate (SER)/effective signal-to-interference plus noise ratio (SINR) performance is shown despite the presence of substantial channel depolarization. The scheme can be used to extend the capacity of any cellular system that uses uni-polarized antennas, and can be extended and applied to MIMO arrays as well.

In this chapter, we consider the use of polarization for the purpose of multiplexing or multiple access in cellular land mobile radio systems. We call such a scheme polarization division multiple access (PDMA). Although PDMA can be adapted to any cellular system, we consider cellular systems that use orthogonal frequency division multiple access (OFDMA) such as LTE/LTE-A or WiMax. The forward link is considered in this chapter. The Tx (or base station) has the same structure as a conventional OFDMA base station, except for an antenna that enables Tx-polarization adjustment such as a mounted (colocated) dual-polarization antenna. Two information streams are transmitted by the base station on two orthogonal polarizations. Each Rx (or mobile station) also has a colocated dual-polarization antenna. A feedback mechanism is used to adjust the Tx polarization on each sub-carrier thereby controlling the cross-polarization discrimination (XPD) observed at each Rx. Moreover polarization-filtering detection (PF-detection) is used to recover one or both of the two user data streams at each Rx. The proposed PDMA scheme is verified by using a polarized sum-of-sinusoids channel simulation model generated from [9] in a similar manner with the conventional MIMO channel simulation model in [27]. The PDMA scheme is shown to be feasible even when serious channel depolarization and polarization mismatch between Rx's exist. The main contributions of this research are summarized as follows: 1) a novel cellular down-link PDMA scheme with PF-detection and collaborative Tx-Rx-polarization adjustment, which can optimize channel frequency response and XPD themselves; 2) theoretical analysis for the impact of XPD on the performance of the proposed PDMA scheme in terms of channel capacity; 3) verification of the PDMA scheme's feasibility and satisfactory performance in the OFDMA cellular system with an appropriate pilot symbol allocation scheme; and 4) simulation results showing the relationship between the SER/SINR performance in the proposed PDMA scheme and the Tx-Rx-polarization adjustment.

## 5.1 Polarization Division Multiple Access with PF-detection and Joint Tx-Rx-polarization Adjustment

We assume non line-of-sight (NLoS) wide-band polarized quasi-static fading channels, where the channel is essentially time-invariant over an OFDMA block. The cyclic prefix is assumed longer than the maximum delay of the channel. Both are very common and reasonable assumptions.

### 5.1.1 System Model

The cellular PDMA down-link considered in this chapter is described in Figure 27. The base station (BS) transmits two independent streams, $\{s_1\}$ and $\{s_2\}$ concurrently to mobile stations (MSs), MS-1 and MS-2 via two Tx antennas through the same OFDMA sub-channels. It is assumed that the Tx polarization on each sub-channel is adjustable. In Figure 27, $\mathbf{h}_m^{(\mathrm{v/h}),k}$, $k \in \{1,2\}$, $m \in \{1,2\}$, represents the channel impulse response from the Tx antenna to a vertically/horizontally polarized Rx antenna at MS-$m$. We note that other orientations such as 45° slant arrangements are also possible.

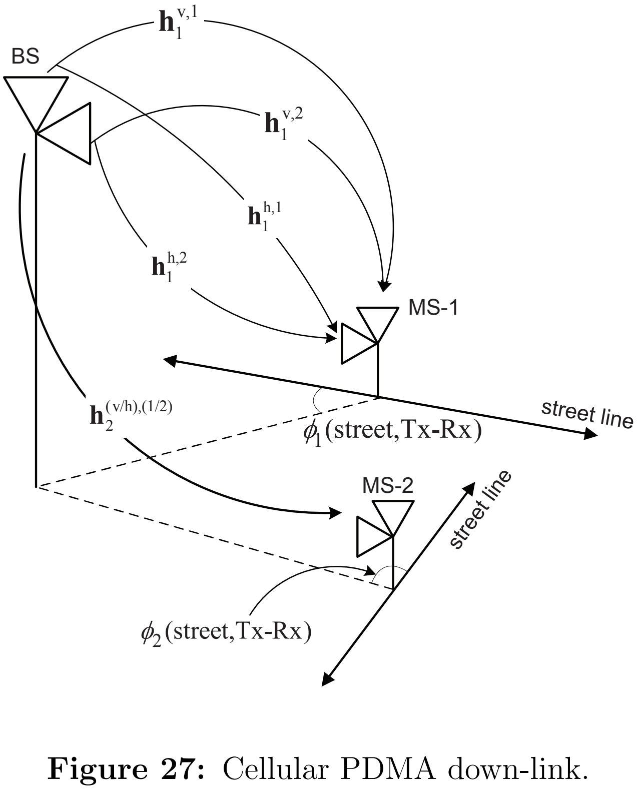

**Figure 27:** Cellular PDMA down-link.

The discrete-time wide-band multi-path fading channels each have $L$-taps and are described by their channel impulse responses $\mathbf{h}_m^{(\mathrm{v/h}),k} = [h_m^{(\mathrm{v/h}),k}(0), ..., h_m^{(\mathrm{v/h}),k}(L-1)]^T$.

Using conventional notation, the $L \times N$ Fourier transform matrix, $\mathbf{F}$ is defined as

$$[\mathbf{F}]_{l,n} = \exp\left(j2\pi\frac{(l-1)(n-1)}{N}\right), \tag{180}$$

where $N$ is the number of sub-channels. For the given $\mathbf{h}_m^{(\mathrm{v/h}),k}$ and $\mathbf{F}$, the channel frequency response of the $n$-th sub-channel at the vertically/horizontally polarized antenna of MS-$m$ is

$$H_{m,n}^{(\mathrm{v/h}),k} = \mathrm{DFT}\left[\mathbf{h}_m^{(\mathrm{v/h}),k}\right] = \mathbf{f}_n^H \mathbf{h}_m^{(\mathrm{v/h}),k}, \tag{181}$$

where $\mathbf{f}_n$ is the $n$-th column of $\mathbf{F}$, and the operator $(\ \cdot\ )^H$ notes complex conjugate transpose.

The Tx has the same structure as a conventional OFDMA down-link Tx except that it has an antenna element that enables per-subcarrier Tx-polarization adjustment such as a mounted (colocated) dual-polarization antenna. The Rx's are assumed to have a colocated dual-polarization antenna with the baseband processing functionality depicted in Figure 28.

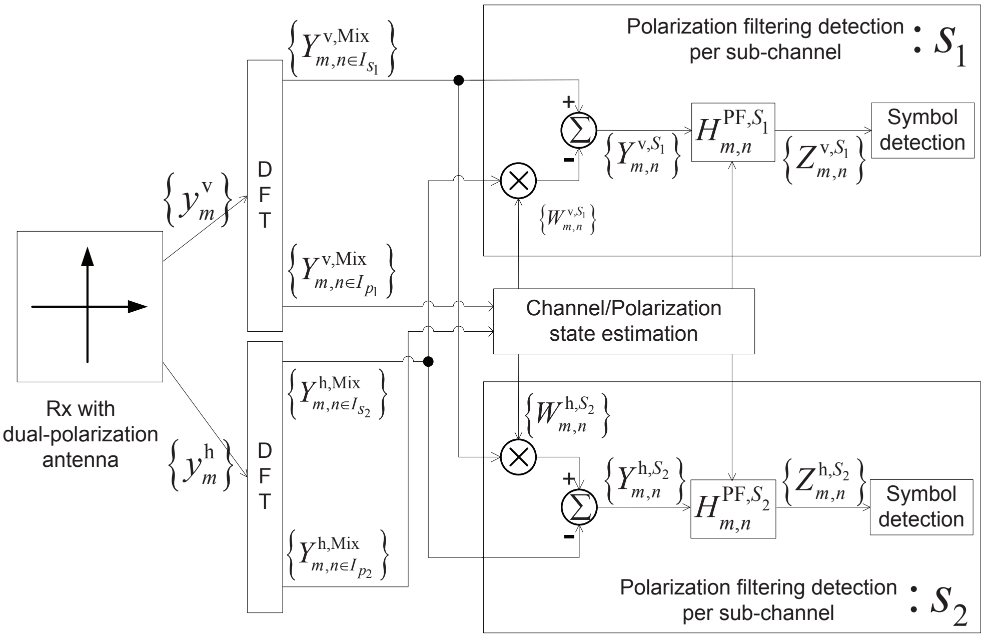

**Figure 28:** PDMA receiver structure for OFDMA-based multi-access.

For the purpose of channel and polarization state estimation, equally spaced pilot symbols are used to minimize the error probability as in [47], appropriately modified to provide polarization state information (PSI). Channel parameters are estimated on a per-block basis, which is particularly appropriate for packet data transmission, where the Rx may receive distinct blocks with unknown delays [47,48]. We note that pilot-symbol-aided inter-block channel/polarization state estimation may be possible [49] as well, but is not pursued further here.

First, after demodulation and discrete fourier transformation (DFT) at the Rx, the received signals corresponding to pilot symbols on the $n$-th OFDM sub-channel at the vertically and horizontally polarized antennas of MS-$m$, $Y^{\mathrm{v,Mix}}_{m,n}$ and $Y^{\mathrm{h,Mix}}_{m,n}$, respectively, are

$$Y^{\mathrm{v,Mix}}_{m,n} = \sqrt{E_{p,1}}H^{\mathrm{v},1}_{m,n}s_1(n) + \sqrt{E_{p,2}}H^{\mathrm{v},2}_{m,n}s_2(n) + w^{\mathrm{v}}_{m,n}\ ,\ n \in I_{p,1}, \tag{182}$$

$$Y^{\mathrm{h,Mix}}_{m,n} = \sqrt{E_{p,1}}H^{\mathrm{h},1}_{m,n}s_1(n) + \sqrt{E_{p,2}}H^{\mathrm{h},2}_{m,n}s_2(n) + w^{\mathrm{h}}_{m,n}\ ,\ n \in I_{p,2}, \tag{183}$$

where $s_k(n)$, $H^{(\mathrm{v/h}),k}_{m,n}$ and $E_{p,k}$ such that $k \in \{1,2\}$ and $n \in I_{p,k}$ are, respectively, the pilot symbol, channel frequency response at the vertically/horizontally polarized Rx antenna of MS-$m$, and transmitted pilot symbol power for the stream $\{s_k\}$. Further, $I_{p,k}$, $k \in \{1,2\}$ is the set of pilot symbols for $\{s_k\}$ in an OFDM block, and $w^{\mathrm{v/h}}_{m,n}$ is complex additive white Gaussian noise (AWGN) with zero mean and variance $N_o/2$ for both the real and imaginary parts. In the same manner, the received signals corresponding to information symbols, $Y^{\mathrm{v,Mix}}_{m,n}$ and $Y^{\mathrm{h,Mix}}_{m,n}$ at the vertically and horizontally polarized antennas of MS-$m$, respectively, are

$$Y^{\mathrm{v,Mix}}_{m,n} = \sqrt{E_{s,1}}H^{\mathrm{v},1}_{m,n}s_1(n) + \sqrt{E_{s,2}}H^{\mathrm{v},2}_{m,n}s_2(n) + w^{\mathrm{v}}_{m,n}\ ,\ n \in I_{s,1}, \tag{184}$$

$$Y^{\mathrm{h,Mix}}_{m,n} = \sqrt{E_{s,1}}H^{\mathrm{h},1}_{m,n}s_1(n) + \sqrt{E_{s,2}}H^{\mathrm{h},2}_{m,n}s_2(n) + w^{\mathrm{h}}_{m,n}\ ,\ n \in I_{s,2}, \tag{185}$$

where $E_{s,k}$ and $I_{s,k}$, $k \in \{1,2\}$ are, respectively, the transmitted information symbol power and the set of information symbols in the OFDM block. It is assumed that the total number of sub-channels is $N$, and further, $|I_{p,1}| = |I_{p,2}| = P$ and $|I_{s,1}| = |I_{s,2}| = N - 2P$. Equally spaced pilot symbols are used in each OFDM block, which is optimal for minimizing error probability [47]. i.e.,

$$I_{p,1} = \left\{ j_{p,1} + k\frac{N}{P} \text{ s.t. k} \in [0, \text{P} - 1] \right\}, \tag{186}$$

$$I_{p,2} = \left\{ j_{p,2} + k\frac{N}{P} \text{ s.t. k} \in [0, \text{P} - 1] \right\}, \tag{187}$$

$$j_{p,1} \in \left[ 0, \frac{N}{P} - 1 \right], \; j_{p,2} \in \left[ 0, \frac{N}{P} - 1 \right], \; j_{p,1} \neq j_{p,2}. \tag{188}$$

Furthermore, to achieve satisfactory channel/polarization state estimation in the PDMA channels, the subcarriers assigned as pilot symbols in the OFDM block of MS-2, are assigned as null subcarriers in the OFDM block of MS-1, and vice versa, i.e., $s_1(n \in I_{p,2}) = 0$, and $s_2(n \in I_{p,1}) = 0$, which implies,

$$I_s = I_{s,1} = I_{s,2} = I - (I_{p,1} \cup I_{p,2}), \tag{189}$$

where $I$ is the entire set of the subcarriers in an OFDM block. Notice that MS-1 and MS-2 use the same subcarriers for information symbols at the same time, while pilot symbols for MS-1 and MS-2 are assigned orthogonal subcarriers. The aforementioned pilot symbol allocation scheme is utilized in our simulations to show the feasibility of the proposed PDMA scheme. Even though the analysis of channel estimation error depending on the pilot symbol allocation scheme and estimation method is beyond the scope of the issues in this thesis, the thorough analysis is provided in [47].

Further, in the simulation, least-square error (LSE) channel estimation is utilized, which yields a symbol error rate (SER) performance identical to that of the minimum mean-square error (MMSE) channel estimator when the pilot symbols are equally spaced, and the channel taps are independent and identically distributed (i.i.d.) [47].

### 5.1.2 Polarization-Filtering Detection with the Appropriate XPD

The proposed PDMA scheme utilizes per-subcarrier PF-detection to recover the user data streams that have undergone substantial channel depolarization. Perfect Rx symbol synchronization is assumed which is the case for the cellular OFDMA downlink. Polarization state information (PSI) is required to perform the PF-detection and, in turn, the PSI can be estimated along with CSI.

Channel depolarization can be described by the conventional ensemble (fading) averaged channel cross-polarization discrimination (XPD), defined as the ratio of the copolarized signal's average received power to the cross-polarized signal's average received power. In this section, we also define the *complex XPD* as the ratio of the channel frequency responses at the vertically and horizontally polarized Rx antennas, or whatever other polarization is applied at the Rx. i.e.,

$$\widetilde{\mathrm{XPD}}_{m,n}^{\mathrm{vh},k} \triangleq \frac{H_{m,n}^{\mathrm{v},k}}{H_{m,n}^{\mathrm{h},k}},\ k \in \{1,2\},\ m \in \{1,2\}, \tag{190}$$

where once again, $k$, $m$ and $n$ are, respectively, the stream, MS and sub-channel indices.

Assume the BS transmits two user data streams, $\{s_1\}$ and $\{s_2\}$, via vertically and horizontally polarized antennas, respectively. The channel exhibits depolarization. If the signals received on the vertically and horizontally polarized Rx antennas of MS-$m$ are used to detect $s_1(n)$ and $s_2(n)$, $n \in I_s$, respectively, then the corresponding outputs of the matched filters $Z_{m,n}^{\mathrm{v},s_1\prime}$ and $Z_{m,n}^{\mathrm{h},s_2\prime}$ are, respectively,

$$\begin{aligned} Z_{m,n}^{\mathrm{v},s_1\prime} &= (\hat{H}_{m,n}^{\mathrm{v},1})^* \, Y_{m,n}^{\mathrm{v,Mix}} && (191)\\ &= \sqrt{E_{s,1}}(\hat{H}_{m,n}^{\mathrm{v},1})^* H_{m,n}^{\mathrm{v},1} s_1(n) + \sqrt{E_{s,2}}(\hat{H}_{m,n}^{\mathrm{v},1})^* H_{m,n}^{\mathrm{v},2} s_2(n) + (\hat{H}_{m,n}^{\mathrm{v},1})^* w_{m,n}^{\mathrm{v}}\ , \\ Z_{m,n}^{\mathrm{h},s_2\prime} &= (\hat{H}_{m,n}^{\mathrm{h},2})^* \, Y_{m,n}^{\mathrm{h,Mix}} && (192)\\ &= \sqrt{E_{s,2}}(\hat{H}_{m,n}^{\mathrm{h},2})^* H_{m,n}^{\mathrm{h},2} s_2(n) + \sqrt{E_{s,1}}(\hat{H}_{m,n}^{\mathrm{h},2})^* H_{m,n}^{\mathrm{h},1} s_1(n) + (\hat{H}_{m,n}^{\mathrm{h},2})^* w_{m,n}^{\mathrm{h}}\ , \end{aligned}$$

where $\hat{H}_{m,n}^{\mathrm{v},1}$ and $\hat{H}_{m,n}^{\mathrm{h},2}$ are the estimated channel frequency responses for $H_{m,n}^{\mathrm{v}-1}$ and $H_{m,n}^{\mathrm{h},2}$, respectively. From here on, only the information symbols are considered.

In the ideal case of the perfect channel estimation, i.e., $\hat{H}_{m,n}^{\mathrm{v},1} = H_{m,n}^{\mathrm{v},1}$ and $\hat{H}_{m,n}^{\mathrm{h},2} = H_{m,n}^{\mathrm{h},2}$, the instantaneous SINR values at the matched filter outputs $Z_{m,n}^{\mathrm{v},s_1\prime}$ and $Z_{m,n}^{\mathrm{h},s_2\prime}$

are

$$\gamma\left(Z^{\mathrm{v},s_1\prime}_{m,n}\right) = \frac{E_{s,1}\left|H^{\mathrm{v},1}_{m,n}\right|^2}{E_{s,2}\left|H^{\mathrm{v},2}_{m,n}\right|^2+N_o}\ , \tag{193}$$

$$\gamma\left(Z^{\mathrm{h},s_2\prime}_{m,n}\right) = \frac{E_{s,2}\left|H^{\mathrm{h},2}_{m,n}\right|^2}{E_{s,1}\left|H^{\mathrm{h},1}_{m,n}\right|^2+N_o}\ , \tag{194}$$

where it is assumed $|s_1(n)| = |s_2(n)| = 1$, which holds for all the remaining parts of this chapter unless otherwise stated.

The SINR can be improved via suppressing or filtering out the second terms in (191) and (192), $\sqrt{E_{s,2}}(\hat{H}^{\mathrm{v},1}_{m,n})^* H^{\mathrm{v},2}_{m,n} s_2(n)$ and $\sqrt{E_{s,1}}(\hat{H}^{\mathrm{h},2}_{m,n})^* H^{\mathrm{h},1}_{m,n} s_1(n)$, respectively, which are the cross-polarization components of the interfering signals. In Figure 28, the upper stage detects $s_1(n)$ and the lower stage detects $s_2(n)$. Each MS utilizes either the upper stage or lower stage as appropriate to detect its desired symbols, i.e., MS-1/MS-2 detects $s_1(n)/s_2(n)$ from the upper/lower stage in Figure 28. Further, the MS can also use both stages to detect both $s_1(n)$ and $s_2(n)$ in the case of polarization division multiplexing where both streams are intended for the same user. Notice that the PF-detection is performed on a per-subcarrier basis.

Using the complex XPD state estimates, the PF-weights in the upper and lower stages in Figure 28 are chosen as

$$W^{\mathrm{v},s_1}_{m,n} = \widehat{\mathrm{XPD}}^{\mathrm{vh},2}_{m,n} = \frac{\hat{H}^{\mathrm{v},2}_{m,n}}{\hat{H}^{\mathrm{h},2}_{m,n}}\ , \tag{195}$$

$$W^{\mathrm{h},s_2}_{m,n} = \left(\widehat{\mathrm{XPD}}^{\mathrm{vh},1}_{m,n}\right)^{-1} = \frac{\hat{H}^{\mathrm{h},1}_{m,n}}{\hat{H}^{\mathrm{v},1}_{m,n}}\ . \tag{196}$$

Then, the intermediate signals $Y^{\mathrm{v},s_1}_{m,n}$ and $Y^{\mathrm{h},s_2}_{m,n}$ in Figure 28 are

$$\begin{aligned} Y^{\mathrm{v},s_1}_{m,n} &= Y^{\mathrm{v,Mix}}_{m,n} - W^{\mathrm{v},s_1}_{m,n} Y^{\mathrm{h,Mix}}_{m,n} \\ &= \sqrt{E_{s,1}}\left(H^{\mathrm{v},1}_{m,n} - W^{\mathrm{v},s_1}_{m,n} H^{\mathrm{h},1}_{m,n}\right) s_1(n) + \sqrt{E_{s,2}}\left(H^{\mathrm{v},2}_{m,n} - W^{\mathrm{v},s_1}_{m,n} H^{\mathrm{h},2}_{m,n}\right) s_2(n) \\ &\quad + \left(w^{\mathrm{v}}_{m,n} - W^{\mathrm{v},s_1}_{m,n} w^{\mathrm{h}}_{m,n}\right), \end{aligned} \tag{197}$$

$$\begin{aligned} Y^{\mathrm{h},s_2}_{m,n} &= Y^{\mathrm{h,Mix}}_{m,n} - W^{\mathrm{v},s_1}_{m,n} Y^{\mathrm{v,Mix}}_{m,n} \\ &= \sqrt{E_{s,2}} \left( H^{\mathrm{h},2}_{m,n} - W^{\mathrm{h},s_2}_{m,n} H^{\mathrm{v},2}_{m,n} \right) s_2(n) + \sqrt{E_{s,1}} \left( H^{\mathrm{h},1}_{m,n} - W^{\mathrm{h},s_2}_{m,n} H^{\mathrm{v},1}_{m,n} \right) s_1(n) \\ &\quad + \left( w^{\mathrm{h}}_{m,n} - W^{\mathrm{h},s_2}_{m,n} w^{\mathrm{v}}_{m,n} \right). \end{aligned} \tag{198}$$

If perfect channel/polarization state estimation is assumed, then the second terms in (197) and (198) are completely filtered out. Further, based on the first terms in (197) and (198), the matched filters required for PF-detection, $H^{\mathrm{PF},s_1}_{m,n}$ and $H^{\mathrm{PF},s_2}_{m,n}$ can be obtained from the channel estimates as follows:

$$\begin{aligned} H^{\mathrm{PF},s_1}_{m,n} &= \left( \hat{H}^{\mathrm{v},1}_{m,n} - W^{\mathrm{v},s_1}_{m,n} \hat{H}^{\mathrm{h},1}_{m,n} \right)^*, \\ H^{\mathrm{PF},s_2}_{m,n} &= \left( \hat{H}^{\mathrm{h},2}_{m,n} - W^{\mathrm{v},s_2}_{m,n} \hat{H}^{\mathrm{v},2}_{m,n} \right)^*. \end{aligned} \tag{199}$$

The outputs of the PF-detection matched filters are

$$\begin{aligned} Z^{\mathrm{v},s_1}_{m,n} &= H^{\mathrm{PF},s_1}_{m,n}\ Y^{\mathrm{v},s_1}_{m,n} & (200) \\ &= \sqrt{E_{s,1}} H^{\mathrm{PF},s_1}_{m,n} \left( H^{\mathrm{v},1}_{m,n} - W^{\mathrm{v},s_1}_{m,n} H^{\mathrm{h},1}_{m,n} \right) s_1(n) + H^{\mathrm{PF},s_1}_{m,n} \left( w^{\mathrm{v}}_{m,n} - W^{v,s_1}_{m,n} w^{\mathrm{h}}_{m,n} \right), \\ Z^{\mathrm{h},s_2}_{m,n} &= H^{\mathrm{PF},s_2}_{m,n}\ Y^{\mathrm{h},s_2}_{m,n} & (201) \\ &= \sqrt{E_{s,2}} H^{\mathrm{PF},s_2}_{m,n} \left( H^{\mathrm{h},2}_{m,n} - W^{\mathrm{h},s_2}_{m,n} H^{\mathrm{v},2}_{m,n} \right) s_2(n) + H^{\mathrm{PF},s_2}_{m,n} \left( w^{\mathrm{h}}_{m,n} - W^{\mathrm{h},s_2}_{m,n} w^{\mathrm{v}}_{m,n} \right). \end{aligned}$$

The SINRs at the PF-detection matched filter output, $\gamma\left(Z^{\mathrm{v},s_1}_{m,n}\right)$ and $\gamma\left(Z^{\mathrm{h},s_2}_{m,n}\right)$, are expressed as (202) and (203).

It is worth mentioning that the polarization filtering affects signal-to-noise ratio (SNR) in either a constructive or destructive fashion. This is apparent since both the numerator and denominator in (202) – (203) depend on the PF-weights, $W^{\mathrm{v},s_1}_{m,n}$ and $W^{\mathrm{h},s_2}_{m,n}$. The novelty of the proposed PDMA scheme, which is quite different from the conventional MIMO techniques, is that it can adjust Tx-polarization angles to change the channel impulse response itself and yield a more desirable complex XPD observed at the receivers. That is, we not only determine the weights of the polarization filter (PF-weights), $W^{\mathrm{v},s_1}_{m,n}$ and $W^{\mathrm{h},s_2}_{m,n}$ in Figure 28 based on the estimated complex XPD,

$$\begin{aligned}\gamma\left(Z^{\mathrm{v},s_1}_{m,n}\right) &= \frac{E_{s,1}|H^{\mathrm{PF},s_1}_{m,n}|^2}{\left(1+|W^{\mathrm{v},s_1}_{m,n}|^2\right)N_o} \\ &= \frac{E_{s,1}\left(\left|H^{\mathrm{v},1}_{m,n}\right|^2+\left|H^{\mathrm{h},1}_{m,n}\right|^2\left|W^{\mathrm{v},s_1}_{m,n}\right|^2-2\mathrm{Re}\left[\left(H^{\mathrm{v},1}_{m,n}\right)^*H^{\mathrm{h},1}_{m,n}W^{\mathrm{v},s_1}_{m,n}\right]\right)}{\left(1+|W^{\mathrm{v},s_1}_{m,n}|^2\right)N_o},\end{aligned}\tag{202}$$

$$\begin{aligned}\gamma\left(Z^{\mathrm{h},s_2}_{m,n}\right) &= \frac{E_{s,2}|H^{\mathrm{PF},s_2}_{m,n}|^2}{\left(1+|W^{\mathrm{h},s_2}_{m,n}|^2\right)N_o} \\ &= \frac{E_{s,1}\left(\left|H^{\mathrm{h},2}_{m,n}\right|^2+\left|H^{\mathrm{v},2}_{m,n}\right|^2\left|W^{\mathrm{h},s_2}_{m,n}\right|^2-2\mathrm{Re}\left[\left(H^{\mathrm{h},2}_{m,n}\right)^*H^{\mathrm{v},2}_{m,n}W^{\mathrm{h},s_2}_{m,n}\right]\right)}{\left(1+\left|W^{\mathrm{h},s_2}_{m,n}\right|^2\right)N_o},\end{aligned}\tag{203}$$

---

but also utilize Tx-polarization adjustment scheme to yield more desirable complex XPD itself at the Rx for the higher channel capacity. The PF-weight is the function of XPD, and in turn, XPD is the function of channel frequency responses expressed in (181). We emphasize that it is the originality of the proposed PDMA scheme that the Tx can adjust complex XPD itself, by tuning Tx-polarization angles at the BS such that the MS has more desirable XPD. On the other hand, conventional MIMO system usually utilizes the power control/allocation algorithm for a given channel impulse response, i.e., the Tx cannot change channel impulse response itself to be the more desirable one at the Rx, although we know the better channel condition to reach the higher channel capacity. It is a significant difference between conventional MIMO techniques and our PDMA scheme, and it substantially affects the system performance in terms of channel capacity as will be shown in the sequel.

Before we derive the channel capacity of the proposed PDMA scheme, we consider two ideal scenarios of adjusting PF-weights as

1. balanced-XPD scheme:

$$\mathrm{E}\left[\left|W_{m,n}^{\mathrm{v},s_1}\right|^2\right] = \mathrm{E}\left[\left|\ \widetilde{\mathrm{XPD}}_{m,n}^{\mathrm{vh},2}\ \right|^2\right] = 1, \tag{204}$$

$$\mathrm{E}\left[\left|\ W_{m,n}^{\mathrm{h},s_2}\ \right|^2\right] = \mathrm{E}\left[\left|\left(\widetilde{\mathrm{XPD}}_{m,n}^{\mathrm{vh},1}\right)^{-1}\right|^2\right] = 1; \tag{205}$$

2. infinite-XPD scheme:

$$\mathrm{E}\left[\left|W_{m,n}^{\mathrm{v},s_1}\right|^2\right] = \mathrm{E}\left[\left|\ \widetilde{\mathrm{XPD}}_{m,n}^{\mathrm{vh},2}\ \right|^2\right] = 0, \tag{206}$$

$$\mathrm{E}\left[\left|\ W_{m,n}^{\mathrm{h},s_2}\ \right|^2\right] = \mathrm{E}\left[\left|\left(\widetilde{\mathrm{XPD}}_{m,n}^{\mathrm{vh},1}\right)^{-1}\right|^2\right] = 0. \tag{207}$$

In infinite-XPD scheme, note that $\mathrm{E}[|(\widetilde{\mathrm{XPD}}_{m,n}^{\mathrm{vh},1})|^2] = \infty$ dB, and $\mathrm{E}[|(\widetilde{\mathrm{XPD}}_{m,n}^{\mathrm{vh},2})|^2] = -\infty$ dB. The more detailed description and the algorithm of adjusting XPD will be provided in Sections 5.1.3 and 5.1.4. First, considering balanced-XPD scheme, the channel capacity of the stream-1 at MS-1 in the PDMA channel can be expressed as

$$\begin{aligned}
\mathbf{C}_{\mathrm{ave}}^{\mathrm{PF,s_1}} &= \mathrm{E}\left[\log\left(1+\gamma\left(\mathrm{Z}_{\mathrm{m,n}}^{\mathrm{v,s_1}}\right)\right)\right] \\
&\le \log\left(1+\mathrm{E}\left[\gamma\left(\mathrm{Z}_{\mathrm{m,n}}^{\mathrm{v,s_1}}\right)\right]\ \right) \\
&= \log\left(1+\frac{E_{s,1}\left(\mathrm{E}\left[\left|H_{m,n}^{\mathrm{v},1}\right|^2+\left|H_{m,n}^{\mathrm{h},1}\right|^2\left|W_{m,n}^{\mathrm{v},s_1}\right|^2\right]\right)}{\left(1+\mathrm{E}\left[\left|W_{m,n}^{\mathrm{v},s_1}\right|^2\right]\right)N_o}\right) \\
&= \log\left(1+\frac{E_{s,1}\left(\mathrm{E}\left[\left|H_{m,n}^{\mathrm{v},1}\right|^2\right]+\mathrm{E}\left[\left|H_{m,n}^{\mathrm{h},1}\right|^2\right]\right)}{2N_o}\right) \\
&= \log\left(1+\frac{E_{s,1}\left(\mathrm{E}\left[\left|H_{m,n}^{\mathrm{v},1}\right|^2\right]\right)}{N_o}\right),
\end{aligned} \tag{208}$$

where Jensen's inequality is utilized, and $\mathrm{E}\left[\ |W_{m,n}^{\mathrm{v},s_1}|^2\ \right]$ and $\mathrm{E}\left[\ |W_{m,n}^{\mathrm{h},s_2}|^2\ \right]$ are set to unity in the linear scale corresponding to the condition of the balanced-XPD scheme in (204) – (205). $\mathrm{E}\left[\ |W_{m,n}^{\mathrm{v},s_1}|^2\ \right] = \mathrm{E}[\ |\widehat{\mathrm{XPD}}_{m,n}^{\mathrm{vh},2}|^2\ ]$ follows the conventional V-H XPD in a statistical sense. It is worth mentioning that the expression at the last line of (208) corresponds to the channel capacity of the single-stream scenario where vertically polarized Tx antenna transmits stream-1 to the vertically polarized Rx antenna at MS-1 with the same symbol power. In the same manner as $\mathbf{C}_{\text{ave}}^{\text{PF,s}_1}$,

$$\begin{aligned}\mathbf{C}_{\text{ave}}^{\text{PF,s}_2} &= \mathrm{E}\left[\log\left(1+\gamma\left(\mathrm{Z}_{\text{m,n}}^{\text{v,s}_2}\right)\right)\right] \\ &\leq \log\left(1+\frac{E_{s,2}\left(\mathrm{E}\left[\left|H_{m,n}^{\text{h},2}\right|^2\right]\right)}{N_o}\right). \end{aligned} \tag{209}$$

Note that, the conventional MIMO system does not utilize Tx-polarization adjustment scheme. Hence, we cannot adjust E[ $|H_{m,n}^{\text{v},1}|^2$ ] and E[$|H_{m,n}^{\text{h},1}|^2$]; E[ $|H_{m,n}^{\text{v},2}|^2$ ] and E[ $|H_{m,n}^{\text{h},2}|^2$ ]; thus, E[ $|W_{m,n}^{\text{v},s_1}|^2$ ] and E[ $|W_{m,n}^{\text{v},s_2}|^2$ ] in (208).

In case of the infinite-XPD scheme, the channel capacity is derived to the same conclusion, i.e., the last line in (208) or (209) by utilizing (206) – (207) instead of (204) – (205) . However, we focus on the balanced-XPD scheme, since it is practically impossible for the MS to have ±∞ dB XPD as implied in [9].

### 5.1.3 Tx-polarization Adjustment

It is necessary to understand the behaviour of channel depolarization if a satisfactory level of SER performance can be obtained by PF-detection. The ensemble averaged V-H XPD vs. distance is plotted in Figure 29, where the geometry of the Tx, Rx and scatterers varies with the angle between the Tx–Rx boresight line and the street line, $\phi(\text{street}, \text{Tx} - \text{Rx})$ in Figure 27; a variety of Tx antenna polarizations are used. The Rx is assumed to maintain vertically and horizontally polarized antenna elements without the loss of generality, as described in detail in Section 5.1.4.

The V-H XPD curves in Figure 29 are generated using our earlier polarized channel model in [9]. The necessary modeling parameters are included in the figure caption. $h_T$, $h_R$, $D$, and $R_r$, are, respectively, the height of the Tx and the Rx, the horizontal distance between the Tx and Rx, the radius of the scattering cylinder whose center at the horizontal plane is the Rx. Further, $\mu_R$, $k_R$ and $\beta_{R,Max}$ are, respectively, the mean azimuth angle of arrival (AAoA), the azimuth angular spread constant, and the

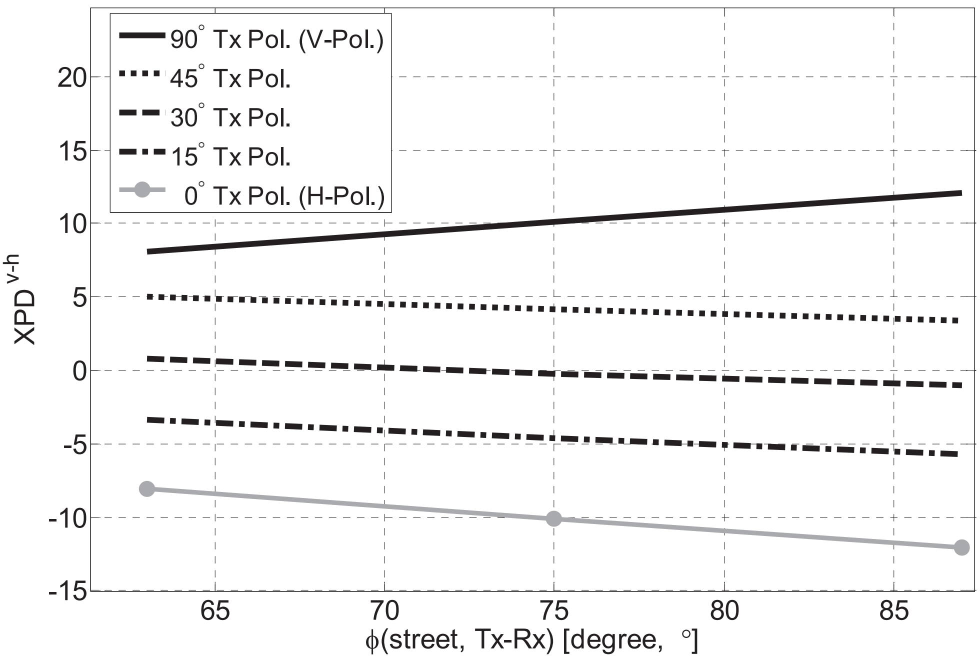

**Figure 29:** XPD curves according to the Tx-Rx line and street line geometry with a variety of Tx-polarization angles; $\mu_R = 180° - \phi(\mathrm{street}, \mathrm{Tx} - \mathrm{Rx})$, $k_R = 20$, $\beta_{R,Max} = 30°$, $R_r = 10 - 200$ m, $h_T = 35$ m, $h_R = 1.65$ m, $D = 1$ km, propagation path loss exponent $n = 3.5$.

maximum elevation angle of arrival (EAoA). Essentially, channel impulse responses for Figure 29 and Section 5.2 are generated from the combination of the narrow-band polarized fading channel model in [9] and the wide-band uni-polarized MIMO channel model in [27]. Notice that the XPD at $\phi(\mathrm{street}, \mathrm{Tx} - \mathrm{Rx}) = 87°$ varies substantially from -12 dB to 12 dB as the Tx antenna changes its polarization from horizontal to vertical.

The XPD observed at the Rx can be controlled at the Tx by adjusting the Tx polarization according to PSI measurements at the Rx along with a feedback channel. Since the XPD is averaged over the channel fading, it is a relatively slowly changing parameter, and the amount of PSI feedback control data is not expected to be large.

The processing used to recover $s_1(n)$ excises the interference $s_2(n)$ and vice versa, but the outputs of the PF-detection matched filters, $Z_{m,n}^{\mathrm{v},s_1}$ and $Z_{m,n}^{\mathrm{h},s_2}$ in (200) and (201), are still largely dependent on the weighted noise terms. To achieve better SER performance, the XPD observed at the receiver can be controlled by adjusting the Tx polarization. That is, the Tx-polarization adjustment can vary the XPD observed at the Rx as described in Figure 29, and the complex XPD observed at the Rx, $H^{\mathrm{v},1}_{m,n}/H^{\mathrm{h},1}_{m,n}$ and $H^{\mathrm{v},2}_{m,n}/H^{\mathrm{h},2}_{m,n}$ will, in turn, follow the XPD in a statistical sense.

Under the assumption that a feedback channel exists between the Tx and Rx such that Tx-polarization adjustment can control the V-H XPD at the Rx, balanced-XPD and infinite-XPD schemes can be considered as mentioned in Section 5.1.2. The balanced-XPD scheme adjusts the Tx polarization to yield zero dB V-H XPD at the Rx. This scheme causes the signal sent from a Tx to be received with the same power in the vertically and horizontally polarized channels, respectively, in (184) and (185). Further, in this scheme, the SNR of each signal at the post-PF stage in (197) or (198) remains same as that of the pre-PF stage in (184) or (185) if the vertically and horizontally polarized channels are uncorrelated.

The infinite-XPD scheme adjusts the Tx-polarization of each Tx such that the power of the cross-polarization components is minimized. For example, the ideal scenario in (184) and (185) occurs when the V-H XPD of $s_1(n)$ is positive infinity and the V-H XPD of $s_2(n)$ is negative infinity. However, infinite XPD is not practical because the wireless channel will depolarize [9]. Hence, the maximum V-H XPD for $s_1(n)$ and the minimum V-H XPD for $s_2(n)$ are pursued instead of positive and negative infinity, respectively. In this scheme, the effect of the additional weighted noise is regarded as insignificant since the weights in (195) and (196) have small amplitudes. Furthermore, the remaining power of the interfering signal at the post-PF stage is negligible, although that signal is not perfectly filtered out; therefore, the infinite-XPD scheme may be less sensitive to channel/polarization state estimation error than the balanced-XPD scheme.

In this thesis, we focus on the balanced-XPD scheme since it is a practical one. The optimal Tx-polarization angles for the balanced-XPD scheme are $30^\circ$ and $30^\circ + 90^\circ =$

120° for the given scenario in Figure 29. When the Tx-polarization angle is 120°, which is orthogonal to 30° Tx-polarization, the V-H XPD curve is almost same as that for the 30° Tx-polarization; therefore, the former is omitted in Figure 29. Notice that the aforementioned optimal Tx-polarization angles vary depending on the given scenario in terms of the surroundings in the vicinity of the MS including the angle between the street line and Tx–Rx boresight line. For this reason, Tx-polarization adjustment through the feedback channel is essential in the proposed PDMA scheme. The PSI in terms of XPD, which is relayed from the Rx to the Tx via the feedback channel, is exploited at the BS for optimal Rx-polarization estimation and then, Tx-polarization adjustment as will be described in detail in Section 5.1.4 with the summarization in Table 1.

### 5.1.4 Collaborative Scheme of Iterative Tx-Rx-polarization Adjustment

In this section, a collaborative scheme of optimal Tx-Rx-polarization estimation to iteratively adjust Tx polarization, thus, in turn, Rx polarization is proposed. The scheme exhibits satisfactory SER performance for the down-link PDMA channels even when the Rx-polarization at each MS has serious mismatch with that of other MS. The SER performance in this scenario will be described in detail in Section 5.2.2.

The Rx-polarization mismatch is created by two factors: different environments depending on the location of each MS and the rotation of Rx antenna orientation owing to the rotational movement of the MS. The scenario of the Rx antenna rotation by a given azimuth and elevation angle pair $(\alpha_A, \beta_A)$ can be regarded as the equivalent scenario of the environment rotation by $(-\alpha_A, -\beta_A)$. Hence, the Rx antenna rotation is equivalent to a change of the scattering environment around the MS. In any case, the maximum mismatch of Rx-polarization between two MSs is 45°, since each MS with a dual-polarization antenna has a Rx-polarization angle pair, $(\theta_{\mathrm{Rx}}, \theta_{\mathrm{Rx}} + \frac{\pi}{2})$ such that $0 \leq \theta_{\mathrm{Rx}} \leq \frac{\pi}{2}$ in the radian scale as described in this section.

The azimuth and elevation angles of antenna rotation, $(\alpha_A, \beta_A)$, can be estimated exploiting sensors that have been already embedded to provide navigation and compass service in the current MSs such as smart phones. It is possible to use this information to physically control the Rx antenna polarization to compensate for Rx antenna rotation, if the MS has polarization-reconfigurable antennas which can rotate the orientation of antenna polarization. However, the polarization-reconfigurable antennas are not implemented in current MSs, and they may require more space than the currently used antennas. For this reason, we propose a scheme that adjusts the Tx polarization at the BS to tune the Rx-polarization at the MS to the optimal one for satisfactory SER performance. The optimal Tx-polarization estimation is performed based on the PSI of conventional V-H XPD, which is estimated at the Rx and relayed to the BS through the Tx–Rx feedback channel.

Once the PSI of conventional V-H XPD at the Rx is relayed to the Tx, the optimal Rx-polarization angles can be estimated at the Tx on a per-OFDM-block basis. Assuming the balanced-XPD scheme, which is more practical and shows better SER performance than the infinite-XPD scheme in Section 5.2, is adopted, the optimal Rx-polarization angle pair at MS-m that has to receive stream-$k$, $(\theta_{\mathrm{Rx},m}^{\mathrm{Opt},1}, \theta_{\mathrm{Rx},m}^{\mathrm{Opt},2})$, is estimated as follows:

$$\theta_{\mathrm{Rx},m}^{\mathrm{Opt},1} = \left(\arctan\left(\sqrt{|\mathrm{XPD}_m^{\mathrm{vh},k}|}\right) - \frac{\pi}{4}\right) \mod \pi, \tag{210}$$

$$\theta_{\mathrm{Rx},m}^{\mathrm{Opt},2} = \left(\theta_{\mathrm{Rx},m}^{\mathrm{Opt},1} + \frac{\pi}{2}\right) \mod \pi, \tag{211}$$

where $\mathrm{XPD}_m^{\mathrm{vh},k}$ is the conventional V-H XPD in the linear scale, and Rx-polarization angles are in the radian scale. Notice that the V-H XPD in (210) is estimated using MS's orthogonally polarized antennas, no matter how their orientation is rotated. In other words, the optimal Rx-polarization angle pair, $(\theta_{\mathrm{Rx},m}^{\mathrm{Opt},1}, \theta_{\mathrm{Rx},m}^{\mathrm{Opt},2})$, in (210) – (211) are not the absolute values but values relative to the rotated orthogonally polarized antennas. The objective of the collaborative Tx-Rx-polarization adjustment is to satisfy $(\theta_{\mathrm{Rx},m}^{\mathrm{Opt},1}, \theta_{\mathrm{Rx},m}^{\mathrm{Opt},2}) = (0, \frac{\pi}{2})$ or, equivalently, $\arctan\left(\sqrt{|\mathrm{XPD}_m^{\mathrm{vh},k}|}\right) = \frac{\pi}{4}$ in (210) – (211) by adjusting Tx-polarization angles referring the PSI of conventional V-H XPD relayed from the MS in an iterative manner.

Based on the estimated optimal Rx-polarization angles, the Tx can estimate optimal Tx-polarization angle pair to adjust Tx-polarization to it. If the current optimal Tx-polarization angle pair is $(\theta_{\mathrm{Tx}}^{\mathrm{Opt},1}, \theta_{\mathrm{Tx}}^{\mathrm{Opt},2})$ such that $0 \leq \theta_{\mathrm{Tx}}^{\mathrm{Opt},1}, \theta_{\mathrm{Rx},m}^{\mathrm{Opt},2} \leq \pi$ , then the next optimal Tx-polarization angle pair,$(\theta_{\mathrm{Tx}}^{\mathrm{Opt},1'}, \theta_{\mathrm{Tx}}^{\mathrm{Opt},2'})$, is determined as

$$\theta_{\mathrm{Tx}}^{\mathrm{Opt},1'} = \left(\theta_{\mathrm{Tx}}^{\mathrm{Opt},1} + \theta_{\mathrm{Rx},m}^{\mathrm{Opt},1}\right) \mod \pi, \tag{212}$$

$$\theta_{\mathrm{Tx}}^{\mathrm{Opt},2'} = \left(\theta_{\mathrm{Tx}}^{\mathrm{Opt},2} + \left(\theta_{\mathrm{Rx},m}^{\mathrm{Opt},2} - \frac{\pi}{2}\right)\right) \mod \pi. \tag{213}$$

Then adjusting Tx-polarization to the updated optimal Tx-polarization angle pair, $(\theta_{\mathrm{Tx}}^{\mathrm{Opt},1'}, \theta_{\mathrm{Tx}}^{\mathrm{Opt},2'})$, the optimal Rx-polarization angle pair $(\theta_{\mathrm{Rx},m}^{\mathrm{Opt},1'}, \theta_{\mathrm{Rx},m}^{\mathrm{Opt},2'})$, approaches $(0, \frac{\pi}{2})$ at the MS as implied in [9]. On the other hand, the MS can estimate the V-H XPD based on the streams transmitted from the BS applying the updated optimal Tx-polarization, $(\theta_{\mathrm{Tx}}^{\mathrm{Opt},1'}, \theta_{\mathrm{Tx}}^{\mathrm{Opt},2'})$, to the Tx antennas. The updated PSI of the conventional V-H XPD is relayed back to the Tx such that the Tx can estimate the new optimal Rx-polarization angle pair, $(\theta_{\mathrm{Rx},m}^{\mathrm{Opt},1'}, \theta_{\mathrm{Rx},m}^{\mathrm{Opt},2'})$ based on the relayed PSI of conventional V-H XPD. Finally, Tx can update its optimal Tx-polarization. In this manner, iterative Tx-Rx-polarization adjustment is performed on a per-OFDM-block basis, and the optimal Rx-polarization angle pair converges to $(0, \frac{\pi}{2})$.

For example, in the scenario of Figure 29, Rx and Tx polarization is horizontal and vertical, which corresponds to $(0°, 90°)$, at the first time. Then, $\mathrm{XPD}_1^{\mathrm{vh},1} = 10$ dB and $\mathrm{XPD}_2^{\mathrm{vh},2} = -12$ dB at MS-1 having $\phi(\mathrm{street}, \mathrm{Tx} - \mathrm{Rx}) = 75°$ and MS-2 having $\phi(\mathrm{street}, \mathrm{Tx} - \mathrm{Rx}) = 87°$, respectively. Once MS-1 and MS-2 relay their conventional V-H XPD to the BS, then the optimal Rx-polarization angle pairs of MS-1 and MS-2 are estimated at the BS. Assuming that balanced-XPD scheme is adopted, the optimal Rx-polarization angle pair of MS-1 is $(27°, 117°)$, and that of MS-2 is

$(31^\circ, 121^\circ, )$ from (210) – (211). The BS utilizes the element-based average of the estimated optimal Rx-polarization angle pairs, $(\theta_{\mathrm{Rx},m}^{\mathrm{Opt},1}, \theta_{\mathrm{Rx},m}^{\mathrm{Opt},2}) = (\ \overline{\theta_{\mathrm{Rx},m}^{\mathrm{Opt},1}}, \overline{\theta_{\mathrm{Rx},m}^{\mathrm{Opt},2}}) = (\frac{27^\circ+31^\circ}{2}, \frac{117^\circ+121^\circ}{2}) = (29^\circ, 119^\circ)$. Finally, the new optimal Tx-polarization angle pair, $(\theta_{\mathrm{Tx}}^{\mathrm{Opt},1'}, \theta_{\mathrm{Tx}}^{\mathrm{Opt},2'})$ in (212) – (213) is $(29^\circ, 119^\circ)$, since the previously used optimal Tx-polarization angle pair, $(\theta_{\mathrm{Tx}}^{\mathrm{Opt},1}, \theta_{\mathrm{Tx}}^{\mathrm{Opt},2})$ is $(0^\circ, 90^\circ)$ in this scenario. It is worth mentioning that conventional V-H XPD at both MS-1 and MS-2 is almost zero dB, which is the required condition of the balanced-XPD scheme, when the Tx polarization is adjusted to $(29^\circ, 119^\circ)$, which is almost same as $(30^\circ, 120^\circ)$ in Figure 29.

Optimal Rx-polarization angle pairs of MS-1 and MS-2 are almost same as each other in the given scenario of Figure 29. However, their mismatch can be serious owing to the substantial difference between the surroundings of MS-1 and MS-2. Even in this case, the BS can compensate for the mismatch of optimal Rx-polarization at MS-1 and MS-2. The BS can take into account both optimal Rx-polarization angle pairs, and apply the element-based average of optimal Rx-polarization angle pairs to (212) – (213) as a suboptimal one for each MS but an optimal one for both MSs. The satisfactory SER performance for both MSs will be exhibited in detail in Section 5.2.2. On the other hand, it is also possible that an element of the optimal Rx-polarization angle pair of MS-1 and an element of the other for MS-2 are used as $\theta_{\mathrm{Rx},m}^{\mathrm{Opt},1}$ and $\theta_{\mathrm{Rx},m}^{\mathrm{Opt},2}$, respectively if they are almost orthogonal. Good SER performance in this case is also realized in Section 5.2.2. The BS utilizes an optimal Rx-polarization angle pair estimated based on the relayed PSI of conventional V-H XPD from one MS when one of the MSs could not successfully relay its PSI of the conventional V-H XPD to the BS for any reason such as the estimation or detection error at the side of either BS or MS.

The proposed collaborative scheme of iterative Tx-Rx-polarization adjustment is summarized in Table 1.

**Table 1:** Collaborative scheme of iterative Tx-Rx-polarization adjustment.

| |
|---|
| *Step 1 – Initial Tx polarization*<br>The Tx transmits stream-1 and stream-2 for MS-1 and MS-2, with the initial Tx polarization, $(\theta^{\mathrm{Init},1}_{\mathrm{Tx}}, \theta^{\mathrm{Init},2}_{\mathrm{Tx}})$, respectively. |
| *Step 2 – Feedback for optimal Rx-polarization estimation*<br>Each MS estimates PSI of the conventional V-H XPD, $\mathrm{XPD}^{\mathrm{vh},k}_{m}$, and relays that PSI to the BS. |
| *Step 3 – Tx-polarization update and adjustment*<br>The BS updates and adjusts its Tx-polarization angle pair based on the relayed PSI from MS-1 and MS-2, and the estimated Rx-polarization angle pairs. The Tx utilizes<br>a. $\left(\overline{\theta^{\mathrm{Opt},1}_{\mathrm{Rx},m}}, \overline{\theta^{\mathrm{Opt},2}_{\mathrm{Rx},m}}\right)$: the average of the optimal Rx-polarization angle pairs relayed from MS-1 and MS-2.<br>b. $\left(\theta^{\mathrm{Opt},1}_{\mathrm{Rx},m}, \theta^{\mathrm{Opt},2}_{\mathrm{Rx},m}\right)$: the relayed optimal Rx-polarization angle pair, if the PSI has been successfully relayed from only one MS.<br>c. the previously used Tx-polarization angle pair, if the Tx could not receive both PSI from MS-1 and MS-2. Repeat the process from *Step 1* at the next transmission of the BS. |
| *Step 4 – Iterative Collaboration of Tx-Rx-polarization adjustment*<br>Go to *step 2*, and repeat *Step 2 – Step 3*. |

## *5.2 Simulation Results*

Consider an OFDMA system with $N = 2048$ sub-channels, $T = 1/(15 \text{ kHz}) = 66.7$ $\mu$sec block duration and $T_s = T/N \simeq 0.0326$ $\mu$sec symbol duration. This corresponds to one of the OFDMA modes in the long-term evolution (LTE) standard. Further, assume $P = N/32 = 64$ pilot symbols are equally spaced in each OFDM block. For pilot symbol allocation in (186) – (188), the offsets of the pilot symbols in an OFDM block are set as $j_{p,1} = 0$ and $j_{p,2} = 1$, and the number of sub-channels assigned information symbols is $S = N - 2P = 1920$. Two streams, $\{s_1\}$ and $\{s_2\}$, are transmitted concurrently on each sub-channel, and quadrature phase shift keying (QPSK) modulation is adopted. It is assumed that the Rx-polarization angles at each MS are 90° and 0° as described in Section 5.1.3.

Monte-Carlo simulation has been performed in MATLAB platform. PDMA channel impulse responses based on the geometry-based stochastic polarized channel model in [9] are utilized to show the SER/SINR performance according to the SNR for a variety of Tx polarization and geometrical scattering environments in Sections 5.2.1 and 5.2.2. The actual SNR considering the OFDM guard interval and the overhead of pilot sub-channels, $\mathrm{SNR}^{\mathrm{A}}$, can be expressed as

$$\begin{aligned}\mathrm{SNR}^{\mathrm{A}} &= 10\mathrm{log}_{10}\left(\frac{N+G}{N}\,\frac{N-P}{N-2P}\,\frac{E_s}{N_o}\right)\\ &= 10\mathrm{log}_{10}\left(\frac{2E_b}{N_o}\right) + (0.0840+0.0695)_{\mathrm{dB}},\\ &\quad \text{for } N=2048,\ P=32 \text{ and } G=40, \end{aligned} \tag{214}$$

where $E_s$ and $E_b = \frac{1}{2}E_s$ are, respectively, the modulated symbol and bit energy for the information symbol in the QPSK constellation. Further, $10\mathrm{log}_{10}\left(\frac{N+G}{N}\right) = 0.0840$ dB and $10\mathrm{log}_{10}\left(\frac{N-P}{N-2P}\right) = 0.0695$ dB, which reflect the modulated symbol energy in the guard interval and the pilot symbol energy in pilot sub-channels, respectively, on the SNR, can be regarded as negligible quantities. In the scenario of the single-stream/single-MS, $10\mathrm{log}_{10}\left(\frac{N-P}{N-2P}\right) = 0.0695$ dB in (214) is replaced with $10\mathrm{log}_{10}\left(\frac{N}{N-P}\right) = 0.0684$ dB, and the difference between the former and the latter is insignificant. The guard interval is not varied depending on whether single-stream/single-MS or multi-stream/multi-MS scenario. Notice that it is assumed that the modulated pilot symbol energy is same as the modulated information symbol energy, i.e., $E_p = E_s$. For the aforementioned reasons, a simplified SNR is utilized with insignificant difference from $\mathrm{SNR}^{\mathrm{A}}$ in the figures of Section 5.2. The SNR in $x$-axis of any figure in Section 5.2 is defined as the modulated information symbol energy-to-noise ratio for simplicity, i.e.,

$$\begin{aligned}\mathrm{SNR} &= 10\mathrm{log}_{10}\left(\frac{E_s}{N_o}\right) = 10\mathrm{log}_{10}\left(\frac{2E_b}{N_o}\right)\\ &= \mathrm{SNR}^{\mathrm{A}} - 10\mathrm{log}_{10}\left(\frac{N+G}{N}\,\frac{N-P}{N-2P}\right). \end{aligned} \tag{215}$$

Figure 30 describes the satisfactory SER performance with the proposed PDMA scheme in a normal scenario where the scattering environment is similar to that in suburban or urban area, i.e., maximum EAoA, $\beta_{R,Max}$ is 30°. Further, Figures 31 and 32 portray the SER and SINR performance deterioration caused by inappropriate Tx-polarization adjustment. Figure 33 visualizes the SER performance deterioration in the signal space even when the channel depolarization is not very serious such as 8 dB and -8 dB V-H XPD for the vertically and horizontally polarized Tx antennas, respectively. Finally, Figures 35 and 36 depict good SER performance with our scheme even in optimal Rx-polarization mismatch when two MSs are located in different scattering environments, i.e., in the suburban and the metropolitan areas; and in the rural and the metropolitan areas, respectively, within the same cell served by a BS.

### 5.2.1 SER performance of the PDMA scheme in the geometry-based stochastic polarized channel model

In this section, the polarized concentric-cylinders channel model described in Section 5.1.3 is used. The channel modeling parameters and geometrical scenario are exactly same as those in Figure 29. The radius of the scattering cylinder, $R_r$, in [27] is set to range from 10 m to 200 m to generate wide-band multi-path fading channels typically found in a metropolitan area. Such a range of $R_r$ results in a discrete-time channel with 25 to 35 $T_s$-spaced taps.

Figure 30 plots SER vs. SNR curves for $\{s_1\}$ at MS-1 and $\{s_2\}$ at MS-2, in PDMA channels in terms of the Tx polarization of the $\{s_1\}$ and $\{s_2\}$ streams. It is assumed that MS-1 and MS-2 in Figure 27 have the angles between the Tx–Rx boresight line and the street line of $\phi_1(\text{street}, \text{Tx} - \text{Rx}) = 63°$ and $\phi_2(\text{street}, \text{Tx} - \text{Rx}) = 87°$, respectively, which correspond to the first and the last points on each V-H XPD curve in Figure 29. Further, both MSs are 1 km far from the BS that transmits the streams with equal power allocation no mater what Tx polarization is utilized.

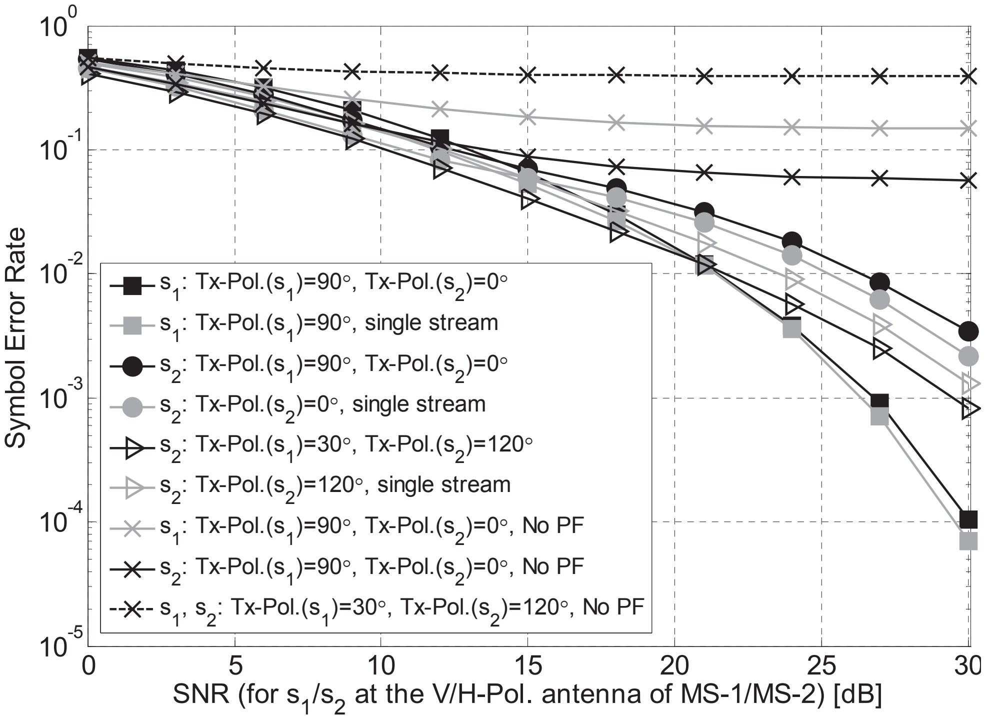

**Figure 30:** SER curves of $s_1(n)$ and $s_2(n)$ in PDMA channels according to the varying SNR and a variety of Tx polarization of two users.

The first scenario in Figure 30 occurs when the Tx antennas for $\{s_1\}$ and $\{s_2\}$ adjust their Tx polarization to vertical (90°) and horizontal (0°) polarization, respectively. On the other hand, the second scenario occurs when the Tx polarization of $\{s_1\}$ and $\{s_2\}$ are, 30° and 120°, respectively, where 30°/120° Tx polarization results in the V-H XPD ranging from -1 dB to 1dB, which is close to zero dB, at both MSs. The first scenario is the case of adopting the infinite-XPD scheme in Section 5.1.3, while the balanced-XPD schemes is utilized in the second scenario.

The SER performance for $\{s_1\}$ and $\{s_2\}$ in the first scenario is almost identical to that for $\{s_1\}$ and $\{s_2\}$ in the single-stream/single-MS scenario, although each single-stream/single-MS scenario may have distinct SER curve depending on the MS's relative location with respect to the BS, Tx polarization and corresponding channel impulse response in each scenario. In this scenario, the V-H XPD for $\{s_1\}$ and $\{s_2\}$ at MS-1 and MS-2, respectively, can be easily recognized as 8 dB and -12 dB, referring

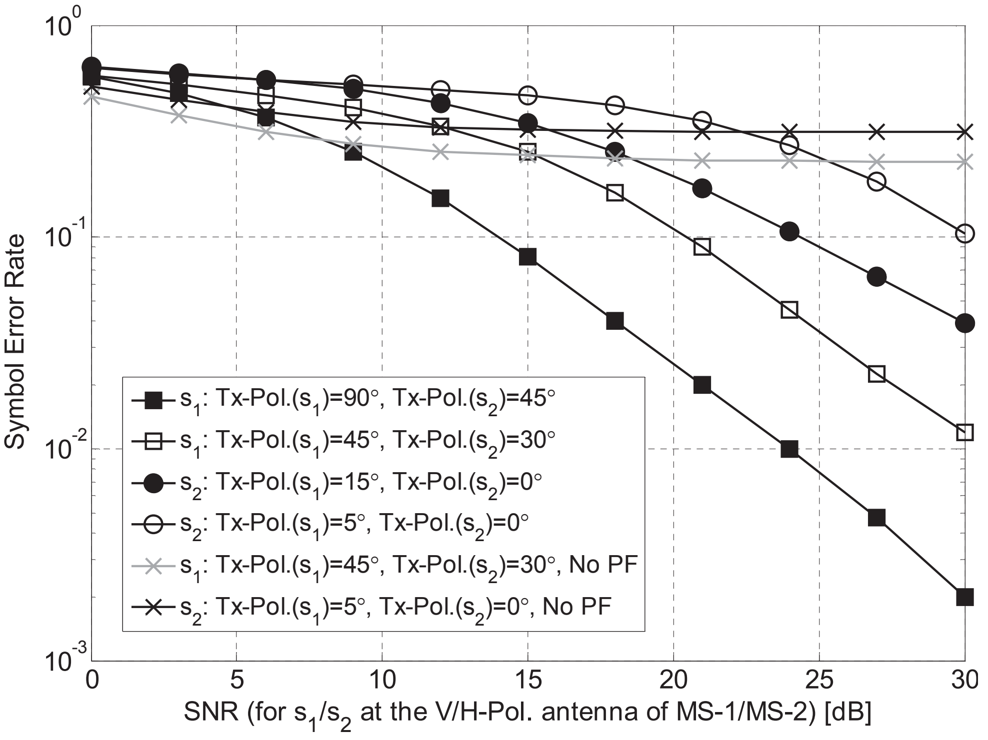

**Figure 31:** SER performance deterioration caused by inappropriate Tx-polarization adjustment in dual-user PDMA channels.

Figure 29. On the other hand, the balanced-XPD scheme in the second scenario exhibits slightly better SER for the stream $\{s_2\}$ at MS-2. The balanced-XPD scheme in the second scenario is regarded as superior to the infinite-XPD scheme in the first scenario in this respect.

The infinite-XPD scheme exhibits practical feasibility with satisfactory level of SER performance in Figure 30. In contrast, the SER performance deteriorates significantly as the Tx polarization for $\{s_1\}$ approaches that for $\{s_2\}$ as portrayed in Figure 31. The worst scenario among those in the legend of Figure 31 occurs when the MS-2 detects with the BS that adjusts its Tx polarization for $\{s_1\}$ and $\{s_2\}$ to 5° and 0°, respectively. In this scenario, the SER performance with PF-detection is even worse than that without PF-detection for the SNR in the range under 22 dB. The reason of this symptom is that the horizontally polarized signal component is stronger than the vertically polarized signal component both for $\{s_1\}$ and $\{s_2\}$ in this case. Thus, combining vertical and horizontal polarization branches by PF-detection exhibits the lower effective SNR than that of using only horizontal polarization branch in the range under 22 dB.

The SER performance in practical PDMA fading channels according to the Tx polarization described in Figures 30 – 31 is closely related with the effective SINR in (202) and (203). In general, as the difference between the Tx polarization for $\{s_1\}$ and $\{s_2\}$ at the BS increases, the difference between the V-H XPD at each MS increases; therefore, the effective SINR performance is improved as described in Figure 32. The last scenario, ($s_1$, $s_2$: Tx-Pol.($s_1$)=90°, Tx-Pol.($s_2$)=0°) in the legend of Figure 32 corresponds to the infinite-XPD scheme that shows satisfactory SER performance in Figure 30. In this scenario, the effective SINR is almost same as the SNR for the whole range of SNR in $x$-axis, which means that the interfering signal is almost completely filtered out by the proposed PF-detection with Tx-polarization adjustment as also implied in (202) and (203). On the other hand, the scenarios, ($s_2$: Tx-Pol.($s_1$)=5°, Tx-Pol.($s_2$)=0°) and ($s_1$: Tx-Pol.($s_1$)=45°, Tx-Pol.($s_2$)=30°) in the legend show unsatisfactory performance in terms of the effective SINR.

When the Tx has vertically and horizontally polarized antennas as in the last scenario of Figure 32, the effect of channel depolarization on the system performance may not be regarded as very serious. However, channel depolarization substantially affects the SER performance, although the V-H XPD at the Rx is 8 dB and -8 dB for vertical and horizontal Tx polarization, which is not very serious channel depolarization. The performance deterioration caused by the channel depolarization and the performance improvement obtained by PF-detection and Tx-Rx-polarization adjustment are depicted in Figure 33. The improvement in the SER performance from PF-detection and Tx-Rx-polarization adjustment is significant even when channel depolarization is not substantial as depicted in Figure 33.

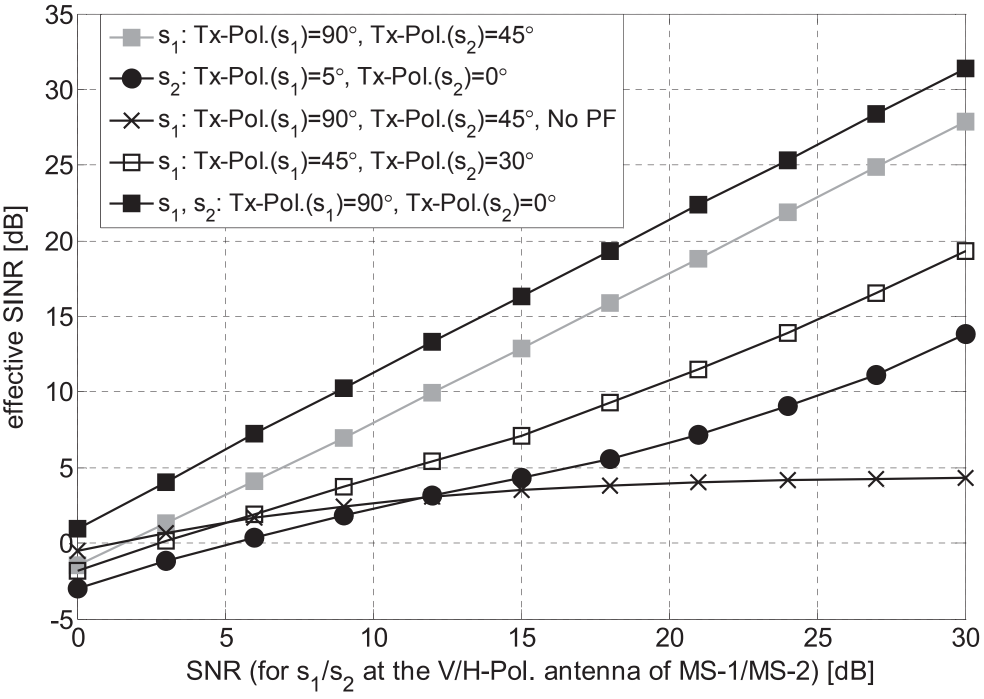

**Figure 32:** Effective SINR curves of $s_1(n)$ and $s_2(n)$ in PDMA channels according to the varying SNR and a variety of Tx polarization of two users.

### 5.2.2 SER performance with Rx-polarization mismatch

The Rx-polarization angle at a MS is not always same as or similar with that at other MSs, since the geometrical scattering environment of a MS can be distinct depending on its location. The V-H XPD curves portrayed in Figure 34 are generated for a variety of Tx-polarization using our earlier polarized channel model in [9]. Here, the maximum EAoA, $\beta_{R,Max}$ is 55° except the first scenario in the legend where $\beta_{R,Max} = 5°$. It is the main geometrical difference between the environments around the MS in Figures 29 and 34. Other channel modeling parameters and the geometrical scenario are exactly same as those in Figure 29. As described in detail in [9], high-elevation objects such as the building and bridge are the main components to create serious wireless channel depolarization. Further, as the height of an object increases or equivalently, as the maximum EAoA $\beta_{R,Max}$ increases, the symptom of channel depolarization becomes serious; therefore the difference between the Tx-polarization

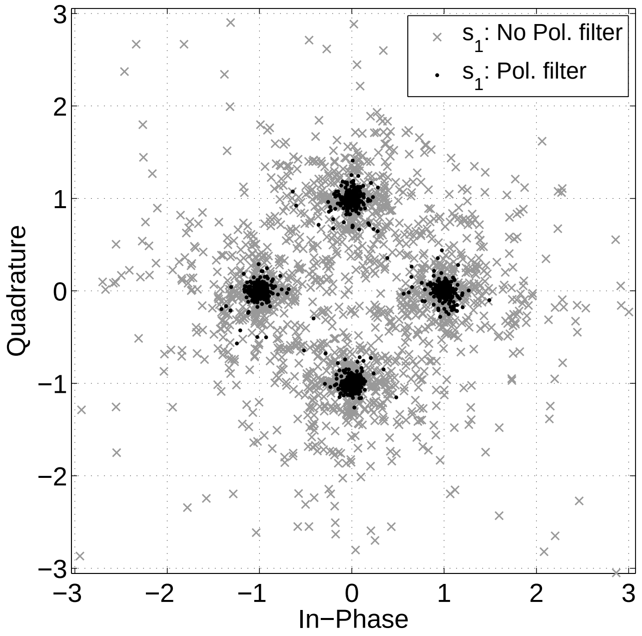

**Figure 33:** Signal space representation of the received baseband signals $s_1(n)$ in an OFDM block with/without PF-detection: SNR=30 dB, stream-1: vertical Tx polarization and 8 dB V-H Rx XPD, stream-2: horizontal Tx polarization and -8 dB V-H Rx XPD.

and Rx-polarization angles increases, and conventional V-H XPD decreases.

The optimal Tx-polarization angle pair for the balanced-XPD scheme, which is proposed in Section 5.1.3, is $(30°, 120°)$ when the maximum EAoA, $\beta_{R,Max}$, is 30° in Figure 29. On the other hand, the optimal Tx-polarization angle pairs are $(40°, 130°)$ and $(20°, 110°)$ for the maximum EAoA's, $\beta_{R,Max} = 5°$ and $\beta_{R,Max} = 55°$, respectively. Notice that the optimal Tx-polarization in the balanced-XPD scheme is the polarization angle of the transmitting antenna that yields 0 dB XPD, or equivalently, 45° or 135° Rx-polarization angle. Further, the optimal Tx-polarization angle pair estimated in Section 5.1.4, in particular, utilizing (210) – (213), is in good agreement with the aforementioned one obtained by the simulation with a variety of Tx-polarization angles to find out the optimal one in Figures 29 and 34.

It is apparent that the maximum EAoA tends to increase owing to high-elevation structures as the cell served by a BS becomes more urbanized. The aforementioned maximum EAoA's, $\beta_{R,Max} = 5°$, $\beta_{R,Max} = 30°$, and $\beta_{R,Max} = 55°$, may be regarded

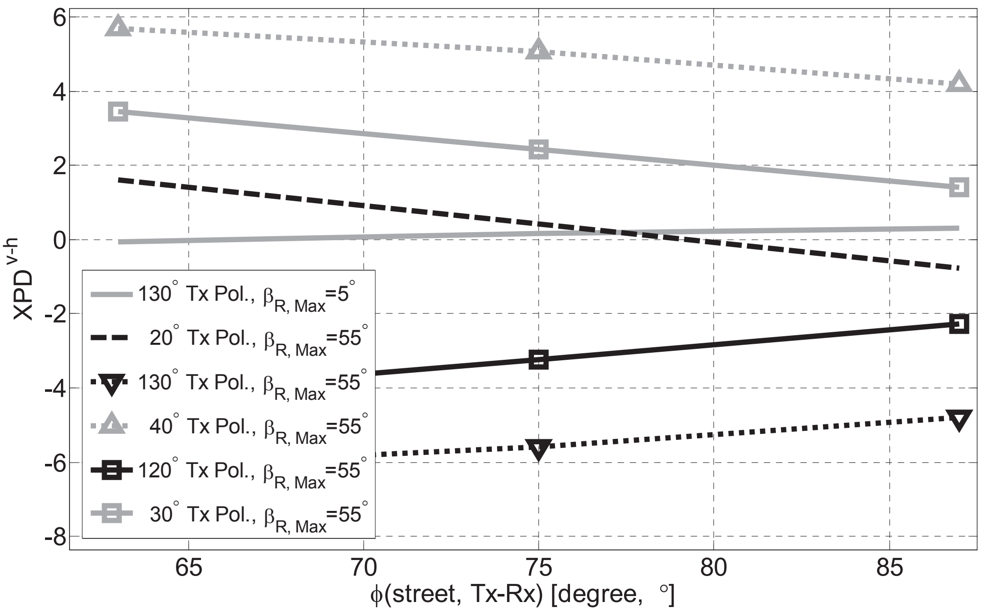

**Figure 34:** XPD curves of a scenario, $\beta_{R,Max} = 55°$, for the Tx-Rx line and street line geometry with a variety of Tx-polarization angles; $\mu_R = 180° - \phi(\text{street}, \text{Tx} - \text{Rx})$, $k_R = 20$, $R_r = 10 - 200$ m, $h_T = 35$ m, $h_R = 1.65$ m, $D = 1$ km, propagation path loss exponent $n = 3.5$.

as those of rural, suburban, and urban/metropolitan areas in a physical sense. The larger difference in maximum EAoA's results in a greater mismatch in the optimal Tx-polarization, i.e., the mismatch of optimal Tx-polarization pairs is 10° for each 25° difference of the maximum EAoA in the given geometrical scenarios in Figs 29 and 34. Figure 34 will be explained further along with the description of Figures 35 and 36 in the sequel.

MS-1 and MS-2 are assumed to be surrounded by different environments in terms of the maximum EAoA, $\beta_{R,Max}$, and the angle between Tx-Rx boresight line and street line, $\phi(\text{street}, \text{Tx} - \text{Rx})$, as described in detail in the figure caption of Figure 35. That is, MS-1 and MS-2 can be considered to be in a suburban area ($\beta_{R,Max} = 30°$) and a metropolitan area ($\beta_{R,Max} = 55°$), respectively, within the same cell served by a BS. The geometry-based stochastic channel simulation model is utilized in the same manner as Section 5.2.1. The estimated optimal Tx-polarization angle pairs for MS-1 and MS-2 based on the relayed CSI from the MSs are, respectively, $(30°, 120°)$

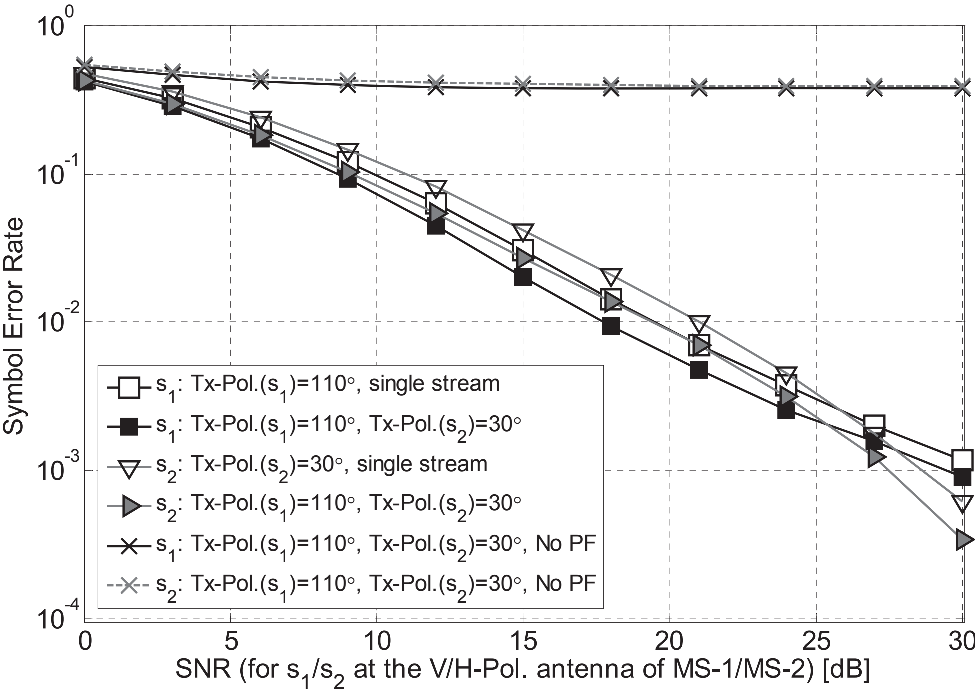

**Figure 35:** SER curves of $s_1(n)$ and $s_2(n)$ in PDMA channels according to the varying SNR. MS-1: $\beta_{R,Max} = 30°$, $\phi(\text{street}, \text{Tx} - \text{Rx}) = 63°$ while MS-2: $\beta_{R,Max} = 55°$, $\phi(\text{street}, \text{Tx} - \text{Rx}) = 87°$.

and $(20°, 110°)$ as shown in Figures 29 and 34. The Tx adjusts its polarization to the suboptimal Tx-polarization angle pair, $(30°, 110°)$, instead of one of the original optimal Tx-polarization angle pairs to compensate the mismatch between them. The suboptimal Tx polarization results in satisfactory SER performance for both $\{s_1\}$ at MS-1 and $\{s_2\}$ at MS-2 as depicted in Figure 35.

The mismatch between the optimal Tx-polarization angle pairs for MS-1 and MS-2 in the scenario of Figure 36 is greater than that in Figure 35 as described in the figure caption of Figure 36. It is assumed that MS-1 lies in a rural area ($\beta_{R,Max} = 5°$), while MS-2 lies in a metropolitan area ($\beta_{R,Max} = 55°$), although they are in the same cell served by a BS. In the given scenario, the optimal Tx-polarization angle pairs for MS-1 and MS-2 are, respectively, $(40°, 130°)$ and $(20°, 110°)$ based on Figure 34. In this case, the suboptimal Tx-polarization pair, $(40°, 110°)$ or $(20°, 130°)$, which is adopted in the same fashion as the previous scenario in Figure 35, does not yield satisfactory SER performance for both MS-1 and MS-2. The reason is that the optimal Tx-polarization angle pairs for MS-1 and MS-2 have a significant mismatch between them; therefore, the suboptimal Tx-polarization angle pair shows substantial difference from the optimal Tx-polarization angle pairs in terms of the orthogonality between two elements of a Tx-polarization angle pair.

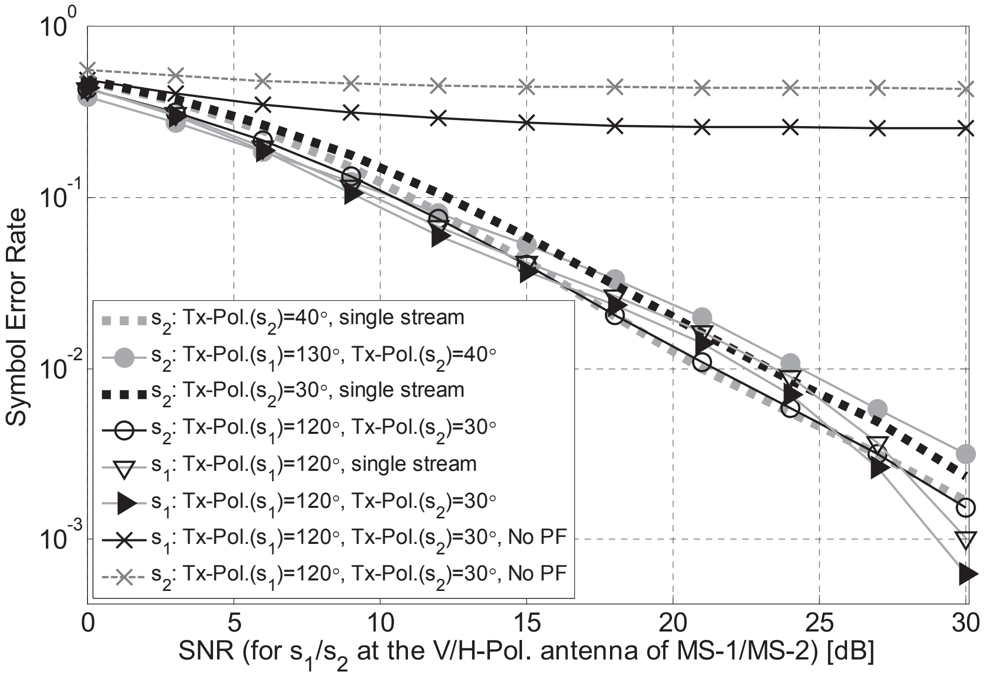

**Figure 36:** SER curves of $s_1(n)$ and $s_2(n)$ in PDMA channels according to the varying SNR. MS-1: $\beta_{R,Max} = 5°$, $\phi(\text{street}, \text{Tx} - \text{Rx}) = 63°$ while MS-2: $\beta_{R,Max} = 55°$, $\phi(\text{street}, \text{Tx} - \text{Rx}) = 87°$.

When the Tx adjust its polarization to an optimal polarization angle pair, $(40°, 130°)$, only for MS-1, the SER performance for $s_2$ at MS-2 shows considerable deterioration comparing to the single-stream/single-MS scenario as portrayed by two curves corresponding to the first and second scenarios in the legend of Figure 36. The SNR difference in $x$-axis between two curves is greater than 3 dB to have the same SER in $y$-axis for the SNR range of 25 dB to 30 dB. It means the stream $\{s_2\}$ must have over twice greater transmitted symbol power in the given PDMA scenario than that in the single-stream scenario to have the same SER performance. The reason for the SER performance deterioration can be easily estimated based on the conventional V-H XPD curves of the scenarios, (40° Tx Pol., $\beta_{R,Max}$=55°) and (130° Tx Pol., $\beta_{R,Max}$=55°) in the legend of Figure 34. For those scenarios, which correspond to the aforementioned Tx-polarization angle pair, $(40°, 130°)$, the conventional V-H XPD at MS-2 is 4 dB and -5 dB when MS-2 has the environment corresponding to $\phi(\mathrm{street}, \mathrm{Tx} - \mathrm{Rx}) = 87°$ and $\beta_{R,Max} = 55°$. That V-H Rx-XPD for Tx-polarization angle pair, $(40°, 130°)$, satisfies the condition of neither balanced-XPD nor infinite-XPD and, thus, does not attain a satisfactory level of SER.

On the other hand, the Tx can adjust its polarization to the suboptimal Tx-polarization angle pair, $(30°, 120°)$, which is the average of the original optimal Tx-polarization angle pairs of MS-1 and MS-2, $(40°, 130°)$ and $(20°, 110°)$, as described in Section 5.1.4. As depicted in the third to sixth scenario in the legend of Figure36, this suboptimal Tx-polarization angle pair exhibits satisfactory SER for both stream $\{s_1\}$ at MS-1 and $\{s_2\}$ at MS-2 comparing with the single-stream/single-MS scenario for each stream/MS. For this suboptimal Tx-polarization angle pair, the conventional V-H XPD at MS-2 is 1.5 dB and -2 dB at the location where MS-2 is surrounded by the environment corresponding to $\phi(\mathrm{street}, \mathrm{Tx} - \mathrm{Rx}) = 87°$ and $\beta_{R,Max} = 55°$, referring, again, to the last two scenarios in the legend of Figure 34. That is, the SER performance is satisfactory when the V-H XPD of two received signals is 1.5 dB and -2 dB, which can be regarded as satisfying the condition of the balanced-XPD scheme. In a similar manner with the SER of $\{s_2\}$ at MS-2, that of $\{s_1\}$ at MS-1 also exhibits good SER performance as portrayed in Figure 36.

## 5.3 Summary

This chapter has proposed a novel PDMA scheme utilizing PF-detection and collaborative Tx-Rx-polarization estimation/adjustment for wide-band NLoS wireless polarized fading channels. A comprehensive research was accomplished starting with proposing a new PDMA scheme with the new Rx structure for the PF-detection and iterative Tx-Rx-polarization adjustment, analyzing PDMA channel capacity in a theoretical manner, providing the appropriate estimation and pilot symbol allocation in OFDMA systems, and lastly, evaluating SER and effective SINR performances. In particular, for proving the practical feasibility of the new PDMA scheme, we did not assume the perfect CSI/PSI, but utilized pilot symbol-aided OFDM channel estimator along with geometry-based polarized fading channel simulation model. The proposed scheme's feasibility and excellent SER/SINR performance is shown so that the new PDMA scheme is regarded as having dramatic potential to be utilized for a new paradigm of multiple access in the next-generation cellular systems and also other telecommunications systems.

# CHAPTER VI

# CONTRIBUTIONS AND FUTURE RESEARCH

## *6.1 Research Contributions*

To the best of our knowledge, the proposed theory and models in this thesis are the first which reveals the origin and mechanism of wireless channel depolarization in a geometry-based methodology, and provides the method of deriving XPD in a quantitative manner for a given geometrical environment. Furthermore, the PDMA scheme in this thesis is the first which shows feasibility of utilizing polarization domain for a multiple access/multiplexing scheme without the aid of spatial diversity or other MIMO techniques in the OFDMA-based wireless cellular systems. This section summarizes the contributions of this thesis.

A geometrical theory, which can reveal the origin of wireless channel depolarization is established. The theory can also describe the general mechanism of channel depolarization, which can be applied to any other wireless communication systems even having NLoS reflected/scattered wave propagation components. We show that the tilt of "*conservation-of-polarization (CoP)*" plane in three-dimensional 3-D space creates wireless channel depolarization, and verify it by comparing XPD curves obtained in a manner of quantitative computation and from previously reported measurements.

A theoretical stochastic model of the narrow-band polarized wireless fading channel in the F2M scenario, is developed based on the aforementioned geometrical theory. The F2M polarized channel model is verified, and shows good agreement with empirical data reported by other authors.

A M2M polarized channel model is proposed by extending F2M polarized channel model. This model successfully describes the change of wireless channel polarization in the double-bounce radio propagation, which means the waves reflected once at the Tx side and then reflected again at the Rx side in vehicular communications. The model also provides the quantitative way of obtaining XPD, and shows different XPD curves from those of the F2M channel scenario.

A unique 3-D geometry-based statistical model for the polarized wireless BAN channel with three different propagation modes, CSS, BS and GS propagation modes, is developed. Further, a theoretical modeling of the creeping wave using diffraction theories is performed, and the empirical validation of the proposed model is also provided with a good agreement between the theoretical and empirical results of channel characteristics. Several meaningful analytical characteristics of polarized BAN channels are also presented based on the proposed BAN channel model.

A novel cellular down-link *Polarization Division Multiple Access (PDMA)* scheme with PF-detection and collaborative Tx-Rx-polarization adjustment is proposed for wide-band NLoS wireless polarized fading channels. The fundamental novelty of the proposed scheme is that it can adjust transmit polarization angles to change the channel impulse response itself and yield a more desirable complex XPD observed at receivers. This is a significant difference between the proposed scheme and the conventional MIMO systems. The capacity analysis of the proposed PDMA scheme is provided, and the feasibility and satisfactory performance of the proposed scheme are demonstrated even when serious time-variant channel depolarization and polarization mismatch between receivers occur. The proposed cellular down-link PDMA scheme uses synchronous OFDMA with an appropriate channel parameter estimator. The scheme can be used to extend the capacity of any cellular system that uses uni-polarized antennas, and can be extended and applied to MIMO arrays as well.

## *6.2 Future Research*

A novel PDMA scheme for the cellular down-links was proposed in this thesis. The PDMA scheme utilizes collaborative Tx-Rx–polarization adjustment through the feedback channel between the Tx and Rx to satisfy the condition of the balanced-XPD or infinite-XPD scheme. The conventional XPD is used for the proposed Tx-polarization adjustment, and the PDMA scheme having two principal functions - PF-detection and Tx-Rx-polarization adjustment - shows satisfactory SER/SINR performance.

Nonetheless, the performance of the proposed PDMA scheme may be improved more than that presented in Cahpter 5, if the characteristics of the XPD are determined on a per-subcarrier basis. The XPD curve in the frequency domain may have considerable variation since the OFDMA waveform exhibits substantial envelope fluctuation, which causes a high peak-to-average power ratio (PAPR). Thus, the performance of the PDMA system for each sub-channel can be different from each other owing to the frequency-dependence of the XPD. For that reason, PDMA system performance for a variety of sub-channels is expected to be a considerable issue to be studied in future research.

The PDMA scheme suggested in this thesis utilizes synchronous OFDMA. It is noteworthy that not only PDMA but also OFDMA is a multiple access scheme. While all sub-channels for information symbols are employed by each user in Chapter 5, only some portions of them are assigned to each user in the practical cellular multi-user system. The sub-channels are assigned to each user according to an appropriate algorithm such as the localized or distributed sub-channel assignment. However, when the PDMA is combined with OFDMA, and both multiple access methodologies are utilized together, a new sub-channel assignment algorithm is required since the XPD exhibits frequency selectivity; therefore PDMA performance also depends on the assigned sub-channels. The PDMA-OFDMA scheme such as the XPD-aware sub-channel assignment algorithm will be a good issue in future research to maximize the performance of the PDMA-OFDMA system.

# APPENDIX A

# DERIVATION OF THE POLARIZATION FUNCTION IN THE SBT PROPAGATION MODE

From the geometry in Figure 6, the distances are

$$d_t = \sqrt{D^2 + {R_t}^2 - 2R_t D\cos\alpha_T}, \tag{216}$$

$$D_{sr} = \sqrt{{d_t}^2 + (\Delta_h + R_t\tan\beta_T)}, \;\; D_{ts} = R_t/\cos\beta_T, \tag{217}$$

$$D_{tr} = \sqrt{D^2 + {\Delta_h}^2}, \;\; d_2 = \sqrt{{d_t}^2 + {\Delta_h}^2} \tag{218}$$

where $\Delta_h = (h_T - h_R)$. Based on (216) – (218) and the law of cosines, the angles in Figure 6 can be written as

$$\cos\phi_1 = \frac{{D_{tr}}^2 + {d_2}^2 - {R_t}^2}{2D_{tr}d_2} = \frac{b_2 + b_4}{\sqrt{\left((R_t/D)^2 - 2b_2 + b_4\right)b_4}}, \tag{219}$$

$$\begin{aligned}\cos\phi_2 &= \frac{{D_{sr}}^2 + {d_2}^2 - {R_t}^2\tan^2\beta_T}{2D_{sr}d_2} \\ &= \frac{(R_t/D)^2 - 2b_2 + b_3 + b_4}{\sqrt{\left({b_1}^2 - 2b_2 + 2b_3 + b_4\right)\left((R_t/D)^2 - 2b_2 + b_4\right)}},\end{aligned} \tag{220}$$

$$\cos\phi_3 = \frac{{D_{ts}}^2 + {D_{tr}}^2 - {D_{sr}}^2}{2D_{ts}D_{tr}} = \frac{(b_2 - b_3)\cos\beta_T}{\sqrt{b_4}}, \tag{221}$$

$$\cos\phi_4 = \frac{{D_{tr}}^2 + {R_t}^2 - {d_2}^2}{2D_{tr}R_t} = \frac{\cos\alpha_T}{\sqrt{b_4}}, \tag{222}$$

$$\cos\phi_5 = \frac{\cos\phi_1 - \cos\phi_2\cos\phi_7}{\sqrt{(1 - \cos^2\phi_2)(1 - \cos^2\phi_7)}}, \tag{223}$$

$$\cos\phi_6 = \frac{\cos\phi_4 - \cos\beta_T\cos\phi_3}{\sqrt{(1 - \cos^2\beta_T)(1 - \cos^2\phi_3)}}, \qquad \phi_V = \pi - \phi_6, \tag{224}$$

$$\cos\phi_7 = \frac{{D_{tr}}^2 + {D_{sr}}^2 - {D_{ts}}^2}{2D_{tr}D_{sr}} = \frac{-b_2 + b_3 + b_4}{\sqrt{(b_1 - 2b_2 + 2b_3 + b_4)\,b_4}}, \tag{225}$$

$$b_1 = \frac{R_t/D}{\cos\beta_T}, \;\; b_2 = \frac{R_t}{D}\cos\alpha_T, \;\; b_3 = \frac{R_t\Delta_h}{D^2}\tan\beta_T, \;\; b_4 = 1 + \left(\frac{\Delta_h}{D}\right)^2. \tag{226}$$

Finally, $\cos\phi_5$ and $\cos\phi_6$ in (223) and (224), respectively, are used to derive the channel polarization functions $f_{VV}^{SBT}$, $f_{HV}^{SBT}$, $f_{HH}^{SBT}$ and $f_{VH}^{SBT}$ in (40) and (41).

# APPENDIX B

# DERIVATION OF THE POLARIZATION FUNCTION IN THE DB PROPAGATION MODE

Using the geometry in Figure 7, the distances are expressed as

$$\begin{aligned}
{D_{O_{S_t}O_{S_r}}}^2 &= \left(D - R_t\cos\alpha_T + R_r\cos\alpha_R\right)^2 + \left(R_t\sin\alpha_T - R_r\sin\alpha_R\right)^2, && (227)\\
{D_{S_tS_r}}^2 &= {D_{O_{S_t}O_{S_r}}}^2 + \left(\Delta_h + R_t\tan\beta_T - R_r\tan\beta_R\right)^2, && (228)\\
{D_{H_tS_r}}^2 &= {D_{O_{S_t}O_{S_r}}}^2 + \left(R_r\tan\beta_R - \Delta_h\right)^2, && (229)\\
{D_{H_rS_t}}^2 &= {D_{O_{S_t}O_{S_r}}}^2 + \left(R_t\tan\beta_T + \Delta_h\right)^2, && (230)\\
{D_{O_tO_{S_r}}}^2 &= \left(R_r\sin\alpha_R\right)^2 + \left(D + R_r\cos\alpha_R\right)^2, && (231)\\
{D_{O_rO_{S_t}}}^2 &= \left(R_t\sin\alpha_T\right)^2 + \left(D + R_t\cos\alpha_T\right)^2, && (232)\\
{D_{TS_r}}^2 &= {D_{O_tO_{S_r}}}^2 + \left(R_r\tan\beta_R - \Delta_h\right)^2, && (233)\\
{D_{RS_t}}^2 &= {D_{O_rO_{S_t}}}^2 + \left(R_t\tan\beta_T + \Delta_h\right)^2, && (234)\\
D_{TS_t} &= R_t/\cos\beta_T,\ \ D_{RS_r} = R_r/\cos\beta_R, && (235)
\end{aligned}$$

where $\Delta_h = (h_T - h_R)$. Based on (227) – (235) and the law of cosines, the angles associated with the SBT-like propagation mode in Figure 7 are:

$$\cos\phi_1' = \angle TS_RH_t = \frac{{D_{TS_r}}^2 + {D_{H_tS_r}}^2 - {R_t}^2}{2D_{TS_r}D_{H_tS_r}}, \qquad (236)$$

$$\cos\phi_2' = \angle S_tS_rH_t = \frac{{D_{S_tS_r}}^2 + {D_{H_tS_r}}^2 - {R_t}^2\tan^2\beta_T}{2D_{S_tS_r}D_{H_tS_r}}, \qquad (237)$$

$$\cos\phi_3' = \angle S_tTS_r = \frac{{D_{TS_t}}^2 + {D_{TS_r}}^2 - {D_{S_tS_r}}^2}{2D_{TS_t}D_{TS_r}}, \qquad (238)$$

$$\cos\phi_4' = \angle H_tTS_r = \frac{{R_t}^2 + {D_{TS_r}}^2 - {D_{H_tS_r}}^2}{2R_tD_{TS_r}}, \qquad (239)$$

$$\cos\phi_5' = \frac{\cos\phi_1' - \cos\phi_2'\cos\phi_7'}{\sqrt{\left(1-\cos^2\phi_2'\right)\left(1-\cos^2\phi_7'\right)}}, \qquad (240)$$

$$\cos\phi'_6 = \frac{\cos\phi'_4 - \cos\beta_T \cos\phi'_3}{\sqrt{(1-\cos^2\beta_T)\,(1-\cos^2\phi'_3)}}, \tag{241}$$

$$\cos\phi'_7 = \angle S_t S_r T = \frac{{D_{S_tS_r}}^2 + {D_{TS_r}}^2 - {R_t}^2/\cos^2\beta_T}{2D_{S_tS_r}D_{TS_r}} \quad , \tag{242}$$

$$\phi_V = \pi - \phi'_6 \ . \tag{243}$$

The angles $\cos\phi'_5$ and $\cos\phi'_6$ in (240) and (241), respectively, can be used to derive the channel polarization functions of the DB propagation mode as a function of $\alpha_R$, $\beta_R$, $\alpha_T$, $\beta_T$, $R_r$, $R_t$, and $D$.

Likewise, the angles associated with the SBR-like propagation mode in Figure 7 can be expressed as:

$$\cos\theta'_3 = \angle S_r S_t R = \frac{{D_{S_tS_r}}^2 + {D_{RS_t}}^2 - {D_{RS_r}}^2}{2D_{S_tS_r}D_{RS_t}}, \tag{244}$$

$$\cos\theta'_4 = \angle S_r S_t H_r = \frac{{D_{S_tS_r}}^2 + {D_{H_rS_t}}^2 - {R_r}^2\tan^2\beta_R}{2D_{S_tS_r}D_{H_rS_t}}, \tag{245}$$

$$\cos\theta'_5 = \angle R S_t H_r = \frac{{D_{H_rS_t}}^2 + {D_{RS_t}}^2 - {R_r}^2}{2D_{H_rS_t}D_{RS_t}}, \tag{246}$$

$$\cos\theta'_6 = \frac{\cos\theta'_5 - \cos\theta'_3\cos\theta'_4}{\sqrt{(1-\cos^2\theta'_3)\,(1-\cos^2\theta'_4)}}, \tag{247}$$

$$\cos\theta'_7 = \angle S_t R S_r = \frac{{D_{RS_t}}^2 + {R_r}^2/\cos^2\beta_R - {D_{S_tS_r}}^2}{2D_{RS_t}R_r/\cos\beta_R}, \tag{248}$$

$$\cos\theta'_8 = \angle S_t R H_r = \frac{{D_{RS_t}}^2 + {R_r}^2 - D_{H_rS_t}}{2D_{RS_t}R_r}, \tag{249}$$

$$\cos\theta'_9 = \frac{\cos\theta'_8 - \cos\beta_R\cos\theta'_7}{\sqrt{(1-\cos^2\beta_R)\,(1-\cos^2\theta'_7)}}, \tag{250}$$

$$\phi_V = \pi - \theta'_6 \ . \tag{251}$$

Once again, the angles $\cos\theta'_6$ and $\cos\theta'_9$ in (247) and (250), respectively, can be used to derive the channel polarization functions of the DB propagation mode as a function of $\alpha_R$, $\beta_R$, $\alpha_T$, $\beta_T$, $R_r$, $R_t$, and $D$.

# REFERENCES

[1] P. Soma, D. S. Baum, V. Erceg, R. Krishnamoorthy, and A. J. Paulraj, "Analysis and modeling of MIMO radio channel based on outdoor measurements conducted at 2.5 GHz for fixed BWA applications," in *Proc. IEEE Int. Conf. Commun.*, vol. 1, pp. 272–276, Apr. 2002.

[2] R. G. Vaughan, "Polarization diversity in mobile communications," *IEEE Trans. Veh. Technol.*, vol. 39, pp. 177–185, Jun. 1990.

[3] S. Kozono, T. Suruhara, and M. Sakamoto, "Base station poloarization diversity reception for mobile radio," *IEEE Trans. Veh. Technol.*, vol. 33, pp. 301–306, Nov. 1984.

[4] W. Lee and Y. Yeh, "Polarization diversity system for mobile radio," *IEEE Trans. Commun.*, vol. 20, pp. 912–923, Oct. 1972.

[5] C. Oestges, V. Erceg, and A. J. Paulraj, "Propagation modeling of MIMO multipolarized fixed wireless channels," *IEEE Trans. Veh. Technol.*, vol. 53, pp. 644–654, May 2004.

[6] M. R. Andrews, P. P. Mitra, and R. deCarvalho, "Tripling the capacity of wireless communications using electromagnetic polarization," *Nature*, vol. 409, pp. 316–318, Jan. 2001.

[7] M. Landmann, K. Sivasondhivat, J.-I. Takada, I. Ida, and R. Thoma, "Polarisation behaviour of discrete multipath and diffuse scattering in urban environments at 4.5 GHz," *EURASIP J. Wireless Commun. Netw.*, p. 60, Jan. 2007 Article ID 57980.

[8] M. Shafi, M. Zhang, A. Moustakas, P. Smith, A. Molisch, F. Tufvesson, and S. Simon, "Polarized MIMO channels in 3-D: Models, measurements, and mutual information," *IEEE J. Sel. Areas Commun.*, vol. 24, pp. 514–527, Mar. 2006.

[9] S.-C. Kwon and G. L. Stüber, "Geometrical theory of channel depolarization," *IEEE Trans. Veh. Technol.*, vol. 60, pp. 3542–3556, Oct. 2011.

[10] S.-C. Kwon, G. Stüber, A. López, and J. Papapolymerou, "Geometrically based statistical model for polarized body-area-network channels," *IEEE Trans. Veh. Technol.*, vol. 62, pp. 3518–3530, Oct. 2013.

[11] S.-C. Kwon, G. Stüber, A. López, and J. Papapolymerou, "Polarized channel model for body area networks with dominant ground scattering," *Submitted to IEEE Trans. Veh. Technol.*, Oct. 2013.

[12] V. Erceg, P. Soma, D. Baum, and S. Catreux, “Multiple-input multiple-output fixed wireless radio channel measurements and modeling using dual-polarized antennas at 2.5 GHz,” *IEEE Trans. Wireless Commun.*, vol. 3, pp. 2288 – 2298, Nov. 2004.

[13] V. Erceg, H. Sampath, and S. Catreux-Erceg, “Dual-polarization versus single-polarization MIMO channel measurement results and modeling,” *IEEE Trans. Wireless Commun.*, vol. 5, pp. 28–33, Jan. 2006.

[14] S.-C. Kwon and Stüber, “Polarization division multiple access on NLoS wide-band wireless fading channels,” *Conditional acceptance on IEEE Trans. Wireless Commun.*, Dec. 2013.

[15] T. Svantesson, “A double-bounce channel model for multi-polarized MIMO systems,” in *Proc. IEEE Veh. Technol. Conf.*, vol. 2, pp. 691–695, Fall 2002.

[16] L. Jiang, L. Thiele, and V. Jungnickel, “On the modelling of polarized MIMO channel,” in *Proc. European Wireless Conf.*, 2007. [CD-ROM].

[17] F. Quitin, C. Oestges, F. Horlin, and P. De Doncker, “Multipolarized MIMO channel characteristics: Analytical study and experimental results,” *IEEE Trans. Antennas Propag.*, vol. 57, pp. 2739–2745, Sept. 2009.

[18] A. Abdi and M. Kaveh, “A space-time correlation model for multielement antenna systems in mobile fading channels,” *IEEE J. Sel. Areas Commun.*, vol. 20, pp. 550–560, Apr. 2002.

[19] G. Byers and F. Takawira, “Spatially and temporally correlated MIMO channels: modeling and capacity analysis,” *IEEE Trans. Veh. Technol.*, vol. 53, pp. 634–643, May 2004.

[20] M. Patzold, B. Hogstad, N. Youssef, and D. Kim, “A MIMO mobile-to-mobile channel model: Part i - the reference model,” in *Proc. IEEE Int. Symp. on Personal, Indoor and Mobile Radio Commun.*, vol. 1, pp. 573–578, Sept. 2005.

[21] T. Aulin, “A modified model for the fading signal at a mobile radio channel,” *IEEE Trans. Veh. Technol.*, vol. 28, pp. 182–203, Aug. 1979.

[22] A. S. Akki and F. Haber, “A statistical model for mobile-to-mobile land communication channel,” *IEEE Trans. Veh. Technol.*, vol. 35, pp. 2–10, Feb. 1986.

[23] “Spatial channel model for multiple input multiple output MIMO simulations.” 3GPP, TR 25.996, 6.1.0 ed., 2003.

[24] W. Weichselberger, M. Herditt, H. Ozcelik, and E. Bonek, “A stochastic MIMO channel model with joint correlation of both link ends,” *IEEE Trans. Wireless Commun.*, vol. 5, pp. 90–100, Jan. 2006.

[25] A. G. Zajić and G. L. Stüber, "Three-dimensional modeling, simulation, and capacity analysis of space-time correlated mobile-to-mobile channels," *IEEE Trans. Veh. Technol.*, vol. 57, pp. 2042–2054, Jul. 2008.

[26] A. G. Zajić, G. L. Stüber, T. G. Pratt, and S. Nguyen, "Wide-band MIMO mobile-to-mobile channels: Geometry-based statistical modeling with experimental verification," *IEEE Trans. Veh. Technol.*, vol. 58, pp. 517–534, Feb. 2009.

[27] A. Zajić and G. Stüber, "Three-dimensional modeling and simulation of wideband MIMO mobile-to-mobile channels," *IEEE Trans. Wireless Commun.*, vol. 8, pp. 1260–1275, Mar. 2009.

[28] N. Timmons and W. Scanlon, "Analysis of the performance of IEEE 802.15.4 for medical sensor body area networking," in *Proc. IEEE Sensor and Ad Hoc Commun. and Netw.*, pp. 16–24, Oct. 2004.

[29] E. Jovanov, A. Milenkovic, C. Otto, and P. Groen, "A wireless body area network of intelligent motion sensors for computer assisted physical rehabilitation," *J. Nuroengin. and Rehabil.*, Mar. 2005.

[30] R. D'Errico and L. Ouvry, "A statistical model for on-body dynamic channels," *Int. J. Wireless Inform. Netw.*, vol. 17, pp. 92–104, Dec. 2010.

[31] J. Ryckaert, P. D. Doncker, R. Meys, A. de Le Hoye, and S. Donnay, "Channel model for wireless communication around human body," *Electronics Letters*, vol. 40, pp. 543–544, Apr. 2004.

[32] S. Cotton and W. Scanlon, "An experimental investigation into the influence of user state and environment on fading characteristics in wireless body area networks at 2.45 GHz," *IEEE Trans. Wireless Commun.*, vol. 8, pp. 6–12, Jan. 2009.

[33] G. Conway, W. Scanlon, S. Cotton, and M. Bentum, "An analytical path-loss model for on-body radio propagation," in *Proc. URSI Int. Symp. on Electromagnetic Theory*, pp. 332–335, Aug. 2010.

[34] A. Fort, C. Desset, J. Ryckaert, P. De Doncker, L. Van Biesen, and P. Wambacq, "Characterization of the ultra wideband body area propagation channel," in *Proc. IEEE Int. Conf. Ultra-Wideband*, p. 6 pp., Sept. 2005.

[35] A. Fort, J. Ryckaert, C. Desset, P. De Doncker, P. Wambacq, and L. Van Biesen, "Ultra-wideband channel model for communication around the human body," *IEEE J. Sel. Areas Commun.*, vol. 24, pp. 927–933, Apr. 2006.

[36] A. Fort, C. Desset, P. De Doncker, P. Wambacq, and L. Van Biesen, "An ultra-wideband body area propagation channel model-from statistics to implementation," *IEEE Trans. Microw. Theory Techniq.*, vol. 54, pp. 1820–1826, Jun. 2006.

[37] T. Zasowski, F. Althaus, M. Stäger, A. Wittneben, and G. Tröster, “UWB for noninvasive wireless body area networks: channel measurements and results,” in *Proc. IEEE Conf. Ultra Wideband Syst. Technol.*, pp. 285–289, Nov. 2003.

[38] P. Hall and Y. Hao, *Antennas and Propagation for Body-Centric Wireless Communications.* Norwood, MA, USA: Artech House, 2006.

[39] P. Hall, “Antennas challenges for body centric communications,” in *Proc. Int. Workshop on Antenna Technol.*, pp. 41–44, march 2007.

[40] A. Sibille, “Statistical antenna modelling,” in *Proc. URSI - 29th General Assembly, Chicago, IL, USA*, pp. 1–6, Aug. 2008.

[41] C. Oliveira, M. Mackowiak, and L. M. Correia, *Statistical Characterization of Antennas in BANs in LTE Advanced and Beyond Wireless Networks: Channel Modelling and Propagation.* Chichester, UK: John Wiley & Sons, Ltd, 2013.

[42] A. Amadjikpe, A. Vera, D. Choudhury, and J. Papapolymerou, “Study of a 60 GHz rectangular patch antenna on a flexible lcp substrate for mobile applications,” in *Proc. IEEE Antennas Propag. Society Int. Symp.*, pp. 1–4, Jul. 2008.

[43] A. Khaleghi and I. Balasingham, “Non-line-of-sight on-body ultra wideband (1 – 6 GHz) channel characterisation using different antenna polarisations,” *IET Microw., Antennas Propag.*, vol. 3, pp. 1019–1027, Oct. 2009.

[44] R. Nabar, H. Bolcskei, V. Erceg, D. Gesbert, and A. Paulraj, “Performance of multiantenna signaling techniques in the presence of polarization diversity,” *IEEE Trans. Sig. Proc.*, vol. 50, pp. 2553–2562, Oct. 2002.

[45] Y. Deng, A. Burr, and G. White, “Performance of MIMO systems with combined polarization multiplexing and transmit diversity,” in *Proc. IEEE Veh. Technol. Conf.*, vol. 2, pp. 869–873, May 2005.

[46] T. Pratt, B. Walkenhorst, and S. Nguyen, “Adaptive polarization transmission of OFDM signals in channels with polarization mode dispersion and polarization-dependent loss,” *IEEE Trans. Wireless Commun.*, vol. 8, pp. 3354–3359, Jul. 2009.

[47] X. Cai and G. Giannakis, “Error probability minimizing pilots for OFDM with M-PSK modulation over rayleigh-fading channels,” *IEEE Trans. Veh. Technol.*, vol. 53, pp. 146–155, Jan. 2004.

[48] O. Edfors, M. Sandell, J.-J. van de Beek, S. Wilson, and P. Borjesson, “OFDM channel estimation by singular value decomposition,” *IEEE Trans. Commun.*, vol. 46, pp. 931–939, Jul. 1998.

[49] Y. Li, J. Cimini, L.J., and N. Sollenberger, “Robust channel estimation for OFDM systems with rapid dispersive fading channels,” *IEEE Trans. Commun.*, vol. 46, pp. 902–915, Jul. 1998.

[50] J. Parsons and A. Turkmani, “Characterisation of mobile radio signals: model description,” *Proc. Inst. Elect. Eng.–I: Commun., Speech Vis.*, vol. 138, pp. 549–556, Dec. 1991.

[51] D. K. Cheng, *Field and Wave Electromagnetics.* Reading, MA: Addison-Wesley, 2 ed., 1989.

[52] A. Abdi, J. Barger, and M. Kaveh, “A parametric model for the distribution of the angle of arrival and the associated correlation function and power spectrum at the mobile station,” *IEEE Trans. Veh. Technol.*, vol. 51, pp. 425–434, May 2002.

[53] A. Kuchar, J. P. Rossi, and E. Bonek, “Directional macro-cell channel characterization from urban measurements,” *IEEE Trans. Antennas Propag.*, vol. 48, pp. 137–146, Feb. 2000.

[54] J. B. Keller, “Geometrical theory of diffraction,” *J. of the Optical Society of America*, vol. 52, pp. 116–130, Feb. 1962.

[55] G. Durgin, “The practical behavior of various edge-diffraction formulas,” *IEEE Antennas and Propag. Mag.*, vol. 51, pp. 24–35, Jun. 2009.

[56] K. Bullington, “Radio propagation at frequencies above 30 megacycles,” *Proceedings of the IRE*, vol. 35, pp. 1122–1136, Oct. 1947.

[57] T. S. Rapparport, *Wireless Communications: Principles & Practice.* Upper Saddle River, NJ: Prentice Hall, PTR., 1 ed., 1996.

# VITA

Seok Chul Kwon graduated from Seoul Science High School for gifted students, Seoul, South Korea in 1996, and received the B.Sc. degree from Yonsei University, Seoul, South Korea in 2001. He was with the R&D Institute of Pantech co., Ltd, Seoul, South Korea in 2001 to 2004, where he worked on CDMA common air interface focusing on layer-3 protocols. He was involved in several projects including six mobile-station products for Motorola and Sprint, which were successfully on the market. He received the M.Sc. degree in Electrical Engineering from the University of Southern California in 2007, and has been a Ph.D. student in the School of Electrical and Computer Engineering, Georgia Institute of Technology from 2007 to 2013. He has been a Graduate Research Assistant with the Wireless Systems Laboratory since 2008, and has performed projects supported by US DARPA and US Army Research Lab. His current research interests are in the broad area of wireless communications including polarized wireless channel modeling; polarization-utilizing techniques such as polarization division multiple access (PDMA) and multiplexing (PDM); and network coding-aware channel assignment.

Geometrical Theory, Modeling and Applications of Channel Polarization

**Seok Chul Kwon**

128 Pages

Directed by Dr. Gordon L. Stüber

Long-term evolution (LTE) standard has been successfully stabilized, and launched in several areas. However, the required channel capacity is expected to increase significantly as the explosively increasing number of smart-phone users implies. Hence, this is already the time for leading researchers to concentrate on a new multiple access scheme in wireless communications to satisfy the channel capacity that those smart users will want in the not-too-distant future. The diversity and multiplexing in a new domain - polarization domain - can be a strong candidate for the solution to that problem in future wireless communication systems.

This research contributes largely to the comprehensive understanding of polarized wireless channels and a new multiple access scheme in the polarization domain - polarization division multiple access (PDMA). The thesis consists of three streams: 1) a novel geometrical theory and models for fixed-to-mobile (F2M) and mobile-to-mobile (M2M) polarized wireless channels; 2) a new wireless body area network (BAN) polarized channel modeling; and 3) a novel PDMA scheme. The proposed geometrical theory and models reveal the origin and mechanism of channel depolarization with excellent agreement with empirical data in terms of cross-polarization discrimination (XPD), which is the principal measure of channel depolarization. Further, a novel PDMA scheme utilizing polarization-filtering detection and collaborative transmitter-receiver-polarization (Tx-Rx-polarization) adjustment, is designed considering cellular orthogonal frequency division multiplexing (OFDM) systems. The novel PDMA scheme has large potential to be utilized with the conventional time, frequency, and code division multiple access (TDMA, FDMA, and CDMA); and spatial multiplexing for next-generation wireless communication systems.